Materials Science & Engineering A

Influence of the Radial-Shear Rolling (RSR) process on the microstructure, electrical conductivity and mechanical properties of a Cu-Ni-Cr-Si alloy

--Manuscript Draft--

Manuscript Number:	MSEA-D-21-01008R2
Article Type:	Research Paper
Keywords:	copper alloys; radial-shear rolling; Plastic deformation; electroconductivity
Corresponding Author:	Yury Gamin, Ph.D. National University of Science and Technology MISIS: Nacional'nyj issledovatel'skij tehnologiceskij universitet MISiS Moscow, RUSSIAN FEDERATION
First Author:	Yury Gamin, PhD
Order of Authors:	Yury Gamin, PhD
	Jairo Alberto Muñoz Bolaños, PhD
	Alexander Aleschenko, PhD
	Alexander Komissarov, PhD
	Nikita Bunits
	Daniil Nikolaev
	Aleksey Fomin, PhD
	Vladimir Cheverikin, PhD
Abstract:	The article describes a method for producing semi-finished products from a copper alloy of the Cu-Ni-Cr-Si system for electrical purposes through the radial-shear rolling (RSR). From the Cu-Ni-Cr-Si alloy by hot deformation, rods with a diameter of 20 mm were obtained, which were then heat treated with quenching and aging. A detailed analysis of the microstructure and properties (mechanical and electrical) of the obtained samples was carried out after RSR and after heat treatment (HT). After RSR, material hardening occurs due to shear deformations forming a gradient structure with grain sizes varying from 8.22 μm to 15.95 μm between the surface and the center of the rod. The microstructure and mechanical property analysis showed that after heat treatment, the alloy is thermally hardened due to the precipitation of Ni2Si and Cr3Si particles uniformly distributed in the sample volume in the form of fine inclusions with an average size of 0.56-0.65 μm. After heat treatment, the alloy enhanced its mechanical properties (ultimate tensile strength (UTS) ~ 700-750 MPa, yield strength (YS) ~ 557-606 MPa, and elongation between 17 and 22%) and its electrical conductivity of 45.17% IACS from the 30.52% IACS of the RSR material. The improved mechanical properties of the heat-treated material are due to the different strength contributions mainly coming from dislocations and precipitates. The electrical conductivity improvement after the heat treatment is related to the dislocation density reduction and the increase in grain boundary misorientation due to the recrystallization phenomenon giving rise to a lower number of boundaries but with a twinning character. Thus, the RSR method offers a new industrial alternative for the production of semi-finished products from a Cu-Ni-Cr-Si alloy in the form of rods with diameters ranging from 10-55 mm.

Dr. Yu.V. Gamin
National University of Science and Technology “MISIS”, Moscow 119049, Russia
E-mail: gamin910@gmail.com
Tel.: +79258895920

Prof. Dr. Ewald A. Werner,
Editor of the Journal Materials Science and Engineering: A

June 26th, 2021

Subject: Revision manuscript: MSEA-D-21-01008R1

Dear Professor,

Please find in attached files of our manuscript entitled **" Influence of the Radial-Shear Rolling (RSR) process on the microstructure, electrical conductivity and mechanical properties of a Cu-Ni-Cr-Si alloy"** to be submitted electronically for publication in the Journal Materials Science and Engineering: A. The manuscript has not been published before and is not currently submitted for publication to any other journal and will not be submitted elsewhere before a decision is made by this journal. This research work has been revised and approved by all the co-authors and institutions.

We appreciate reviewer’s detailed comments. They raised new topics that enriched the content of the paper. Our responses are marked in Italics below and the changes in the manuscript are marked using yellow highlighting.

Yours sincerely

Dr. Yu.V. Gamin

Corresponding author
On behalf of all authors.

Dr. Yu.V. Gamin
National University of Science and Technology "MISIS", Moscow 119049, Russia
E-mail: gamin910@gmail.com
Tel.: +79258895920

Prof. Dr. Ewald A. Werner,
Editor of the Journal Materials Science and Engineering: A

June 26th, 2021

Subject: Revision manuscript: MSEA-D-21-01008R1

Dear Professor,

Please find in attached files of our manuscript entitled **"Influence of the Radial-Shear Rolling (RSR) process on the microstructure, electrical conductivity and mechanical properties of a Cu-Ni-Cr-Si alloy"** to be submitted electronically for publication in the Journal Materials Science and Engineering: A. The manuscript has not been published before and is not currently submitted for publication to any other journal and will not be submitted elsewhere before a decision is made by this journal. This research work has been revised and approved by all the co-authors and institutions.

We appreciate reviewer's detailed comments. They raised new topics that enriched the content of the paper. Our responses are marked in Italics below and the changes in the manuscript are marked using yellow highlighting.

Reviewers' comments:

Reviewer #2:

The revised manuscript complies with the recommendations of the previous reviewer. It should be ready for publication except for minor grammar corrections. I have made the effort of reducing the most I could a tendency to verbosity that should be rechecked, either to see if the original intended meanings were respected or there are still some undetected wordiness that complicates the reading task. The meaning of some words is somehow misleading and have been replaced. Please recheck whenever you remember have used in the same sense to see if you still sustain the wording.

Units used should be clarified. MSm/m seems to be unexplained and undefined.

Answer: *Thank you for the comments.*
We have corrected all errors in the text in accordance with the comments (yellow color highlighted).
The SI unit of conductivity is Siemens per meter (S/m). In the manuscript we used units of measurement in accordance with the international standard, as well as %IACS for comparison with other copper alloys. We have corrected the typing mistake, we wanted to mean MS/m (megasiemens/meter) instead of MSm/m.

4.3 Electroconductivity and hybrid properties

The conductivity measurements are presented in MS/m (megasiemens/meter) and %IACS, that is, as a percentage of pure copper's conductivity (58 MS/m). Fig. 14 shows a diagram of the electrical conductivity values after RSR and aging treatment. At first glance, the heat treatment has a significant effect on electrical conductivity. However, after RSR, the electrical conductivity is 30.52% IACS. Quenching and subsequent aging of the samples lead to an increase in the electrical conductivity value by 48% (Fig. 14).

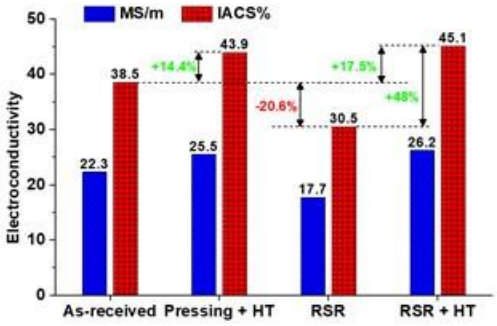

Fig. 14 Electrical conductivity of Cu-Ni-Cr-Si alloy after RSR and heat treatment

The technical standard for Cu-Ni-Cr-Si alloy semi-finished products shows a conductivity value of at least 24 MS/m. Therefore, the two analyzed conditions comply with this requirement. It is also worth noting that these values are obtained based on the conditions used in an industrial environment to obtain semi-finished products by extrusion and drawing.

Reviewer #3:

Manuscript Number: MSEA-D-21-01008_R1

Points in favor:
The article deals with using the Radial-Shear Rolling (RSR) process for producing semi-finished products of a Cu-Ni-Cr-Si alloy aiming properties similar to traditional thermomechanical

methods. The authors analyzed the microstructure and tried to correlate it with electrical conductivity and mechanical properties. We believe that this kind of analysis is always welcome, trying to search for new ways to improve the mechanical properties and electrical conductivity of finished products of copper alloys.
Answer: *We appreciate the positive feedback from the reviewer.*

Points detracting:
I have read the paper with interest. However, I am afraid I cannot recommend its publication. This paper has some interesting results, but there are sufficient challenges that make it unsuitable for publication in its present form. These challenges are significant, and it is unclear whether or not the authors can correct them to resubmit the manuscript after revising it. The issues of considerable concern are indicated in the following.
(Please, use the unmarked version to correlated the pages)

1 - English deserves revision. In the attached file, I am sending some English mistakes. I have even found Spanish words. However, I do think that it is mandatory to send the article to an English speaker after all suggested modifications. The authors did not pay attention or did not read the final version before submitting the paper. I have also found source error messages (Error! Reference source not found).

Answer: *Thank you for the comments. We have corrected all the grammar and links issues.*

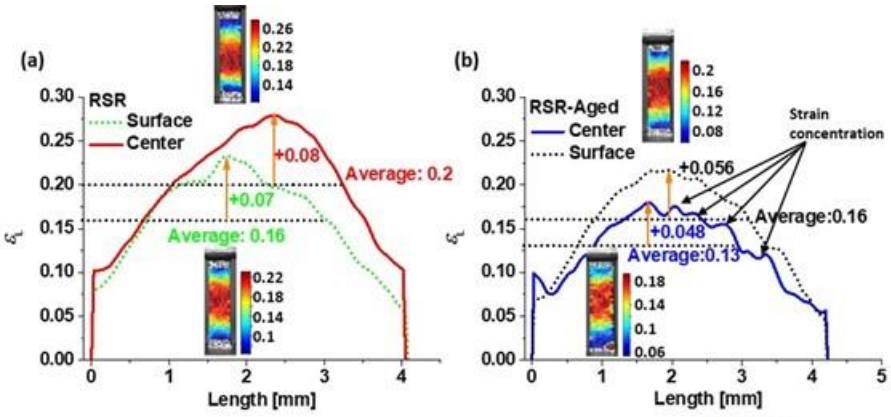

Fig. 10 Strain evolution at the plastic instability points indicated in Fig. 8b, (a) RSR, and (b) RSR+aging.

2 - Introduction.
2a) The Introduction is good. However, after reading the first paragraph of page 3, I would say that the sentence "One of the methodologies that" is useless in the way it is. RSR is not a severe plastic deformation technique. It deforms severely. However, it does not severely deform. It is not SPD.

Answer: *The sentence has been corrected following the recommendations.*

Today, heterogeneous structures have aroused great interest due to their excellent combination of strength and ductility [17,18]. Several methodologies have been proposed to obtain heterogeneous microstructures with different microstructural configurations (for example, heterogeneous distribution of grain sizes, localized distribution of phases in the piece's geometry, heterogeneous dislocation densities, among other characteristics) [17,19–23]. One methodology that has been used is controlled severe plastic deformation applied to sheets, bars, and discs using ECAP and high pressure torsion (HPT), respectively [24–26]. Thus, the initial deformation stages of SPD produce deformation gradients across the sample dimensions. For example, high surface shear strains are obtained after ECAP processing while maintaining its central section less deformed. Although RSR cannot be considered an SPD technique due to the change in the sample's dimensions, it does produce a similar effect between the surface and the center of the deformed material giving rise to a heterogeneous structure [27].

2b) Why use such a large amount of citations from only one team and material? I believe that it would be possible to find articles using SRS and from different teams and materials. Please, try to find them and remove part of the cited articles.

Answer: *Thank you for the comment. We have used some new references from other research teams.*

However, at the moment, the leading industrial methods for producing semi-finished products from copper alloys for electrical purposes are extrusion and drawing [1]. From the manufacturability point of view, the extrusion method has significant disadvantages. These include the inability to quickly reconfigure to a different size and the need for a large number of extrusion tools. To obtain semi-finished products from copper alloys with a high level of operational properties, the application of the radial-shear rolling (RSR) method may be relevant. This method of metal forming has found a full application for producing long round bars of various steel grades [13], titanium alloys [14], and aluminum alloys [15]. Due to the action of shear strains, a spiral-shaped gradient structure is formed with an ultrafine-grained surface layer, which provides an increase in strength properties while maintaining satisfactory ductility [16].

central section less deformed. Although RSR cannot be considered an SPD technique due to the change in the sample's dimensions, it does produce a similar effect between the surface and the center of the deformed material giving rise to a heterogeneous structure [27].

The developed designs of RSR mills allow obtaining long rods (up to 9 m) with different diameters on one set of working tools-rolls [28]. The weight and dimensions of such equipment are significantly lower compared to press equipment. When it is necessary to organize the production of small batches, but a large number of different sized rods, it may be relevant to replace the press equipment with RSR mills. There is no need for a large number of working

2c) The sentence after the one mentioned above is not entirely correct. ECAP will produce inhomogeneities only if using small numbers of passes. Please, rewrite the sentence to be more precise.

Answer: *Thank you for the comment. The sentence has been corrected following the recommendations.*

Today, heterogeneous structures have aroused great interest due to their excellent combination of strength and ductility [17,18]. Several methodologies have been proposed to obtain heterogeneous microstructures with different microstructural configurations (for example, heterogeneous distribution of grain sizes, localized distribution of phases in the piece's geometry, heterogeneous dislocation densities, among other characteristics) [17,19–23]. One methodology that has been used is controlled severe plastic deformation applied to sheets, bars, and discs using ECAP and high pressure torsion (HPT), respectively [24–26]. Thus, the initial deformation stages of SPD produce deformation gradients across the sample dimensions. For example, high surface shear strains are obtained after ECAP processing while maintaining its central section less deformed. Although RSR cannot be considered an SPD technique due to the change in the sample's dimensions, it does produce a similar effect between the surface and the center of the deformed material giving rise to a heterogeneous structure [27].

3 – Experimental

3a) How was the ingot produced?

Answer: *The original ingot was obtained by chill casting. Information added in the manuscript.*

2 Experimental materials and methods

The initial billet (cylindrical ingot with a diameter of 110 mm) was obtained by chill casting and then deformed by hot pressing until the 60 mm rod diameter. Further, a hot-pressed rod was used for rolling. The initial billet diameter was 60 mm, and the length was 250 mm.

3b) It appears that Table 1 brings information related to theoretical composition or some standard, as it is not normal to have a range of composition after the determination. After determination, an error is inserted to show the quality of the analysis.
Therefore, please, introduce the real chemical composition, compared or not with some standard, and give information about the equipment used to do it.

Answer: *Thank you for the comment. We have introduced the real chemical composition of the alloy, and we have also added the method and equipment used.*

Table 1 presents the alloy's chemical composition obtained from the EDS spectrum of several SEM images employing TESCAN VEGA SBH3 scanning electron microscope (SEM-EDS) from Oxford Instruments.

3

Table 1. Chemical composition of Cu alloy (% wt.)

Alloy	Cu	Ni	Cr	Si	Al	Zn	Fe	Other
Cu-Ni-Cr-Si	95.02	2.89	1.03	0.92	0.03	0.08	0.03	≤ 0.1

3c) Where are the data of Table 2 from? Please, give information by citing something or how data were obtained.

Answer: *Those data correspond with experimental values measured in this study.*

Table 2 summarizes the alloy's experimental electrical conductivity and mechanical properties.

Table 2. Experimental properties of Cu-Ni-Cr-Si alloy in the initial state

Parameter name	Value
Hardness (HV)	130-150
Ultimate tensile strength (MPa)	340-380
Yield strength (MPa)	220-240
Elongation (%)	20
Electrical conductivity (MS/m)	22.3

3d) Figure 1 is useless. It is industrial equipment, and the theory is already in books. Furthermore, the same equipment was used in a previous publication, and Figure 1 is almost the same used in such a publication (https://doi.org/10.1051/matecconf/202031511001). Therefore, remove Figure 1 and cite the article to define angles related to RSR.

Answer: *Thank you for the comment. Fig. 1 has been removed and appropriately cited.*

The initial billets were deformed in the hot state by radial-shear rolling. RSR was carried out at the semi-industrial rolling mill located in the laboratory of the Department of Metal forming (NUST "MISIS", Moscow). The mills are equipped with three work rolls that are deployed at a feed angle β and a toe angle δ, as indicated in previous studies [29]. Work rolls located symmetrically concerning the central rolling axis form a deformation zone rotating in one direction and deforming the workpiece. The sample moves along the deformation zone following a helicoidal path.

3e) Table 3 must be placed after Equation (2).

Answer: *Thank you for the comment. We have moved Table 3 after equation 2.*

$$\sum_{i=1}^{n} \mu_i = \frac{F_0}{F_n} = \mu_1 \cdot \mu_2 \cdot \mu_3 \cdot \ldots \cdot \mu_n \qquad (2)$$

Table 3. Deformation conditions of Rolling.

Pass Number, i	Diameter of workpiece D_{i-1}, mm	Diameter of the resulting rod D_i, mm	Elongation ratio μ_i	$\Sigma\mu_i$
1	60	46	1.70	1.70
2	46	36	1.63	2.78
3	36	28	1.65	4.60
4	28	20	1.96	9.00

4) Results

4.1) In the last sentence of the first paragraph of page 7, please, change "These mechanical properties" to read "This yield strength".

Answer: *Thank you for the comment. The phrase has been corrected.*

3 Results and analysis

3.1 As-received material

The initial material was obtained by casting, obtaining bars of 110 mm in diameter. Thus, Fig. 4a indicates the microstructure obtained by optical microscopy (OM) after casting. This figure shows the formation of a structure of coarse grains of different sizes. Due to the solidification process in which the surfaces are cooled before the central zone, a variation in grain size occurs, as indicated in Fig. 4b. This figure indicates the existence of two families of grain size, one formed by sizes smaller than 3 mm located around the surface with an average value of 0.92 mm and the other comprising sizes between 4 mm and 8 mm located preferably in the center of the bar with an average value of 4.83 mm. Concerning alloy tensile behavior, Fig. 4c indicates that the as-cast material reaches a yield strength of 220 MPa with a fracture strain of 20%. Additionally, the EBSD characterization in Fig. 4d confirms a microstructure with large grains. Those grains are free of dislocations and substructures in its interior, as confirmed by the misorientation profile lines 1-2 and 3-4 in Fig. 4e. The misorientation profiles show constant behaviors inside the grains, and only appreciable changes in misorientation occur when crossing the grain boundaries. This yield strength reflect the effect of the alloying elements in the material, i.e., an increase in yield strength of 60% concerning high-purity electrolytic copper (87 MPa, yield strength) [31].

4.2) Figure 4: Please remove the background colors from the graphics in Figures b, c, and e. Also, use symbols along with lines. Remember that the article will be printed in grayscale.

Answer: *Thank you for the comment. Fig.4 (now Fig. 3) has been edited following your recommendations.*

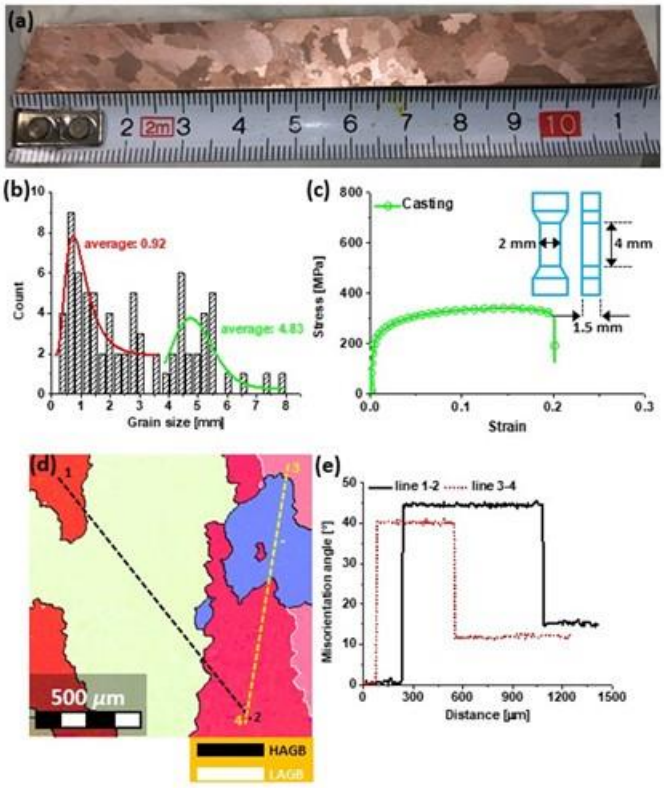

Fig. 3 Initial microstructure after casting process (a), grain size in the casting condition (b), tensile properties (c), EBSD map (d), and misorientation profiles for the lines indicated in the EBSD map (e).

4.3) Figure 5. Please check the data in Figure f. The average grain size of the surface does not match that seen in Figure d. Figure d is taking part of the grains from the center. Therefore, the related information regarding grain size in Figure f is incorrect. The average grain size is much larger than the one presenting it.

Answer: *Thank you for the comment. The EBSD colored maps represent the grain area and figs. 5c and 5f represent the average grain size (i.e., diameter). On the other hand, the grain size representation of Fig. 5f corresponds well with fig. 5d. The grain size according to the scale is not larger than 200 µm. So, we have checked the results obtaining the same curves. To avoid confusion, we have changed the map's color code using grain diameter values.*

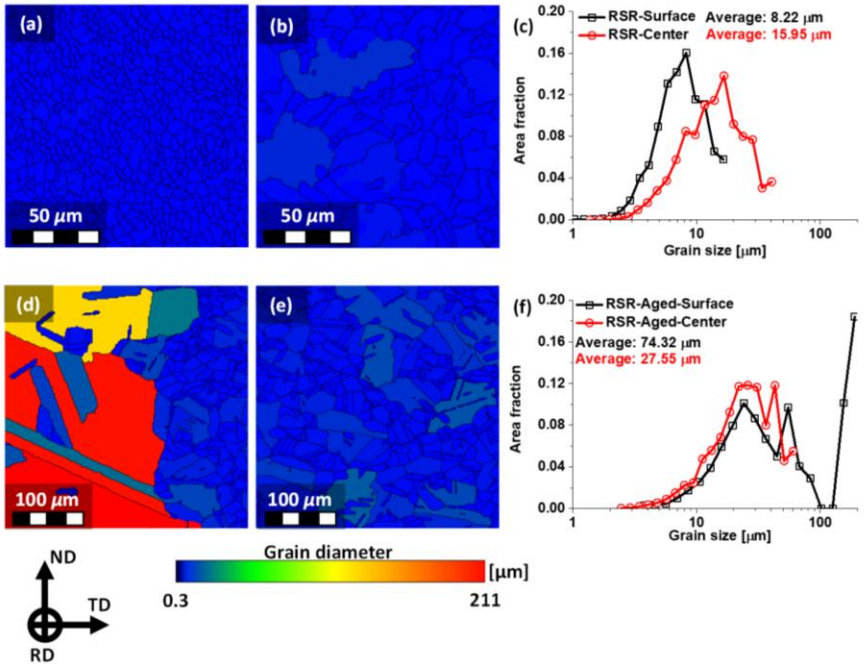

Fig. 4 Surface grain diameter map after RSR (a), center grain diameter map after RSR (b), grain size evolution after RSR (c), surface grain diameter map after RSR+aging (d), center grain diameter map after RSR+aging (e), grain size evolution after RSR+aging (f).

4.4) Figure 5. Why does grain instability only occur on the deformed surface? In other words, please, explain the abnormal grain growth on the sample surface.

Answer: *Thank you for the comment. The abnormal grain growth is a consequence of the deformation gradient across the rod diameter after RSR processing. Thus, the strain heterogeneity between the rod surface and its center zone gives rise to recrystallization gradients after the heat treatment. Further explanation is given in the discussion section.*

Fig. 4 Surface grain area map after RSR (a), center grain area map after RSR (b), grain size evolution after RSR (c), surface grain area map after RSR+aging (d), center grain area map after RSR+aging (e), grain size evolution after RSR+aging (f).

In the hardening process by heat treatment, Fig. 5d-Fig. 5f manifest an evident grain structure change. After the heat treatment, grain recrystallization occurs in a heterogeneous way, as the grain size increases, especially in the surface layer, which may be due to different deformation degree induced by the RSR process across the rod diameter. After the aging treatment, the microstructure evolution in Fig. 5d and Fig. 5e shows the opposite behavior concerning the RSR material. The average grain size in the central part of the rod after heat treatment is 27.5 μm. At the surface of the rod, coarse grains larger than 100 μm in size are observed, while the average grain size, according to measurements, is 74.32 μm. Besides, in the microstructure of samples after heat treatment, one can observe characteristic annealing twins formed during grain growth. Therefore, the abnormal grain growth is a consequence of the deformation gradient across the rod diameter after RSR processing. Thus, the strain heterogeneity between the rod surface and its center zone gives rise to recrystallization gradients after the heat treatment.

4.5) Figure 5. Please remove the background colors from the graphics in Figures b, c, and e. Also, use symbols along with lines. Remember that the article will be printed in grayscale.

Answer: *Thank you for the comment. Fig. 5 (now Fig. 4) has been edited.*

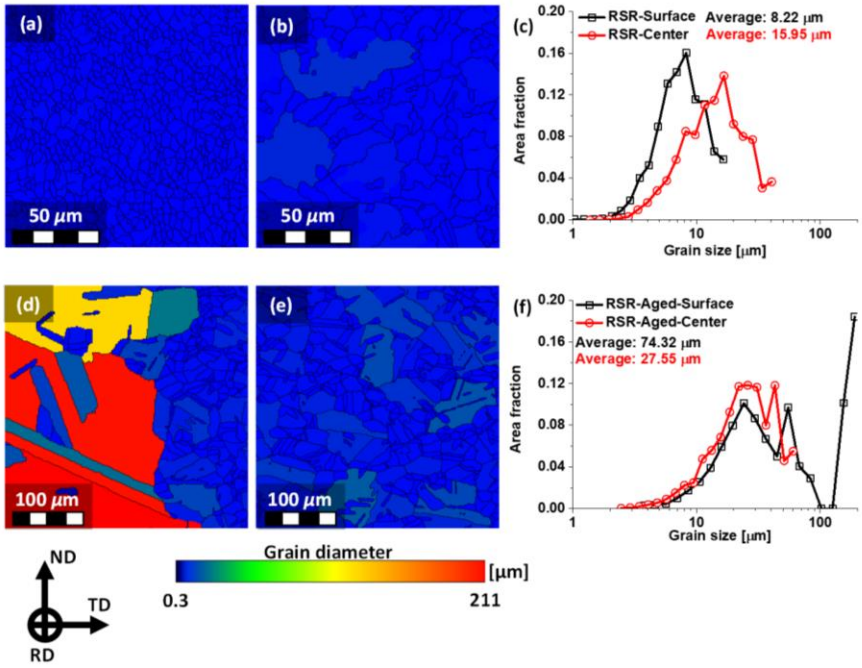

Fig. 4 Surface grain diameter map after RSR (a), center grain diameter map after RSR (b), grain size evolution after RSR (c), surface grain diameter map after RSR+aging (d), center grain diameter map after RSR+aging (e), grain size evolution after RSR+aging (f).

4.6) First paragraph of page 10. The sentence: "On the contrary, Cr and Si elements are preferentially located..." Strangely, the precipitation of some particles occurred in regions of low energy, as reported by the authors, inside the grain.
If the authors look more deeply at the image in Fig. 6b, they will notice that the sample is not fully recrystallized or has smaller grains than those presented by the large contours. In any case, most of these particles are actually in contours or sub-contours and not free inside the grain. Please, pay attention to the boundaries that I have mentioned, modify the sentence and comment and discuss this behavior correctly in the article.

Answer: *Thank you for the comment. We have rewritten the phrase.*

To better describe microstructural characteristics, energy dispersive spectroscopy (EDS) analyses were performed. Fig. 6a indicates the material's microstructure after RSR processing plus aging treatment, indicating the different regions analyzed (red squares). The SEM image allows observing the grain boundaries and the presence of particles of different sizes. In Fig. 6b, the main alloying elements' EDS map is indicated for the spectrum area 1. At first glance, it can be assessed that Ni and Cu concentrations are homogeneously distributed throughout the material. On the contrary, Cr and Si elements seem to be located in small regions forming particle colonies close to the grain boundaries. Fig. 6c shows the EDS spectra for the

4.7) First paragraph of page 10. The sentence: "...shows alloying elements such as Ni, Cr, and Si mainly." Why mainly? Are there other measurable alloying elements by EDS?

Answer: *Thank you for the comment. We have rewritten the sentence.*

To better describe microstructural characteristics, energy dispersive spectroscopy (EDS) analyses were performed. Fig. 6a indicates the material's microstructure after RSR processing plus aging treatment, indicating the different regions analyzed (red squares). The SEM image allows observing the grain boundaries and the presence of particles of different sizes. In Fig. 6b, the main alloying elements' EDS map is indicated for the spectrum area 1. At first glance, it can be assessed that Ni and Cu concentrations are homogeneously distributed throughout the material. On the contrary, Cr and Si elements are preferentially located on small regions forming particle colonies within the grains and close to the grain boundaries. Fig. 6c shows the EDS spectra for the different areas indicated in Fig. 6a. Spectrum number 1, corresponding to the entire analyzed area shows alloying elements such as Ni, Cr, and Si.

4.8) First paragraph of page 10. The sentence: "... confirm the formation of precipitates rich in Cr, Si, and Ni with a Ni matrix enriched." Why Ni-rich precipitates? Ni is everywhere. It is part of the matrix. Using SEM is impossible to affirm that you have Ni-rich precipitates.

Answer: *Thank you for the comment. We agree with your comment. We wanted to mean precipitates rich in Cr and Si.*

On the other hand, spectra 4 and 5 within the grains indicate low concentrations of Cr and Si and a domain of Cu and Ni. In this way, the previous observations confirm the formation of precipitates rich in Cr, and Si with a Ni matrix enriched. Looking in more detail at the EDS maps for Cu, Si, Ni, and Cr in Fig. 6d, we see that many of the high Si concentration spots also show high Cr content. According to Rdzawski et al. [33], these particles with a high content of Cr and Si correspond to Cr_3Si precipitates, which are preferentially located around the grain boundaries.

4.9) First paragraph of page 10, last sentence. The last sentence confirms my comment 4.6.

Answer: *Thank you for the comment. We have followed your recommendations.*

4.10) Page 10, last sentence of the first paragraph and first sentence of the second paragraph. As the particles are very big (in fact, they are not precipitates anymore, they are particles), please, perform x-ray diffraction to access information regarding such second phases.

Answer: *Thank you for the comment. We have added X-ray diffraction analysis data to the manuscript to confirm the presence of second phases Ni_2Si and Cr_3Si.*

The analysis of the phase composition was carried out using the X-Ray diffraction method using a Multifunctional X-ray diffractometer DRON-8. The following parameters were used for scanning: voltage 40 kV, Amperage 20 mA, scanning step 0.05°, exposure time 4 s - discrete mode, PDF-2 Release 2014 ICDD database.

Tensile tests in different zones across the sample diameter (surface and center) were evaluated using a universal testing machine at room temperature. Sample gauge dimensions of 4 mm x 1.5 mm x 2 mm tested at a constant strain rate of $1 \cdot 10^{-3}$ s^{-1}. Strain maps were obtained

X-ray diffraction confirms the formation of different types of precipitates such as Cr_3Si and Ni_2Si. Fig. 7 shows the diffraction patterns for samples after RSR and aging heat treatment. It can be seen that the chromium silicide and nickel silicide phase concentrations are about 0.84% and 0.9%, respectively. Samoilova et al. [38] showed that for the Cu-3%Ni-1.5%Si-1%Cr alloy, the main phases observed after heat treatment are Cr_3Si and Ni_2Si. The formation of these precipitates suggests the activation of an additional hardening mechanism in the material processed by RSR and subsequently heat treated.

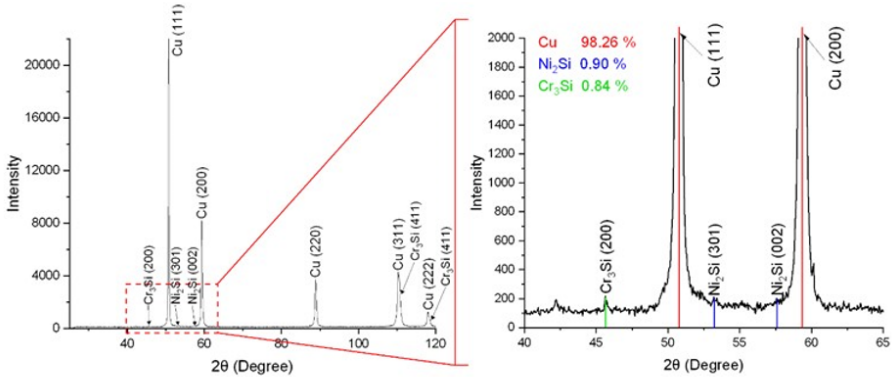

Fig. 7 Diffraction pattern for the Cu-Ni-Cr-Si alloy after RSR + Aging treatment

4.11) Page 10, second paragraph. Please, insert a reference for ImageJ.

Answer: *Thank you for the comment. The ImageJ reference has been added.*

Aging treatment also favors the precipitation of Ni_2Si phases in the matrix as particles uniformly distributed in the bulk of the samples in the form of small inclusions. Cheng et al. [34] also reported the formation of this type of precipitates after aging at a temperature of 500 °C for a Cu-Ni-Si-Cr alloy. Analyzing the EDS images for each element using ImageJ [35], an appreciation of the precipitate particles' size can be made, as indicated in Fig. 7. The histograms show an average particle size between 0.56 μm and 0.65 μm that follows a lognormal function. The inset in Fig. 7 highlights a microstructure where some small particles appear either inside the grains (blue ellipse) or forming colonies (green ellipse). However, several authors have reported nano-precipitates' formation with average values of 8 nm [34,36]. Therefore, the analyses from the SEM images represent a more descriptive than quantitative result of the precipitates' real size.

4.12) Page 10, second paragraph, antepenultimate sentence (The inset in Fig. 7...). Please, see my above comment regarding boundaries. Unfortunately, the resolution of the insert is not enough for me to see more details as above. Anyway, please, verify and modify as suggested above.

Answer: *Thank you for the comment. We have modified the sentence as you suggested.*

To better describe microstructural characteristics, energy dispersive spectroscopy (EDS) analyses were performed. Fig. 6a indicates the material's microstructure after RSR processing plus aging treatment, indicating the different regions analyzed (red squares). The SEM image allows observing the grain boundaries and the presence of particles of different sizes. In Fig. 6b, the main alloying elements' EDS map is indicated for the spectrum area 1. At first glance, it can be assessed that Ni and Cu concentrations are homogeneously distributed throughout the material. On the contrary, Cr and Si elements seem to be located in small regions forming particle colonies close to the grain boundaries. Fig. 6c shows the EDS spectra for the

show high Cr content. According to Rdzawski et al. [34], these particles with a high content of Cr and Si correspond to Cr_3Si precipitates, which are preferentially located around the grain boundaries.

Aging treatment also favors the precipitation of Ni_2Si phases in the matrix as particles uniformly distributed in the bulk of the samples in the form of small inclusions. Cheng et al. [35] also reported the formation of this type of precipitates after aging at a temperature of 500 °C for a Cu-Ni-Si-Cr alloy. Analyzing the EDS images for each element using ImageJ [36], an appreciation of the precipitate particles' size can be made, as indicated in Fig. 6. The histograms show an average particle size between 0.56 μm and 0.65 μm that follows a lognormal function. The inset in Fig. 6 highlights a microstructure where some small particles appear either inside the grains (blue ellipse) or forming colonies close to the grain boundaries (green ellipse). However, several authors have reported via TEM that after plastic deformation, the Cu-Cr-Ni-Si alloy can form nano-precipitates with average sizes of 8 nm [35,37]. Therefore, the analyses from the SEM images represent a more descriptive than quantitative result of the precipitates' real size.

4.13) Page 10, second paragraph, penultimate sentence (However, several authors have...). It would be necessary to have TEM data to ensure that you do not have such precipitate size. If the intention was to say that you have, please, give TEM information.

Answer: *Thank you for the comment. We wanted to mean that this type of alloys after plastic deformation can form nano-precipitates.*

Aging treatment also favors the precipitation of Ni_2Si phases in the matrix as particles uniformly distributed in the bulk of the samples in the form of small inclusions. Cheng et al. [35] also reported the formation of this type of precipitates after aging at a temperature of 500 °C for a Cu-Ni-Si-Cr alloy. Analyzing the EDS images for each element using ImageJ [36], an appreciation of the precipitate particles' size can be made, as indicated in Fig. 6. The histograms show an average particle size between 0.56 μm and 0.65 μm that follows a lognormal function. The inset in Fig. 6 highlights a microstructure where some small particles appear either inside the grains (blue ellipse) or forming colonies close to the grain boundaries (green ellipse). However, several authors have reported via TEM that after plastic deformation, the Cu-Cr-Ni-Si alloy can form nano-precipitates with average sizes of 8 nm [35,37]. Therefore, the analyses from the SEM images represent a more descriptive than quantitative result of the precipitates' real size.

4.14) Page 10, second paragraph, last sentence (Therefore, the analyses from...). I did not understand the statement. Even if you do not have the complete information, you have the one for this magnification, and it is quantitative. The authors should modify the two last sentences (comments 4.13 and 4.14) to be more precise.

Answer: *Thank you for the comment. We have modified the sentences.*

show high Cr content. According to Rdzawski et al. [34], these particles with a high content of Cr and Si correspond to Cr_3Si precipitates, which are preferentially located around the grain boundaries.

Aging treatment also favors the precipitation of Ni_2Si phases in the matrix as particles uniformly distributed in the bulk of the samples in the form of small inclusions. Cheng et al. [35] also reported the formation of this type of precipitates after aging at a temperature of 500 °C for a Cu-Ni-Si-Cr alloy. Analyzing the EDS images for each element using ImageJ [36], an appreciation of the precipitate particles' size can be made, as indicated in Fig. 6. The histograms show an average particle size between 0.56 μm and 0.65 μm that follows a lognormal function. The inset in Fig. 6 highlights a microstructure where some small particles appear either inside the grains (blue ellipse) or forming colonies close to the grain boundaries (green ellipse). However, several authors have reported via TEM that after plastic deformation, the Cu-Cr-Ni-Si alloy can form nano-precipitates with average sizes of 8 nm [35,37]. Therefore, the analyses from the SEM images represent a more descriptive than quantitative result of the precipitates' real size.

4.15) Page 11. Figure 6. I know that the background colors of the EDS spectra are standard on the equipment, but please reprocess the data and remove the background colors from such spectra.

Answer: *Thank you for the comment. We have removed the EDS spectra backgrounds.*

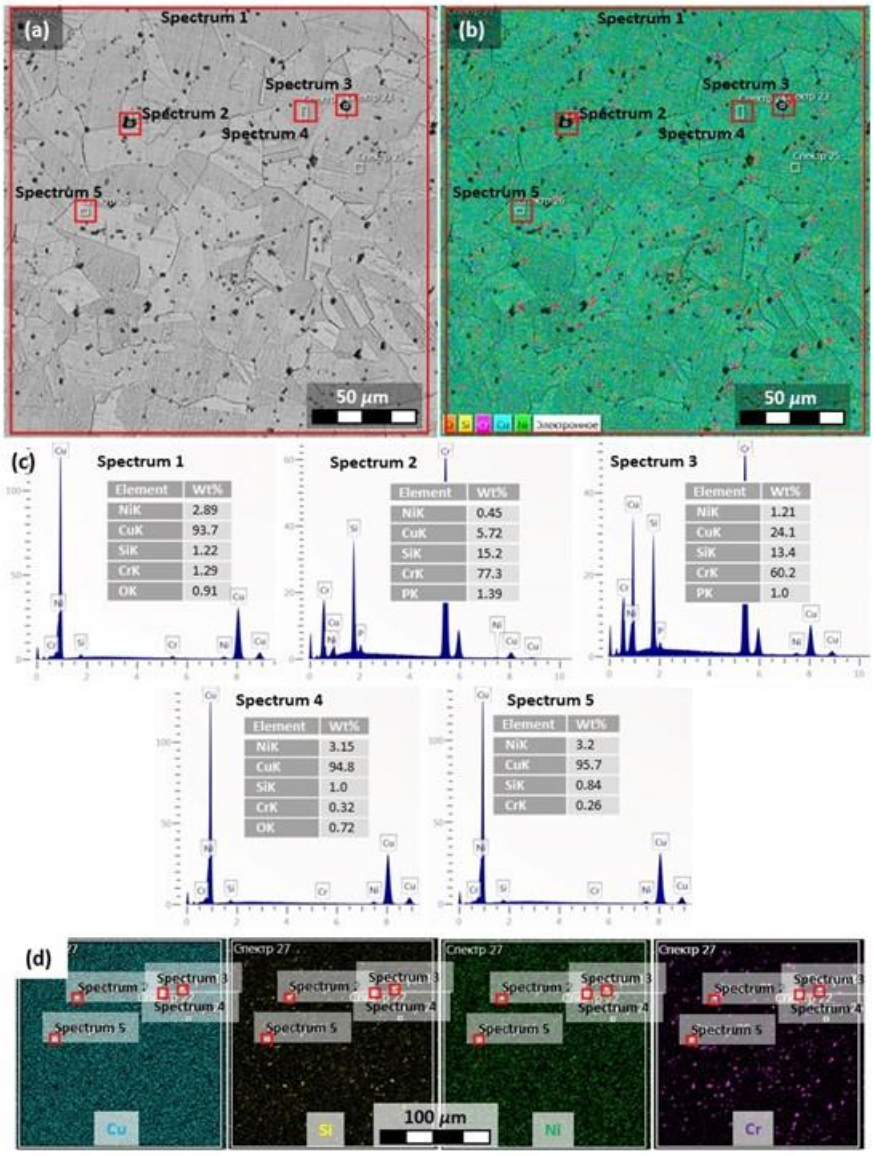

Fig. 5 SEM map after aging treatment (a), EDS map (b), EDS spectrums for the red squares indicated in figure (a) (c), and Cu, Si, Ni, and Cr EDS maps (d)

4.16) Page 12. Line graphs of Figure 7. Please, use symbols along with lines. Remember that the article will be printed in grayscale.

Answer: *Thank you for the comment. We have modified the lines to make them readable in grayscale.*

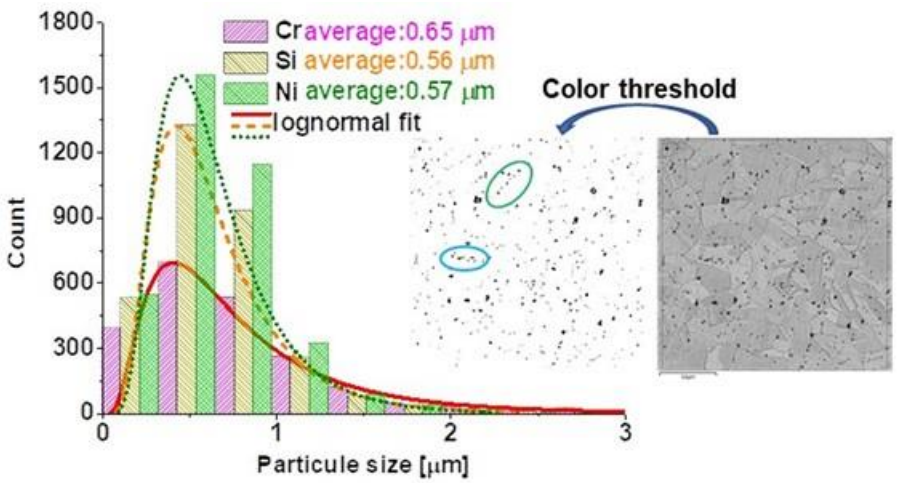

Fig. 7 Precipitation particles sizes.

4.17) Page 12, first paragraph, Two last sentences (The same behavior...). The statements are bizarre. The grain size on the surface is much larger than in the center. It should produce a big difference in hardness. Why did this not happen?

Answer: *Thank you for the comment. We have re-calculated the hardness values, and we observed some changes between the center and the surface.*

3.3 Mechanical properties

Fig. 8 shows the hardness distribution in the cross section for both conditions RSR and heat-treated RSR. The RSR material shows some hardness variation from the surface to the rod center. The opposite behavior is observed in the heat-treated RSR material, where hardness values are high close to the center and decrease near the surface. Additionally, a hardness value of ~260-280 HV above the ~180-200 HV of the RSR condition was obtained after the aging treatment representing a hardness increment of 40-45%.

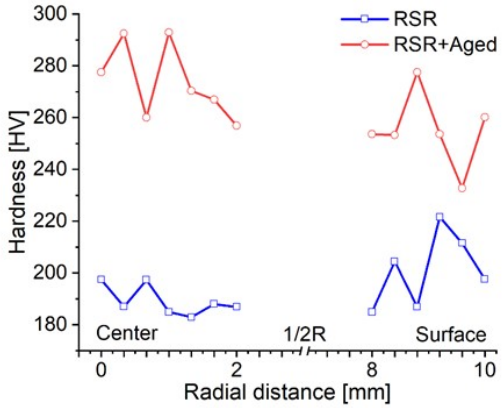

Fig. 8 Hardness evolution in the cross section after RSR and RSR + aging treatment.

4.18) Page 12. Figure 8. Please use symbols along with lines in the graphics. Remember that the article will be printed in grayscale.
Where is the center, zero or 10 mm? Please, give this information on the graph.

Answer: *Thank you for the comment. We have edited the figure following your recommendations.*

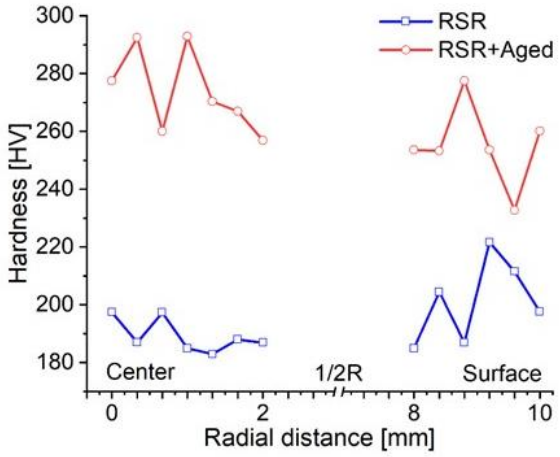

Fig. 8 Hardness evolution in the cross section after RSR and RSR + aging treatment.

4.19) Page 13. First paragraph, second sentence (Thus, the obtained...). Please, specify that the statement is for aged samples.

Answer: *Thank you for the comment. We have specified that the statement is for aged samples.*

According to the standard specifications for this alloy, the Vickers hardness of hot-pressed rods should not be lower than 200 HB (210 HV) [38]. Thus, the obtained hardness values for aged samples are higher than the standard values.

4.20) Page 13. First paragraph, last sentence. Here you cannot conclude. You can infer, or something like this. However, I think it is better to correct and move the sentence to a more appropriate position during the discussion.

Answer: *Thank you for the comment. The sentence has been moved forward into the discussion section.*

In this way, Fig. 11 collects the different strength contributions of the materials obtained through equations (4)-(7). Fig. 11a indicates how the main strength contribution comes from dislocations. It is also shown that in the surface zone, the second contribution associated with the grain size is due to the bigger grain refinement in this area, as shown in Fig. 5a. After the aging treatment, Fig. 11b shows that the main strength contributions come from the precipitates and dislocations components in both the surface and center areas. This behavior demonstrates the greater strength of the heat-treated material concerning the RSR as a consequence of the additional contribution of the precipitates. Fig. 11b shows that the aging treatment generated larger amounts of precipitates near the surface due to a possible recrystallization gradient as a consequence of the microstructure heterogeneity after the RSR process. Thus, hardness and the yield strengths values lead to infer that the RSR method is a good and versatile alternative for the production of rods with diameters in the range of 10-55 mm.

Using the model proposed by Kocks et al. [42], which describes the rate of change in the density of dislocations with deformation ($\frac{\partial \rho}{\partial \varepsilon}$) as a function of the density of dislocations (ρ), it is possible to know more about dislocations in materials through the following equation:

4.21) Page 13, Figure 9. Why is the strength greater on the surface after the heat treatment? Please, explain and discuss.
Also, Please use symbols along with lines in the graphics. Remember that the article will be printed in grayscale.

Answer: *Thank you for the comment. It is true that on the aged material surface, we can observe abnormal grain growth, which is why a lower strength would be expected than in the center. However, the tensile sample thickness is 1.5 mm, which means that the surface sample covers both large grains and areas of grains such as those found in the center of the sheet. Symbols have used in Fig 9.*

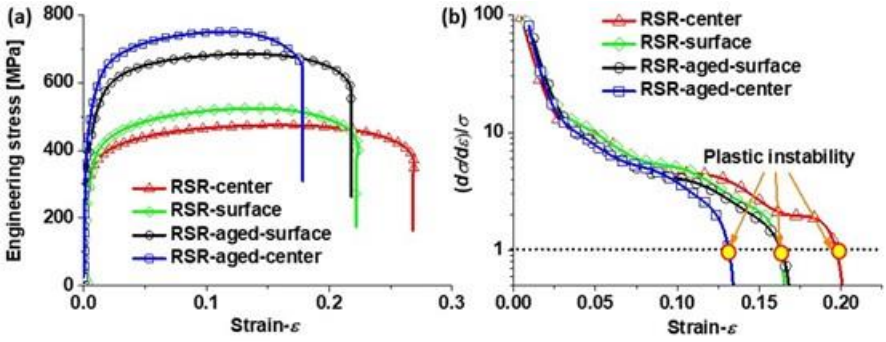

Fig. 9 Mechanical properties at different zones of the samples after RSR and RSR + aging, (a) tensile curves, and (b) Considère criterion evolution.

As a result of the aging of the samples, the ultimate tensile strength increases to 650–750 MPa, the yield strength increases to 557–606 MPa, and the strain to failure lies in the range 0.17–0.22. Although the microstructure shows a marked difference in grain sizes between the surface and the center, the tensile specimens do not correspond precisely to each zone. This is because the specimens' minimum thickness was 1.5 mm, which indicates that the surface sample also considers grains from the central area. Therefore, although the tensile samples cover more than one region, the strength increments due to aging, and the strength-ductility changes between the two zones can still be differentiated—these behaviors in good agreement with the hardness values.

4.22) Page 13, two last sentences of the third paragraph. The grain size is enormous on the surface after aging. Therefore, how can one prove that such an amount of particles are enough to increase the strength? Also, how is it possible to affirm the specific influence of each kind of the second phase? From where the authors got such information?

Answer: *Thank you for the comment. We have added proper references to support our observations. On the other hand, the results from the tensile tests do not exactly correspond to the zone with the big and small grains. The sample's thickness was 1.5mm, which means the surface sample considers both big and small grains.*

As a result of the aging of the samples, the ultimate tensile strength increases to 650–750 MPa, the yield strength increases to 557–606 MPa, and the strain to failure lies in the range 0.17–0.22. Although the microstructure shows a marked difference in grain sizes between the surface and the center, the tensile specimens do not correspond precisely to each zone. This is because the specimens' minimum thickness was 1.5 mm, which indicates that the surface sample also considers grains from the central area. Therefore, although the tensile samples cover more than one region, the strength increments due to aging, and the strength-ductility changes between the two zones can still be differentiated—these behaviors in good agreement with the hardness values. The mechanical properties increase is explained by the presence of two hardened excess phases. The Ni_2Cr phase hardens the alloy due to dispersion hardening through aging, and the Cr_3Si phase increases the strength properties because of the structure heterogenization [40]. As shown in [40], the Cr3Si phase is formed during crystallization and does not depend on subsequent deformation and heat treatment, and thus can prevent grain growth. On the other hand, high strength nickel silicide Ni2Si phase precipitates in the matrix in the form of dispersoids during the aging process.

4.23) Page 14. First paragraph. The sentence before the last. Please, explain why.

Answer: *Thank you for the comment. We have given an explanation.*

$$(\partial\sigma/\partial\varepsilon)/\sigma \leq 1 \qquad (3)$$

This figure shows that the heat-treated material reaches plastic instability first, especially the area near the edge. On the other hand, the central area of the two materials (i.e., RSR and RSR + HT) show similar behaviors in agreement with the microstructure evolution indicated in Fig. 5b and Fig. 5e where similar grain sizes were found. On the other hand, the material deformed by RSR indicates more significant extensions of the homogeneous deformation zone, resulting in plastic instability at higher deformations. This behavior can be associated with the least amount of precipitates in the RSR material leading to a greater mean free path for dislocations movement and larger deformation before fracture. The Considère plot also allows checking the heterogeneity of both materials across the diameter of the bars.

4.24) Page 14. The last paragraph does not appear to be a discussion. It appears to be a description. Furthermore, the explanation given in the last sentence of the paragraph is too poor. Please, discuss and give a better explanation.

Answer: *Thank you for the comment. We have modified the paragraph.*

4.1 Microstructure strengthening

Material heterogeneity is transferred to the deformation evolution as indicated by the strain maps analyzed at the plastic instability points represented in Fig. 8b. In this way, Fig. 9a demonstrates that the RSR material achieves higher deformations than the aged material. Furthermore, strains in the center and surface areas of the deformed material are 43.7% (0.07/0.16) and 40% (0.08/0.2) higher than the average value. This behavior explains the better ductility of the RSR material. On the other hand, for the heat-treated material, Fig. 9b indicates lower deformations along the length of the tensile samples, highlighting that the center area achieves higher strains than the edge region. Therefore, the lower ductility of the aged material is associated with the appearance of several peaks along the length of the tensile sample, as Fig. 9b shows. This behavior can be associated to a more significant number of precipitates that give rise to multiple stress concentration points as a consequence of interaction between precipitates, dislocations and dislocations sources.

4.25) Page15. Figure 10. Please use symbols along with lines in the graphics. Remember that the article will be printed in grayscale. Also, take care. There is an error message there.

Answer: *Thank you for the comment. We have modified the Fig. 10 (now fig. 9) and we fixed the error message.*

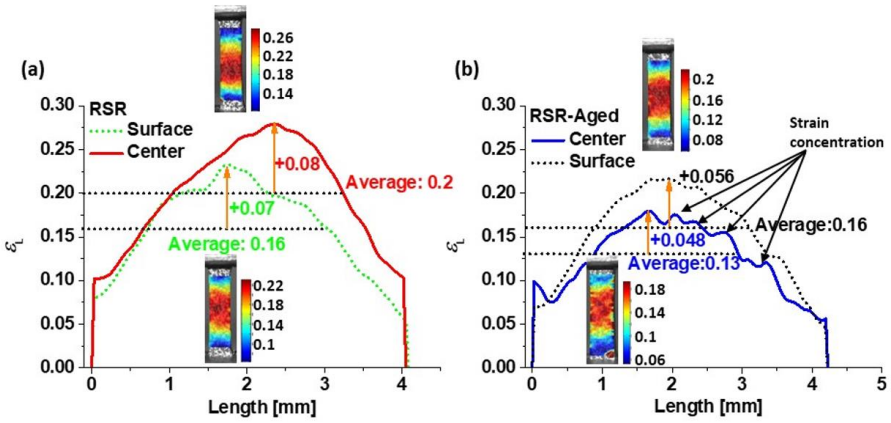

Fig. 10 Strain evolution at the plastic instability points indicated in Fig. 9b, (a) RSR, and (b) RSR+aging.

4.26) Page 15. First paragraph. The different contributions for the strength are not only for copper alloys. Please, modify.

Answer: *Thank you for the comment. We have modified the paragraph.*

Copper and aluminum alloys present different contributions to their strengths, e.g., from lattice friction stress (σ_0), grain size (σ_G), solid solution elements (σ_{SS}), precipitates (σ_P), and dislocations (σ_ρ). Thus, the material yield strength (σ_Y) can be described by the sum of the different components, as indicated by equation (4) [39]:

4.27) Page 15, Equation 4. Sigma0+SigmaG is the Hall-Petch equation. Sigam0 represents the overall resistance of the crystal lattice to dislocation movement. KHP, also known as unpinning constant or "locking parameter", measures the relative hardening contribution of the grain boundaries. So, do not separate Sigma0 from SigmaG.

Answer: *Thank you for the comment. We have followed your suggestions and we included the Hall-Petch term in Fig. 10 (before Fig. 11).*

$$\sigma_G = \frac{k_{HP}}{d^{1/2}} \qquad (5)$$

with k_{HP} as the de Hall-Petch slope, with a value of 112 MPa·μm$^{1/2}$ [40], and d the average grain size. In this way, the first two terms of equation (4) correspond to the Hall-Petch equation, so: $\sigma_{HP} = \sigma_0 + \sigma_G$.

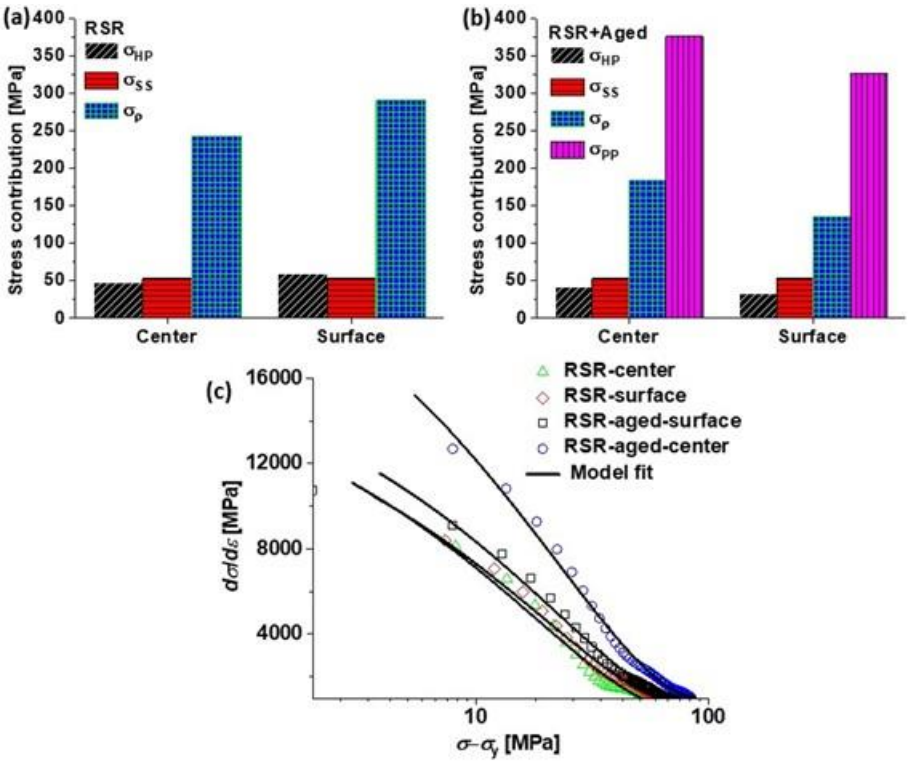

Fig. 11 Strength contributions for the (a) RSR, (b) RSR+aged conditions, and (c) Kock's model fitting.

4.28) Page 15. The authors used a constant value for KHP, which is not constant. It needs to be determined. Please, do it.

Answer: *Thank you for the comment. We appreciate your comment, but we can not follow your recommendation. The main reasons are: We only have two points for each condition (RSR and RSR+Aged) which take us to calculate overestimated or sub-estimated values. The second reason is that the strength values correspond to different hardening mechanisms (Hall-Petch, solid solution, and precipitation). So, we think the constant value is a good approximation to know the different hardening mechanisms for this alloy. On the other hand, the Hall-Petch value used in this study has been used and reported in several investigations with similar processing conditions (i.e., plastic deformation plus aging treatment).*

4.29) Page 15. In Equation 6, what is Ess?

Answer: *Thank you for the comment. We have specified the meaning for the Ess variable.*

$$\sigma_{SS} = M\frac{G\epsilon_{SS}^{3/2}c^{1/2}}{700} \quad (6)$$

where M = 3.06 is the Taylor factor, G the shear module for Ni and Si (77 GPa and 65 GPa, respectively), c the Ni and Si fractions, and ϵ_{SS} is a parameter that correlates the energy from dislocations (edge and screw) with the resolved shear stress per unit solute concentration. ϵ_{SS} can take values of 0.559 and 1.17 for Ni and Si, respectively [36].

4.30) Page 16. First paragraph. If you do not have the value corresponding to the dislocation contribution, how is it possible to get the dislocation density? How did you calculate the mentioned values?

Answer: *Thank you for the comment. The dislocation densities were obtained using equations 4 through 7 for the yield stress state. For the RSR material, we assumed that the precipitation effect was negligible. So, we know the yield stress from the tensile test, the grain boundary contributions from the EBSD measurements, and the solid solution contribution from the alloy's composition. Therefore, the dislocation density contribution can be obtained by subtracting the grain boundary and solid solution contributions from the yield stress.*

$$\sigma_\rho = \alpha MGb\sqrt{\rho} \quad (7)$$

where α = 0.3 is a dislocation hardening constant, M= 3.02 the Taylor factor, G = 44 GPa as the copper shear module, and b = 0.255 nm the matrix Burgers vector. Therefore, for the RSR material, the dislocations' contributions can be obtained assuming that the precipitation effect is absent. From equation (4), contributions of 243 MPa and 291 MPa can be obtained for the surface and center, respectively. Employing equation (7), dislocation densities between 5.7×10^{14} m^{-2} and 8.1×10^{14} m^{-2} can be estimated, which agree with values reported by other investigations. E.g., Watanabe et al. [41], after processing a Cu-Ni-Si alloy using high-pressure torsion (HPT), reported a dislocations density of 8×10^{14} m^{-2}, which remained in the peak aged state and it was reduced to 6×10^{14} m^{-2} in the over-aged state. For the RSR + aged material, the precipitates contribution was obtained as the difference in the aged material's yield strength and the as-cast state.

4.31) Page 17. Figures 11a and b. How did you get the values for individual stress contributions? Also, remove the background colors from the Figures.

Answer: *Thank you for the comment. Strength contributions were obtained using equations 4 through 7. For the RSR material, we assumed that the precipitation effect was negligible. So, we know the yield stress from the tensile test, the grain boundary contributions from the EBSD measurements, and the solid solution contribution from the alloy's composition. Therefore, the*

dislocation density contribution can be obtained by subtracting the grain boundary and solid solution contributions from the yield stress. For the RSR + aged material, we first calculated the precipitation contributions as the yield stress difference between the as-cast and the aged condition. Then, the dislocation contribution was obtained by subtracting the grain boundary, precipitation, and solid solution contributions from the yield stress. We accept that this methodology is not the most appropriate. However, comparing our dislocation density values with other research work for the same alloy, we found that our values are in the same order. When we used the Kocks model in the plastic zone is valid to approximate the dislocation density with the change in the yield stress (i.e., $\rho \propto (\sigma - \sigma_Y)$). *Thus, the change in the density of dislocations with the deformation is proportional to the strain hardening rate* (i.e., $\frac{\partial \rho}{\partial \varepsilon} \propto \frac{\partial \sigma}{\partial \varepsilon}$).

Color background has been removed from Fig. 11(now Fig.10).

$$\sigma_\rho = \alpha M G b \sqrt{\rho} \quad (7)$$

where α = 0.3 is a dislocation hardening constant, M= 3.02 the Taylor factor, G = 44 GPa as the copper shear module, and b = 0.255 nm the matrix Burgers vector. Therefore, for the RSR material, the dislocations' contributions can be obtained assuming that the precipitation effect is absent. From equation (4), contributions of 243 MPa and 291 MPa can be obtained for the surface and center, respectively. Employing equation (7), dislocation densities between 5.7×10^{14} m^{-2} and 8.1×10^{14} m^{-2} can be estimated, which agree with values reported by other investigations. E.g., Watanabe et al. [41], after processing a Cu-Ni-Si alloy using high-pressure torsion (HPT), reported a dislocations density of 8×10^{14} m^{-2}, which remained in the peak aged state and it was reduced to 6×10^{14} m^{-2} in the over-aged state. For the RSR + aged material, the precipitates contribution was obtained as the difference in the aged material's yield strength and the as-cast state.

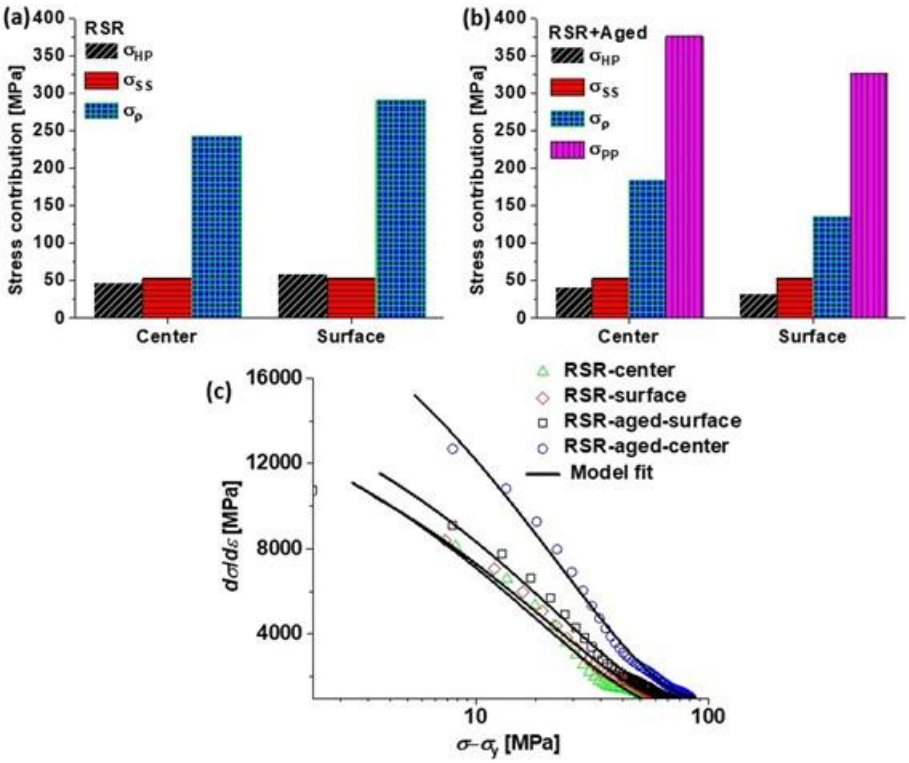

Fig. 11 Strength contributions for the (a) RSR, (b) RSR+aged conditions, and (c) Kock's model fitting.

Using the model proposed by Kocks et al. [44], which describes the rate of change in the density of dislocations with deformation ($\frac{\partial \rho}{\partial \varepsilon}$) as a function of the density of dislocations (ρ), it is possible to know more about dislocations in materials through the following equation:

$$\frac{\partial \rho}{\partial \varepsilon} = M(K_1\sqrt{\rho} - K_2\rho) \quad (8)$$

Where the terms $K_1\sqrt{\rho}$ and $K_2\rho$ describe the storage and recovery or annihilation of dislocations, respectively, and M the Taylor factor. Through Fig. 11c, the adjustment of equation (8) is indicated for each plastic zone of the traction curves of Fig. 9a. When the dislocation density evolution during the tensile test is not known, it can be approximated by the change in the yield stress (i.e., $\rho \propto (\sigma - \sigma_Y)$). Hence, the change in the density of dislocations with the deformation is proportional to the strain hardening rate (i.e., $\frac{\partial \rho}{\partial \varepsilon} \propto \frac{\partial \sigma}{\partial \varepsilon}$).

4.32) Page 18. First paragraph First sentence. Please, change "large-angle" to read "High Angle". Also, the authors have stated about the percentage of HAGB. Probably this information came from EBSD analysis, but you need to tell us and, also, where these data are (tables or something like this).

Answer: *Thank you for the comment. We have changed large-angle for high-angle, and we have also mentioned the table where the values are summarized.*

The aging treatment effect is also reflected in the material grain boundaries character. Table 4 indicates a substantial change in the fraction of high-angle grain boundaries (HAGB) obtained by EBSD from 47% in the RSR state to a microstructure dominated by HAGB with a fraction larger than 97%. Thus, using the equation proposed by Read-Shockley, the energy contributions of the different types of grain boundaries can be quantified [44]:

4.33) Page 20. First paragraph, third sentence (5b). This heterogeneity...). The statement does not explain the faster grain growth. Please, do it.

Answer: *Thank you for the comment. We have explained the faster grain growth on the rod surface due to the heterogeneous strain induced by the RSR process plus the later high temperatures. Therefore, the higher strains near the rod surface than its center and the subsequent heat treatment (960 °C+495 °C) make the most deformed grains around the surface experiment recrystallization followed by abnormal grain growth whereas the center zone only recrystallization.*

4.2 Material heterogeneity

The RSR processing generates a heterogeneous state of deformation between the surface and the center of the bar. This deformation state gives rise to more prominent grain refinement close to the rod surface while the areas away from the surface present a larger grain size (see Fig. 5a and Fig. 5b). This heterogeneity prior to the aging treatment results, in the more deformed areas (that is, a larger number of subgrains, high density of GNDs, and higher energy) after aging in a more accelerated recrystallization phenomenon than in the center of the bars. According to Muñoz et al. [46,47], bars of metallic materials processed by high magnitudes of plastic deformation can generate microstructural gradients when applying high temperatures. This behavior is attributed to the fact that the temperature necessary for recrystallization is lower in the deformed areas than in the less deformed ones. In this direction, since the areas near the surface are more deformed than the center of the bar and the quenching temperature of the aging treatment is much higher than the copper recrystallization temperature (i.e., 960 °C for the quenching followed by the 495 °C for the aging, both higher than 200 °C, copper recrystallization temperature), it is easier to go from recrystallization to abnormal grain growth on the surface than in the center of the rod.

4.34) Page 20, second paragraph. The sentence: On the other hand, after... The statement is related to my previous comment. However, it continues not to explain why there was abnormal grain growth. Please, do it.

Answer: *Thank you for the comment. We have explained the reason for the abnormal grain growth.*

4.2 Material heterogeneity

The RSR processing generates a heterogeneous state of deformation between the surface and the center of the bar. This deformation state gives rise to more prominent grain refinement close to the rod surface while the areas away from the surface present a larger grain size (see Fig. 5a and Fig. 5b). This heterogeneity prior to the aging treatment results, in the more deformed areas (that is, a larger number of subgrains, high density of GNDs, and higher energy) after aging in a more accelerated recrystallization phenomenon than in the center of the bars. According to Muñoz et al. [46,47], bars of metallic materials processed by high magnitudes of plastic deformation can generate microstructural gradients when applying high temperatures. This behavior is attributed to the fact that the temperature necessary for recrystallization is lower in the deformed areas than in the less deformed ones. In this direction, since the areas near the surface are more deformed than the center of the bar and the quenching temperature of the aging treatment is much higher than the copper recrystallization temperature (i.e., 960 °C for the quenching followed by the 495 °C for the aging, both higher than 200 °C, copper recrystallization temperature), it is easier to go from recrystallization to abnormal grain growth on the surface than in the center of the rod.

4.35) Page 21. Second paragraph. The sentences "This apparent contradiction..." and "This effect is because..." The authors need to remember that micron-sized particles will not contribute much to the pinning of dislocation or their multiplication.
The correct case is the one mentioned by Yang et al. In the following sentence. With big particles, you can have reinforcement, but not in the way the authors are trying to say. Please, try to find another explanation.
In this way, the statement in the last sentence of the paragraph is not totally correct. Please, reanalyze and modify it.

Answer: *Thank you for the comment. We have modified the analysis of this paragraph.*

As a consequence of the aging treatment, the recrystallization phenomenon gives rise to larger grain size in the RSR + aged material than in the RSR condition. However, Fig. 13c indicates that, although the grain size in the RSR + aged material is much larger than the RSR, the former's yield strength is greater than that of the latter. This apparent contradiction is supported by the precipitation hardening mechanism. According to various authors and studies using TEM [51,52], the processing of Cu alloys with plastic deformation and subsequent aging heat treatment gives rise to the formation of nanoprecipitates. The authors showed that nanoprecipitates act as elements that pinned the dislocations while dividing them, creating more defects. Therefore, under the influence of stress, nanoprecipitates act as elements that nucleate new dislocations, and that can help to improve ductility. Thus, it can be established and confirmed that the main hardening mechanisms come from dislocations and precipitates.

4.36) Last sentence of page 22. The statement does not explain the effect of second phase particles

and is contradictory to what was previously explained on page 21 concerning the heterogeneity of the microstructure. Please, improve the statement by reanalyzing the data.

Answer: *Thank you for the comment. We have improved the statement.*

4.3 Electroconductivity and hybrid properties

The conductivity measurements are presented in MS/m (megasiemens/meter) and %IACS, that is, as a percentage of pure copper's conductivity (58 MS/m). Fig. 14 shows a diagram of the electrical conductivity values after RSR and aging treatment. At first glance, the heat treatment has a significant effect on electrical conductivity. However, after RSR, the electrical conductivity is 30.52% IACS. Quenching and subsequent aging of the samples lead to an increase in the electrical conductivity value by 48% (Fig. 14). Therefore, the electrical conductivity increment of the aged material is associated with the purification phenomenon of the Cu matrix with precipitates, as demonstrated by the EDS maps and by Yang et al. [48] in a Cu alloy deformed by rolling and subsequent aging treatment.

5 - Conclusions: Despite the number of results, which can be very useful, conclusions are not sound enough. They reflect the uncertainties of the discussion. After performing another data analysis and discussing it, please come back to the conclusions topic to modify it.

Answer: *Thank you for the comment. We have rewritten the conclusions as follows:*

5 Conclusions

The article describes a method for producing semi-finished products from a Cu-Ni-Cr-Si alloy by the radial-shear rolling process.

1. In the radial-shear rolling process, the alloy hardening occurs due to intense shear deformations in the surface layers of the rod, giving rise to microstructure heterogeneity. Subsequent aging treatment leads to precipitation hardening due to the release of Ni_2Cr and Cr_3Si hardener phases dispersed in the matrix as particles uniformly distributed in the bulk of the samples in the form of small inclusions with an average size of 0.56-0.65 μm.

2. The RSR process generates deformation gradients that, after the aging heat treatment, are transformed into recrystallization gradients in the bars' radial direction that give rise to a structural material with a remarkable combination of strength ductility and electrical conductivity. Therefore, the abnormal grain growth results from the deformation gradient across the rod diameter after RSR processing. Thus, the strain heterogeneity between the rod surface and its center zone gives rise to recrystallization gradients after the heat treatment.

3. After RSR, the main strength contribution comes from dislocations. The second contribution is associated with the grain size due to the greater grain refinement. After the aging treatment, the main strength contributions come from the precipitates and dislocation components in both the surface and center areas. This behavior demonstrates the greater strength of the heat-treated material concerning the RSR due to the additional contribution of the precipitates.

4. After RSR and heat treatment, the alloy increased the strength by 50% with elongations ranging between 17-22% and obtaining an electrical conductivity of 45.17% IACS concerning the 30.52% IACS of the RSR material. Thus, the RSR process, together with the appropriate aging heat treatment, allows obtaining a structural heterogeneous copper alloy that stands out among different copper alloys by combining strength, conductivity, and ductility.

5. Hardness and yield strength values infer that the RSR method is a good and versatile alternative for producing bars with diameters in the range of 10-55 mm. The radial-shear rolling method at the large industrial production scale for bars will reduce the tool's cost, the occupied floor space, and equipment downtime associated with the readjustment and replacement of the tool.

Yours sincerely

Dr. Yu.V. Gamin

Corresponding author
On behalf of all authors.

Influence of the Radial-Shear Rolling (RSR) process on the microstructure, electrical conductivity and mechanical properties of a Cu-Ni-Cr-Si alloy

Yu.V. Gamin[1, *], Jairo Alberto Muñoz Bolaños[1, 2, *], A.S. Aleschenko[1], A.A. Komissarov[1], N.S. Bunits[1], D.A. Nikolaev[1], A.V. Fomin[1], V.V. Cheverikin[1]

[1]National University of Science and Technology «MISIS», 4 Leninsky pr., Moscow 119049, Russia.
[2]Instituto de Física Rosario, Consejo Nacional de Investigaciones Científicas y Técnicas-CONICET, Universidad Nacional de Rosario, Ocampo y Esmeralda, 2000 Rosario, Argentina

*Corresponding author email: gamin910@gmail.com.

Abstract

The article describes a method for producing semi-finished products from a copper alloy of the Cu-Ni-Cr-Si system for electrical purposes through the radial-shear rolling (RSR). From the Cu-Ni-Cr-Si alloy by hot deformation, rods with a diameter of 20 mm were obtained, which were then heat treated with quenching and aging. A detailed analysis of the microstructure and properties (mechanical and electrical) of the obtained samples was carried out after RSR and after heat treatment (HT). After RSR, material hardening occurs due to shear deformations forming a gradient structure with grain sizes varying from 8.22 μm to 15.95 μm between the surface and the center of the rod. The microstructure and mechanical property analysis showed that after heat treatment, the alloy is thermally hardened due to the precipitation of Ni_2Si and Cr_3Si particles uniformly distributed in the sample volume in the form of fine inclusions with an average size of 0.56-0.65 μm. After heat treatment, the alloy enhanced its mechanical properties (ultimate tensile strength (UTS) ~ 700-750 MPa, yield strength (YS) ~ 557-606 MPa, and elongation between 17 and 22%) and its electrical conductivity of 45.17% IACS from the 30.52% IACS of the RSR material. The improved mechanical properties of the heat-treated material are due to the different strength contributions mainly coming from dislocations and precipitates. The electrical conductivity improvement after the heat treatment is related to the dislocation density reduction and the increase in grain boundary misorientation due to the recrystallization phenomenon giving rise to a lower number of boundaries but with a twinning character. Thus, the RSR method offers a new industrial alternative for the production of semi-finished products from a Cu-Ni-Cr-Si alloy in the form of rods with diameters ranging from 10-55 mm.

Keywords: *copper alloys; radial-shear rolling; plastic deformation; electroconductivity.*

1 Introduction

Copper-based alloys are one of the most sought-after materials in industry [1]. Due to the good combination of high hardness, thermal and electrical conductivity, such alloys are widely used in electric welding production as contactors, connectors, and other products [2,3]. E.g., rail contact tires made of copper alloys should have high mechanical strength combined with high electrical conductivity [4]. Cu-Cr systems are promising materials for this purpose [5]. Adding small amounts of Zr to a Cu-Cr leads to an increase in strength and ductility properties at elevated temperatures (400-650 °C).

An analogue of the Cu-Cr-Zr alloy for use in electrical engineering is the alloy of the Cu-Ni-Cr-Si system. This alloy possess lower electrical conductivity, but it has improved strength properties, like high wear resistance and temperature stability [6]. For that reason, it has found application in the manufacture of electrodes, tips and parts of resistance welding machines, instrument connectors, and the electrical equipment of transport networks [7].

One way to increase the mechanical properties of materials is to reduce their structure to an ultrafine-grained scale using severe plastic deformation (SPD) [8]. Several investigations describe methods for improving the properties of Cu alloys after SPD by equal channel angular pressing (ECAP) and heat treatment [9,10]. Other methods like screw extrusion and accumulative rolling are also used for producing materials with ultra-fine grain (UFG) structure [11]. For the Cu-Ni-Si-Cr alloy system, some recent investigations are mainly aimed at the evolution of properties during heat treatment in various modes [12].

However, at the moment, the leading industrial methods for producing semi-finished products from copper alloys for electrical purposes are extrusion and drawing [1]. From the manufacturability point of view, the extrusion method has significant disadvantages. These include the inability to quickly reconfigure to a different size and the need for a large number of extrusion tools. To obtain semi-finished products from copper alloys with a high level of operational properties, the application of the radial-shear rolling (RSR) method may be relevant. This method of metal forming has found a full application for producing long round bars of various steel grades [13], titanium alloys [14], and aluminum alloys [15]. Due to the action of shear strains, a spiral-shaped gradient structure is formed with an ultrafine-grained surface layer, which provides an increase in strength properties while maintaining satisfactory ductility [16].

Today, heterogeneous structures have aroused great interest due to their excellent combination of strength and ductility [17,18]. Several methodologies have been proposed to obtain heterogeneous microstructures with different microstructural configurations (for example, heterogeneous distribution of grain sizes, localized distribution of phases in the piece's geometry, heterogeneous dislocation densities, among other characteristics) [17,19–23]. One methodology that has been used is controlled severe plastic deformation applied to sheets, bars, and discs using ECAP and high pressure torsion (HPT), respectively [24–26]. Thus, the initial deformation stages of SPD produce deformation gradients across the sample dimensions. For example, high surface shear strains are obtained after ECAP processing while maintaining its central section less deformed. Although RSR cannot be considered an SPD technique due to the change in the sample's dimensions, it does produce a similar effect between the surface and the center of the deformed material giving rise to a heterogeneous structure [27].

The developed designs of RSR mills allow obtaining long rods (up to 9 m) with different diameters on one set of working tools-rolls [28]. The weight and dimensions of such equipment are significantly lower compared to press equipment. When it is necessary to organize the production of small batches, but a large number of different sized rods, it may be relevant to replace the press equipment with RSR mills. There is no need for a large number of working tools for each bar size; the total weight of the equipment and the occupied floor space is reduced, and the wear resistance of the tool is increased. In this regard, an urgent task may be to study RSR process of copper alloys and compare it with deformation methods used in industry.

The main purpose of this work is to show the capacity of the RSR process for producing semi-finished products from Cu-Ni-Cr-Si alloy with properties quite similar or even better than traditional methods such as extrusion. The RSR process influence was studying by the evolution of microstructure and mechanical properties across the diameter of the rods and the electrical conductivity measurements under the deformed and heat-treated condition.

2 Experimental materials and methods

The initial billet (cylindrical ingot with a diameter of 110 mm) was obtained by chill casting and then deformed by hot pressing until the 60 mm rod diameter. Further, a hot-pressed rod was used for rolling. The initial billet diameter was 60 mm, and the length was 250 mm. Table 1 presents the alloy's chemical composition obtained from the EDS spectrum of several SEM images employing TESCAN VEGA SBH3 scanning electron microscope (SEM-EDS) from Oxford Instruments.

Table 1. Chemical composition of Cu alloy (% wt.)

Alloy	Cu	Ni	Cr	Si	Al	Zn	Fe	Other
Cu-Ni-Cr-Si	95.04	2.89	1.03	0.92	0.03	0.08	0.03	≤ 0.1

Table 2 summarizes the alloy's experimental electrical conductivity and mechanical properties.

Table 2. Experimental properties of Cu-Ni-Cr-Si alloy in the initial state

Parameter name	Value
Hardness (HV)	130-150
Ultimate tensile strength (MPa)	340-380
Yield strength (MPa)	220-240
Elongation (%)	20
Electrical conductivity (MS/m)	22.3

The initial billets were deformed in the hot state by radial-shear rolling. RSR was carried out at the semi-industrial rolling mill located in the laboratory of the Department of Metal forming (NUST "MISIS", Moscow). The mills are equipped with three work rolls that are deployed at a feed angle β and a toe angle δ, as indicated in previous studies [29]. Work rolls located symmetrically concerning the central rolling axis form a deformation zone rotating in one direction and deforming the workpiece. The sample moves along the deformation zone following a helicoidal path.

Before deformation, the initial billet was heated in a chamber furnace for 2 hours to a temperature of 900 °C. Rolling was carried out in 4 passes following the modes summarized in Table 3. After each pass, the bar returned to the furnace to equalize the temperature over the entire cross section. The rotary velocity of the working rolls was 30 rpm.

The elongation ratio (μ_i) for the i pass is defined as the ratio of the cross-sectional area of the bar in the ($i-1$) pass (F_{i-1}) to the cross-sectional area of the bar in the i pass (F_i):

$$\mu_i = \frac{F_{i-1}}{F_i} = \frac{D_{i-1}^2}{D_i^2} \quad (1)$$

Where D_{i-1} and D^2 represent the initial and final rod diameter, respectively.

The total elongation ratio for several passes is defined as the ratio of the cross-sectional area of the initial billet (F_0) to the cross-sectional area of the bar after the last pass (F_n):

$$\sum_{i=1}^{n} \mu_i = \frac{F_0}{F_n} = \mu_1 \cdot \mu_2 \cdot \mu_3 \cdot \ldots \cdot \mu_n \quad (2)$$

Table 3. Deformation conditions of Rolling.

Pass Number, i	Diameter of workpiece D_{i-1}, mm	Diameter of the resulting rod D_i, mm	Elongation ratio μ_i	$\Sigma\mu_i$
1	60	46	1.70	1.70
2	46	36	1.63	2.78
3	36	28	1.65	4.60
4	28	20	1.96	9.00

After RSR, heat treatment was performed, which consisted of quenching and aging. The heat treatment cycle for the studied alloy is shown in Fig. 1.

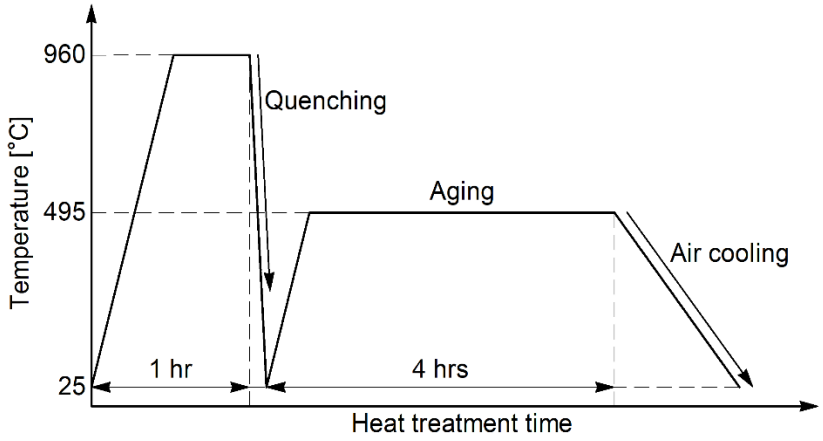

Fig. 1 Heat treatment diagram for Cu-Ni-Cr-Si alloy.

For the 20 mm diameter rods after RSR and heat treatment, electrical conductivity and microhardness distribution over the cross and longitudinal sections were measured. The microstructure was analyzed across the radial direction in three zones: i.e., the surface, the middle of the radius, and the center. Fig. 2a illustrates the microhardness measurement scheme and the microstructure analysis zones.

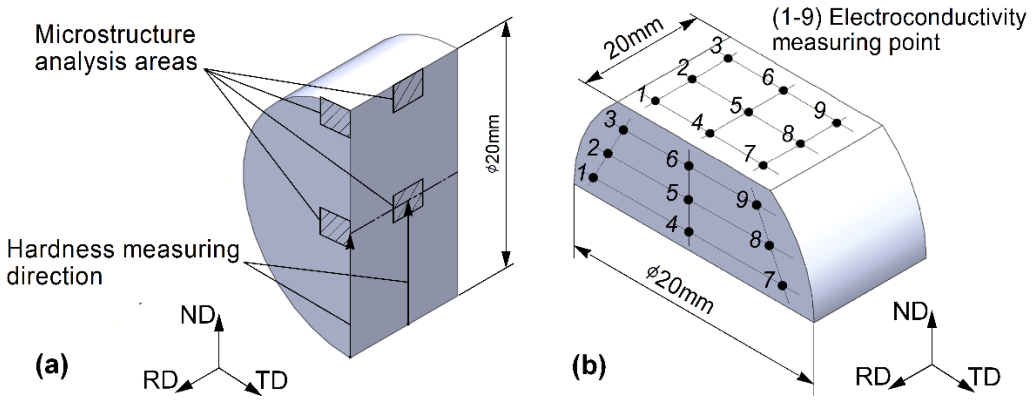

Fig. 2 Microstructure and hardness measurement scheme (a), and electroconductivity measurement scheme (b).

The microstructure was studied using a Carl Zeiss Axio Lab.A1 optical microscope. The microhardness of specimens was measured by the Vickers method (HV) on a DUROLINE MH-6 durometer (load 300 g, dwell time of 30 s). The electrical conductivity of the samples was measured at eddy current structuroscope (Scientific Research Institute of Introscopy "Srektr", Russia) at 9 points in parallel and perpendicular to the rolling direction (Fig. 2b). The final value was determined as the average value of measurements at all points.

For better understanding the microstructural characteristics of the material processed by RSR and after the aging heat treatment, a TESCAN VEGA SBH3 scanning electron microscope (SEM-EDS) from Oxford Instruments was used. The material's microstructure was analyzed at different points on the cross-sectional area of the bars using electron back-scattering diffraction (EBSD). The samples were prepared by mechanical polishing using SiC sandpaper up to 2500 granulometry and subsequent fine polishing with diamond pastes of 9 µm, 6 µm 1 µm and colloidal silica with a particle size of 0.05 µm. Data were analyzed using TSL-OIM 7 and Mtex toolbox. Grains with less than two pixels were not considered in the statistical analysis. Grain boundaries with misorientations between 3° and 15° were defined as low-angle grain boundaries (LAGB). Those with misorientations greater than 15° as high-angle grain boundaries (HAGB).

The analysis of the phase composition was carried out using the X-Ray diffraction method by the Multifunctional X-ray diffractometer DRON-8. The following parameters were used for scanning: voltage 40 kV, Amperage 20 mA, scanning step 0.05°, exposure time 4 s - discrete mode, PDF-2 Release 2014 ICDD database.

Tensile tests in different zones across the sample diameter (surface and center) were evaluated using a universal testing machine at room temperature. Sample gauge dimensions of 4 mm x 1.5 mm x 2 mm tested at a constant strain rate of $1 \cdot 10^{-3}$ s^{-1}. Strain maps were obtained

by digital image correlation (DIC) during the tensile test employing the Ncorr free software [30].

3 Results and analysis

3.1 As-received material

The initial material was obtained by casting, obtaining bars of 110 mm in diameter. Thus, Fig. 3a indicates the microstructure obtained by optical microscopy (OM) after casting. This figure shows the formation of a structure of coarse grains of different sizes. Due to the solidification process in which the surfaces are cooled before the central zone, a variation in grain size occurs, as indicated in Fig. 3b. This figure indicates the existence of two families of grain size, one formed by sizes smaller than 3 mm located around the surface with an average value of 0.92 mm and the other comprising sizes between 4 mm and 8 mm located preferably in the center of the bar with an average value of 4.83 mm. Concerning alloy tensile behavior, Fig. 3c indicates that the as-cast material reaches a yield strength of 220 MPa with a fracture strain of 20%. Additionally, the EBSD characterization in Fig. 3d confirms a microstructure with large grains. Those grains are free of dislocations and substructures in its interior, as confirmed by the misorientation profile lines 1-2 and 3-4 in Fig. 3e. The misorientation profiles show constant behaviors inside the grains, and only appreciable changes in misorientation occur when crossing the grain boundaries. This yield strength reflect the effect of the alloying elements in the material, i.e., an increase in yield strength of 60% concerning high-purity electrolytic copper (87 MPa, yield strength) [31].

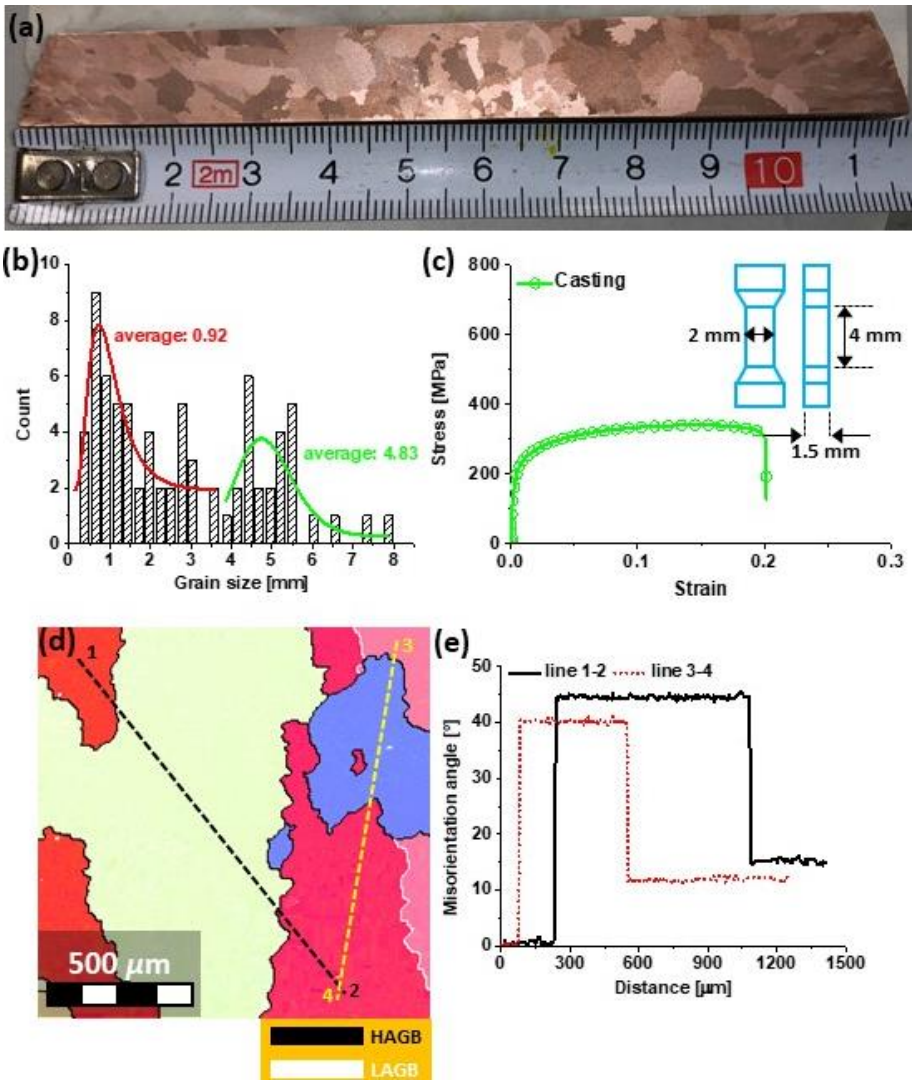

Fig. 3 Initial microstructure after casting process (a), grain size in the casting condition (b), tensile properties (c), EBSD map (d), and misorientation profiles for the lines indicated in the EBSD map (e).

3.2 Processed material

Fig. 4 display the microstructure of the rods after RSR and RSR plus heat treatment, respectively. In the RSR process, a gradient structure is formed, with a spiral morphology that reflects the helicoidal motion of metal layers in the deformation zone [16,32,33]. Fig. 4a and Fig. 4c allows seeing that the microstructure around the surface in cross-section after RSR is mainly formed by small grains with an average size of 8.22 µm. The smallest grain size is formed here due to the localization of severe shear deformations in the surface layer. Conversely, the central zone in Fig. 4b, and Fig. 4c shows a mix of small and large grain sizes ranging between 2 µm and 40 µm, with an average grain size of 15.9 µm. This effect is attributed to the heterogeneous equivalent strain distribution along the radial direction.

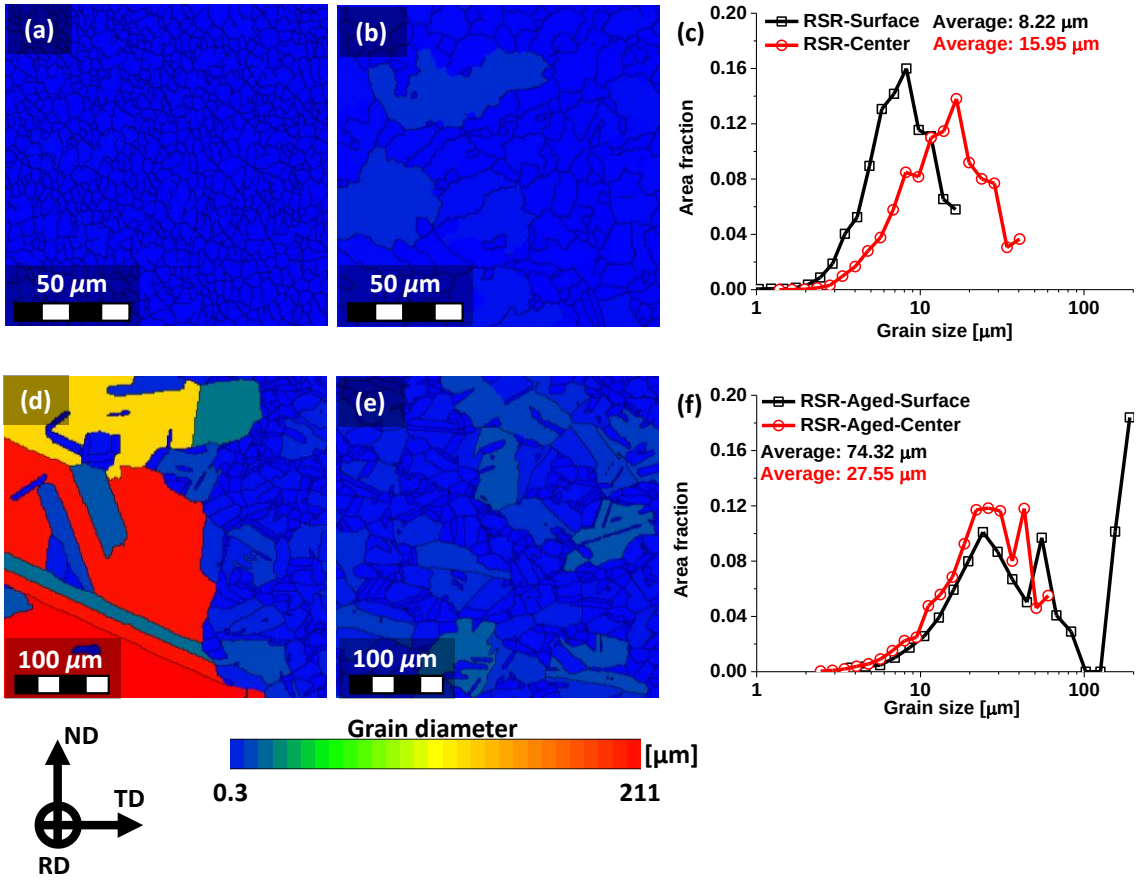

Fig. 4 Surface grain diameter map after RSR (a), center grain diameter map after RSR (b), grain size evolution after RSR (c), surface grain diameter map after RSR+aging (d), center grain diameter map after RSR+aging (e), grain size evolution after RSR+aging (f).

In the hardening process by heat treatment, Fig. 4d through Fig. 4f manifests an evident grain structure change. After the heat treatment, grain recrystallization occurs in a heterogeneous way, as the grain size increases, especially in the surface layer, which may be due to different deformation degree induced by the RSR process across the rod diameter. After the aging treatment, the microstructure evolution in Fig. 4d and Fig. 4e shows the opposite behavior concerning the RSR material. The average grain size in the central part of the rod after heat treatment is 27.5 μm. At the surface of the rod, coarse grains larger than 100 μm in size are observed, while the average grain size, according to measurements, is 74.32 μm. Besides, in the microstructure of samples after heat treatment, one can observe characteristic annealing twins formed during grain growth. Therefore, the abnormal grain growth is a consequence of the deformation gradient across the rod diameter after RSR processing. Thus, the strain heterogeneity between the rod surface and its center zone gives rise to recrystallization gradients after the heat treatment.

To better describe microstructural characteristics, energy dispersive spectroscopy (EDS) analyses were performed. Fig. 5a indicates the material's microstructure after RSR processing plus aging treatment, indicating the different regions analyzed (red squares). The SEM image allows observing the grain boundaries and the presence of particles of different sizes. In Fig. 5b, the main alloying elements' EDS map is indicated for the spectrum area 1. At first glance, it can be assessed that Ni and Cu concentrations are homogeneously distributed throughout the material. On the contrary, Cr and Si elements seem to be located in small regions forming particle colonies close to the grain boundaries. Fig. 5c shows the EDS spectra for the different areas indicated in Fig. 5a. Spectrum number 1, corresponding to the entire analyzed area shows alloying elements such as Ni, Cr, and Si. Looking in more detail at spectra 2 and 3, corresponding to the black particles observed in Fig. 5a, we see a high Si and Cr concentrations. On the other hand, spectra 4 and 5 within the grains indicate low concentrations of Cr and Si and a domain of Cu and Ni. In this way, the previous observations confirm the formation of precipitates rich in Cr, and Si with a Ni matrix enriched. Looking in more detail at the EDS maps for Cu, Si, Ni, and Cr in Fig. 5d, we see that many of the high Si concentration spots also show high Cr content. According to Rdzawski et al. [34], these particles with a high content of Cr and Si correspond to Cr_3Si precipitates, which are preferentially located around the grain boundaries.

Aging treatment also favors the precipitation of Ni_2Si phases in the matrix as particles uniformly distributed in the bulk of the samples in the form of small inclusions. Cheng et al. [35] also reported the formation of this type of precipitates after aging at a temperature of 500 °C for a Cu-Ni-Si-Cr alloy. Analyzing the EDS images for each element using ImageJ [36], an appreciation of the precipitate particles' size can be made, as indicated in Fig. 6. The histograms show an average particle size between 0.56 μm and 0.65 μm that follows a lognormal function. The inset in Fig. 6 highlights a microstructure where some small particles appear either inside the grains (blue ellipse) or forming colonies close to the grain boundaries (green ellipse). However, several authors have reported via TEM that after plastic deformation, the Cu-Cr-Ni-Si alloy can form nano-precipitates with average sizes of 8 nm [35,37]. Therefore, the analyses from the SEM images represent a more descriptive than quantitative result of the precipitates' real size.

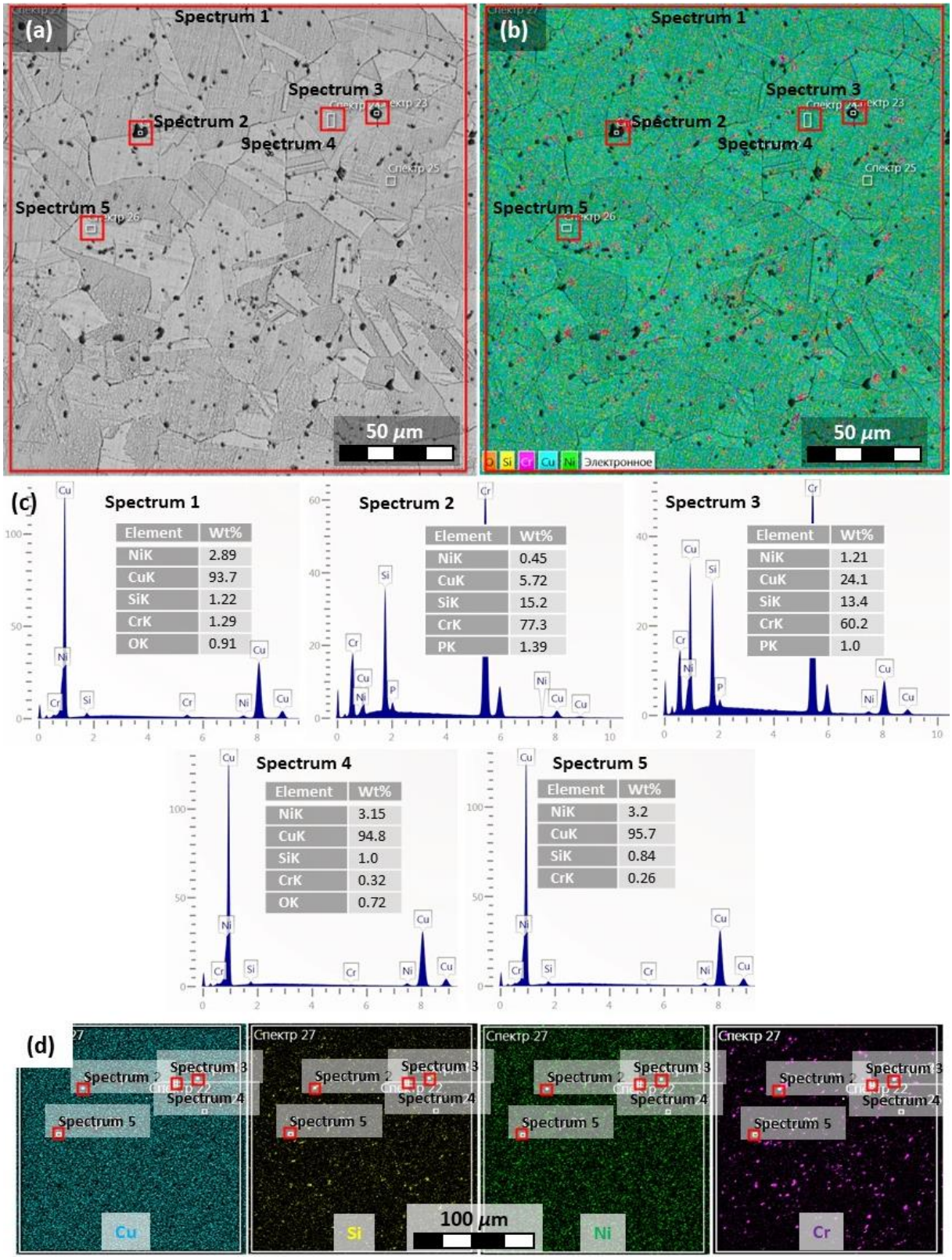

Fig. 5 SEM map after aging treatment (a), EDS map (b), EDS spectrums for the red squares indicated in figure (a) (c), and Cu, Si, Ni, and Cr EDS maps (d)

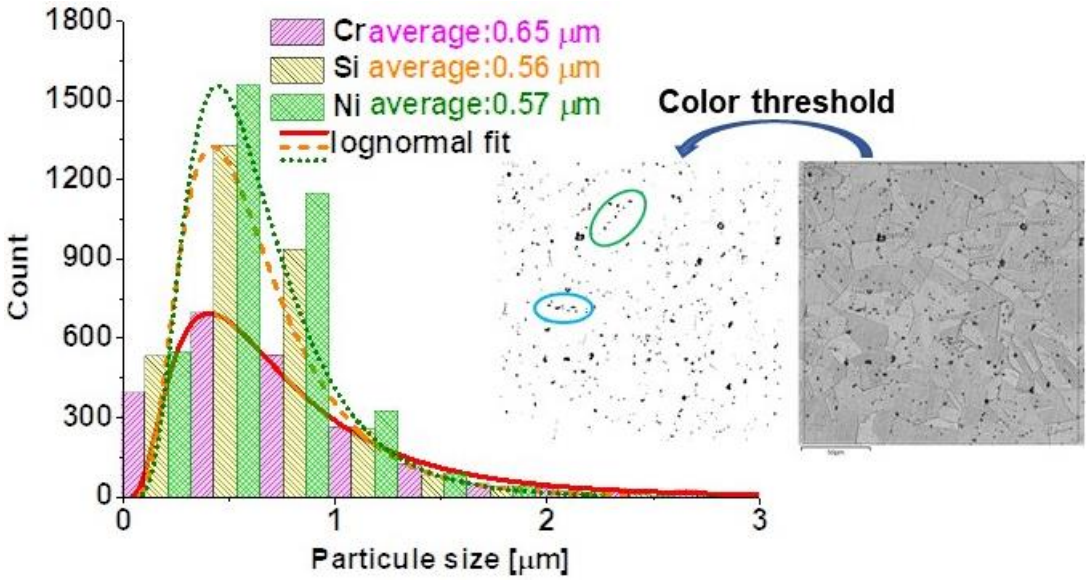

Fig. 6 Precipitation particles sizes.

X-ray diffraction confirms the formation of different types of precipitates such as Cr_3Si and Ni_2Si. Fig. 7 shows the diffraction patterns for samples after RSR and aging heat treatment. It can be seen that the chromium silicide and nickel silicide phase concentrations are about 0.84% and 0.9%, respectively. Samoilova et al. [38] showed that for the Cu-3%Ni-1.5%Si-1%Cr alloy, the main phases observed after heat treatment are Cr_3Si and Ni_2Si. The formation of these precipitates suggests the activation of an additional hardening mechanism in the material processed by RSR and subsequently heat treated.

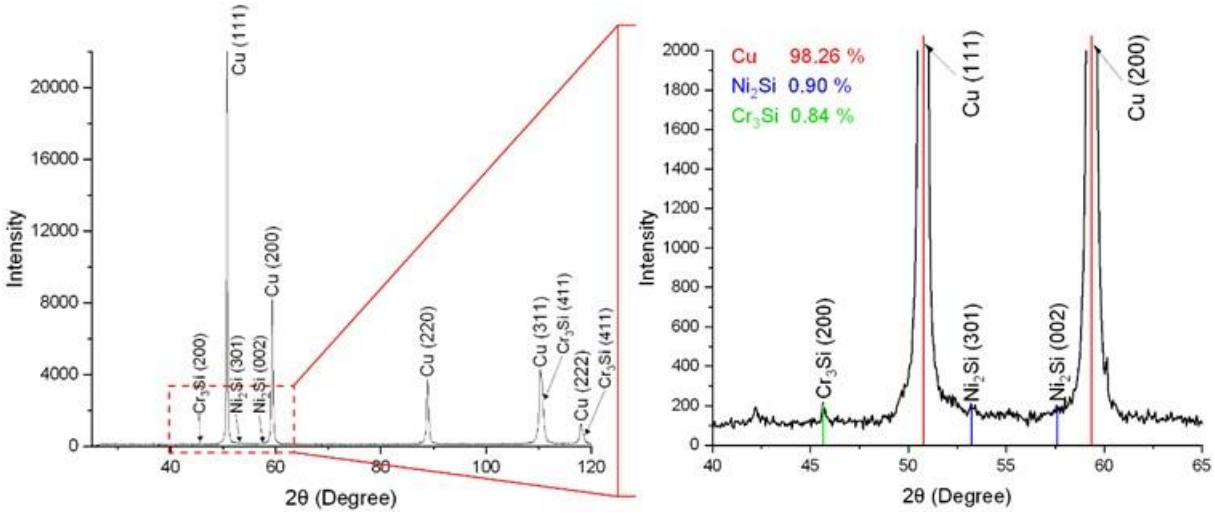

Fig. 7 Diffraction pattern for the Cu-Ni-Cr-Si alloy after RSR + Aging treatment

3.3 Mechanical properties

Fig. 8 shows the hardness distribution in the cross section for both conditions RSR and heat-treated RSR. The RSR material shows some hardness variation from the surface to the rod center. The opposite behavior is observed in the heat-treated RSR material, where hardness values are high close to the center and decrease near the surface. Additionally, a hardness value of ~260-280 HV above the ~180-200 HV of the RSR condition was obtained after the aging treatment representing a hardness increment of 40-45%.

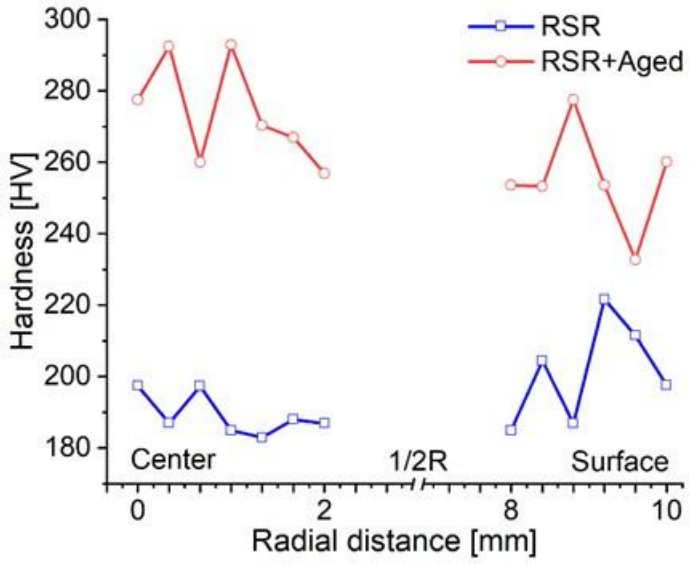

Fig. 8 Hardness evolution in the cross section after RSR and RSR + aging treatment.

According to the standard specifications for this alloy, the Vickers hardness of hot-pressed rods should not be lower than 200 HB (210 HV) [39]. Thus, the obtained hardness values for aged samples are higher than the standard values.

Fig. 9a illustrates typical engineering stress-strain curves for samples subjected to RSR and aging treatment. It worth mentioning that the samples cut near the surface of the rod and in its center region differ on their mechanical strengths, what is explained by the microstructure heterogeneity of the samples in those zones. After hot radial-shear rolling with a total elongation ratio μ = 9.0, the ultimate tensile strength is ~ 480-520 MPa, the yield strength is about 355-392 MPa. At the same time, the strain to failure lies typically around 0.22 and 0.27 for the center and surface samples, respectively.

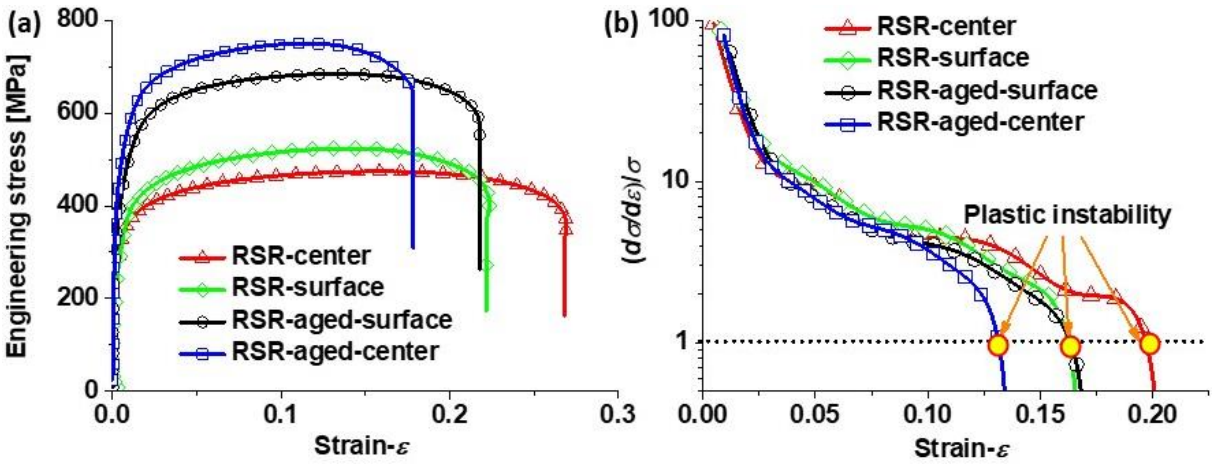

Fig. 9 Mechanical properties at different zones of the samples after RSR and RSR + aging, (a) tensile curves, and (b) Considère criterion evolution.

As a result of the aging of the samples, the ultimate tensile strength increases to 650–750 MPa, the yield strength increases to 557–606 MPa, and the strain to failure lies in the range 0.17–0.22. Although the microstructure shows a marked difference in grain sizes between the surface and the center, the tensile specimens do not correspond precisely to each zone. This is because the specimens' minimum thickness was 1.5 mm, which indicates that the surface sample also considers grains from the central area. Therefore, although the tensile samples cover more than one region, the strength increments due to aging, and the strength-ductility changes between the two zones can still be differentiated—these behaviors in good agreement with the hardness values. The mechanical properties increase is explained by the presence of two hardened excess phases. The Ni_2Si phase hardens the alloy due to dispersion hardening through aging, and the Cr_3Si phase increases the strength properties because of the structure heterogenization [40]. As shown in [40], the Cr_3Si phase is formed during crystallization and does not depend on subsequent deformation and heat treatment, and thus can prevent grain growth. On the other hand, high strength nickel silicide Ni_2Si phase precipitates in the matrix in the form of dispersoids during the aging process.

Additionally, Fig. 9b represents the Considère criterion evolution for the tensile curves of Fig. 9a. This criterion establishes that the appearance of plastic instability occurs when the strain hardening rate $(\partial\sigma/\partial\varepsilon)$ equals the flow stress (σ) of the material according to the following equation [41]:

$$(\partial\sigma/\partial\varepsilon)/\sigma \leq 1 \qquad (3)$$

This figure shows that the heat-treated material reaches plastic instability first, especially the center area. On the other hand, the surface area of the two materials (i.e., RSR

and RSR + HT) show similar behaviors. On the other hand, the material deformed by RSR indicates more significant extensions of the homogeneous deformation zone, resulting in plastic instability at higher deformations. This behavior can be associated with the fewer number of precipitates in the RSR material leading to a greater mean free path for dislocations movement and larger deformation before fracture. The Considère plot also allows checking the heterogeneity of both materials across the diameter of the bars.

4 Discussion

The processing of the alloy by RSR produces heterogeneity in the material, what can influence its properties, giving it a combination of unusual properties such as good strength and ductility or good strength keeping good electrical conductivity. In this way, the discussion of the results obtained in this work will focus on microstructural and mechanical heterogeneity.

4.1 Microstructure strengthening

Material heterogeneity is transferred to the deformation evolution as indicated by the strain maps analyzed at the plastic instability points represented in Fig. 9b. In this way, Fig. 10a demonstrates that the RSR material achieves higher deformations than the aged material. Furthermore, strains in the center and surface areas of the deformed material are 40% (0.08/0.2) and 43.7% (0.07/0.16) higher than the average value. This behavior explains the better ductility of the RSR material. On the other hand, for the heat-treated material, Fig. 10b indicates lower deformations along the length of the tensile samples, highlighting that the surfer area achieves higher strains than the center region. Therefore, the lower ductility of the aged material is associated with the appearance of several peaks along the length of the tensile sample, as Fig. 10b shows. This behavior can be associated to a more significant number of precipitates that give rise to multiple stress concentration points as a consequence of interaction between precipitates, dislocations and dislocations sources.

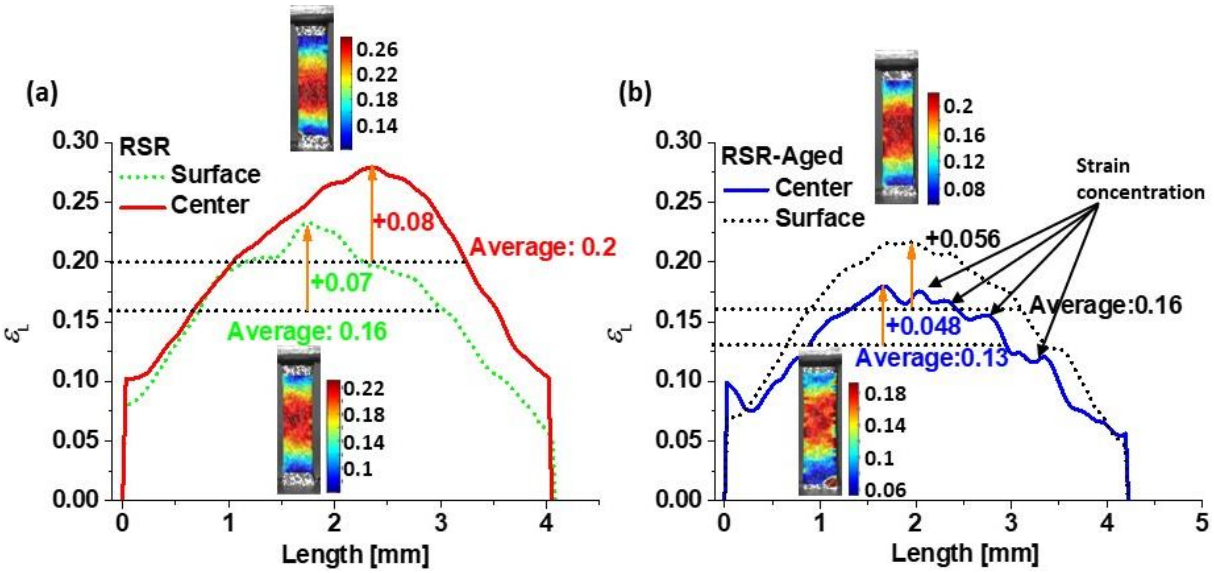

Fig. 10 Strain evolution at the plastic instability points indicated in Fig. 9b, (a) RSR, and (b) RSR+aging.

Copper and aluminum alloys present different contributions to their strengths, e.g., from lattice friction stress (σ_0) equal to 20 MPa [37], grain size (σ_G), solid solution elements (σ_{SS}), precipitates (σ_P), and dislocations (σ_ρ). Thus, the material yield strength (σ_Y) can be described by the sum of the different components, as indicated by equation (4) [42]:

$$\sigma_Y = \sigma_0 + \sigma_G + \sigma_{SS} + \sigma_P + \sigma_\rho \tag{4}$$

Where the grain size contribution follows the next equation:

$$\sigma_G = \frac{k_{HP}}{d^{1/2}} \tag{5}$$

with k_{HP} as the de Hall-Petch slope, with a value of 112 MPa·μm$^{1/2}$ [43], and d the average grain size. In this way, the first two terms of equation (4) correspond to the Hall-Petch equation, so: $\sigma_{HP} = \sigma_0 + \sigma_G$.

The solid solution contribution from Ni and Si can be expressed by the next equation:

$$\sigma_{SS} = M\frac{G\epsilon_{SS}^{3/2}c^{1/2}}{700} \tag{6}$$

where M = 3.06 is the Taylor factor, G the shear module for Ni and Si (77 GPa and 65 GPa, respectively), c the Ni and Si fractions, and ϵ_{SS} is a parameter that correlates the energy from dislocations (edge and screw) with the resolved shear stress per unit solute concentration. ϵ_{SS} can take values of 0.559 and 1.17 for Ni and Si, respectively [37].

On the other hand, the dislocation contribution can be obtained through the equation (7):

$$\sigma_\rho = \alpha M G b \sqrt{\rho} \tag{7}$$

where α = 0.3 is a dislocation hardening constant, M= 3.02 the Taylor factor, G = 44 GPa as the copper shear module, and b = 0.255 nm the matrix Burgers vector. Therefore, for the RSR material, the dislocations' contributions can be obtained assuming that the precipitation effect is absent. From equation (4), contributions of 291 MPa and 243 MPa can be obtained for the surface and center, respectively. Employing equation (7), dislocation densities between 8.1×10^{14} m^{-2} and 5.7×10^{14} m^{-2} can be estimated, which agree with values reported by other investigations. E.g., Watanabe et al. [44], after processing a Cu-Ni-Si alloy using high-pressure torsion (HPT), reported a dislocations density of 8×10^{14} m^{-2}, which remained in the peak aged state and it was reduced to 6×10^{14} m^{-2} in the over-aged state. For the RSR + aged material, the precipitates contribution was obtained as the difference in the aged material's yield strength and the as-cast state.

In this way, Fig. 11 collects the different strength contributions of the materials obtained through equations (4)-(7). Fig. 11a indicates how the main strength contribution comes from dislocations. It is also shown that in the surface zone, the second contribution associated with the grain size is due to the bigger grain refinement in this area, as shown in Fig. 4a. After the aging treatment, Fig. 11b shows that the main strength contributions come from the precipitates and dislocations components in both the surface and center areas. This behavior demonstrates the greater strength of the heat-treated material concerning the RSR as a consequence of the additional contribution of the precipitates. Fig. 11b shows that the aging treatment generated larger amounts of precipitates near the center due to a possible recrystallization gradient as a consequence of the microstructure heterogeneity after the RSR process. Thus, hardness and the yield strengths values lead to infer that the RSR method is a good and versatile alternative for the production of rods with diameters in the range of 10-55 mm.

Using the model proposed by Kocks et al. [45], which describes the rate of change in the density of dislocations with deformation ($\frac{\partial \rho}{\partial \varepsilon}$) as a function of the density of dislocations (ρ), it is possible to know more about dislocations in materials through the following equation:

$$\frac{\partial \rho}{\partial \varepsilon} = M(K_1\sqrt{\rho} - K_2\rho) \quad (8)$$

Where the terms $K_1\sqrt{\rho}$ and $K_2\rho$ describe the storage and recovery or annihilation of dislocations, respectively, and M the Taylor factor. Through Fig. 11c, the adjustment of equation (8) is indicated for each plastic zone of the traction curves of Fig. 9a. When the dislocation density evolution during the tensile test is not known, it can be approximated by the change in the yield stress (i.e., $\rho \propto (\sigma - \sigma_Y)$). Hence, the change in the density of dislocations with the deformation is proportional to the strain hardening rate (i.e., $\frac{\partial \rho}{\partial \varepsilon} \propto \frac{\partial \sigma}{\partial \varepsilon}$).

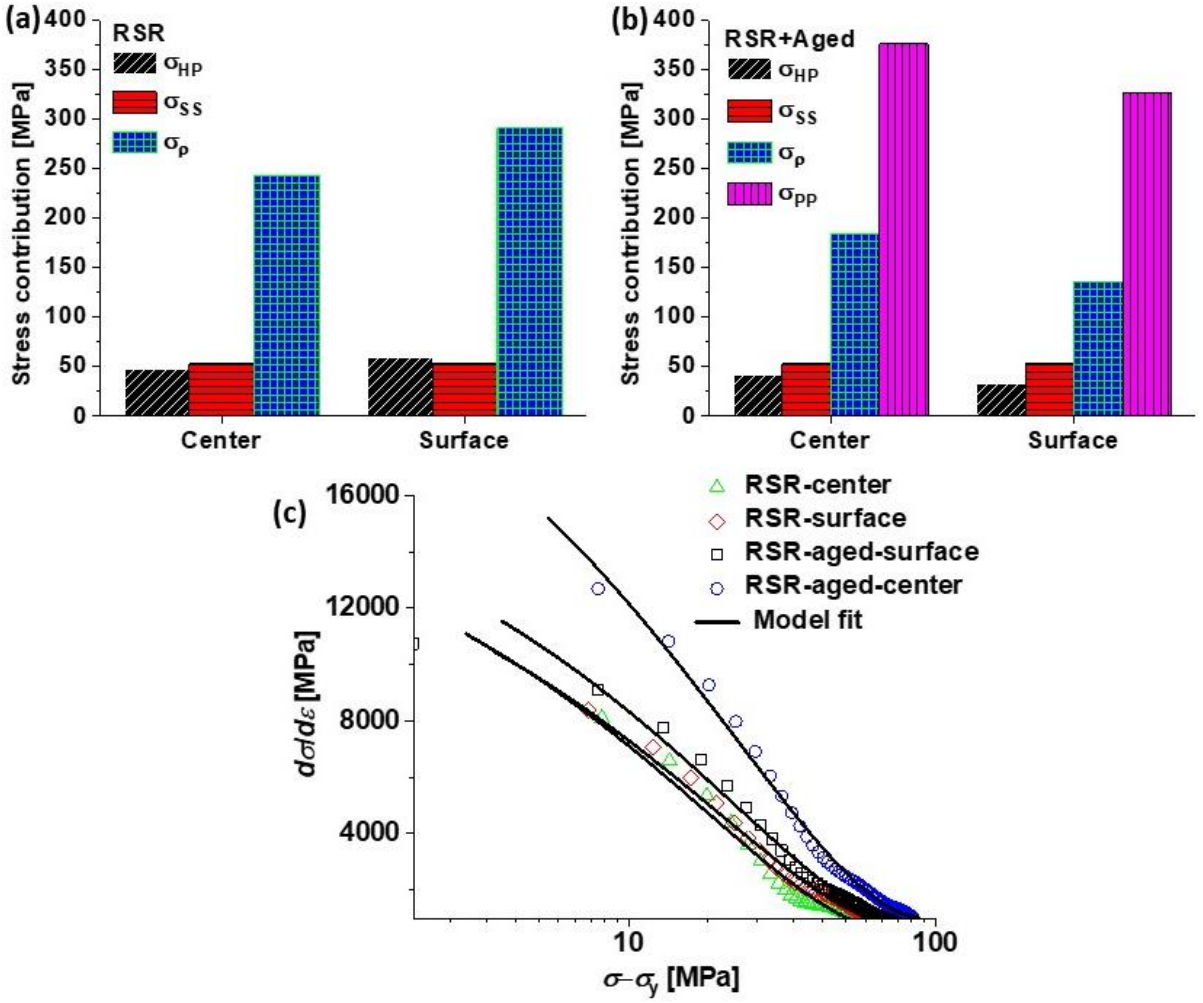

Fig. 11 Strength contributions for the (a) RSR, (b) RSR+aged conditions, and (c) Kock's model fitting.

The curve fits show good correlations that allow the calculation of K_1 and K_2 values as summarized in Table 4 for the different conditions and areas analyzed. Initially, it is observed that the surface of the material processed by RSR register greater values for both the K_1 and K_2

coefficients than the center. Conversely, the RSR + aged material exhibits the oppositive behavior, i.e., greater values for both the K_1 and K_2 in the center than in the surface. However, between the two conditions, there is a marked difference for the coefficients. The RSR + aged material has a lower dislocation multiplication rate of approximately half of the one for RSR material. On the other hand, the dislocation annihilation rate in RSR + aged material is lower than in RSR. This behavior is due to the lower density of dislocations in the RSR + aged material due to the previous annihilation of dislocations by the solubilization and aging treatment. However, it should be noted that the dislocation annihilation magnitudes are much lower than those observed in severe plastic deformation processes where magnitudes close to 1000 are reached for the K_2 coefficient [46]. Thus, the low dislocation annihilation rate suggests a good strain hardening capacity in the RSR + aged material.

The aging treatment effect is also reflected in the material grain boundaries character. Table 4 indicates a substantial change in the fraction of high-angle grain boundaries (HAGB) obtained by EBSD from 47% in the RSR state to a microstructure dominated by HAGB with a fraction larger than 97%. Thus, using the equation proposed by Read-Shockley, the energy contributions of the different types of grain boundaries can be quantified [47]:

$$\gamma(\theta) = \begin{cases} \gamma_m \frac{\theta}{15}\left[1 - ln\left(\frac{\theta}{15}\right)\right], if\ \theta \leq 15° \\ \gamma_m, if\ \theta > 15° \end{cases} \quad (9)$$

With $\gamma_{\mathrm{m}} = 0.625$ J/m^2 representing the energy per unit area of a HAGB and θ the misorientation angles. Hence, the average energy ($\bar{\gamma}$) is obtained as the sum of the different contributions of the misorientation angles as indicated in the following equation [47]:

$$\bar{\gamma} = \sum_{2}^{63.5} \gamma(\theta) f(\theta) \quad (10)$$

where $f(\theta)$ is the fraction of a determined misorientation. While the energy stored in grain edges can be obtained through the following equation [47]:

$$E_b = \frac{2\bar{\gamma}}{d_{sub-grain}} \quad (11)$$

Solving equations (9)-(11), the energy stored in the grain boundaries is obtained as indicated in Table 4. Despite the average energy increases after the aging treatment due to the increase in

the HAGB fraction, the boundary stored energy decreases as a consequence of the subgrain growth. This behavior shows that the increase in the temperature in the material due to the heat treatment after RSR processing produces abnormal grain growth and a reduction in stored dislocations, especially geometrically necessary dislocations (GNDs).

Table 4. Microstructural properties

Condition	K_1	K_2	%HAGB	ρ [m^{-2}]	$d_{\mathrm{sub-grain}}$ [μm]	$\bar{\gamma}$ [J/m^2]	E_b [J/g]
RSR-surface	1.1×10^{10}	126.8	47.2	8.1×10^{14}	3.20	0.52	0.036
RSR-center	9.8×10^{9}	112.9	40.7	5.7×10^{14}	7.14	0.50	0.016
RSR-aged-surface	3.8×10^{9}	54.8	98.1	1.7×10^{14}	13.05	0.62	0.011
RSR-aged-center	4.6×10^{9}	63.7	97.9	2.1×10^{14}	11.85	0.62	0.012

Fig. 12 shows the substantial change in the grain boundaries' misorientations, highlighting different types of boundaries. For example, it is noted that the material properties after RSR processing are dominated by low-angle grain boundaries (LAGB) with small fractions of twins and coincident sites lattice (CSL), especially in the surface area. Conversely, after aging, the presence of misorientation peaks for angles of 38.9° and 60° corresponding to twins of the type ⟨110⟩ and ⟨111⟩, respectively, is appreciated. Therefore, the RSR+aged material boundaries are mainly formed by a high fraction of twins and CSL, as indicated by the misorientation distributions and the CSL maps.

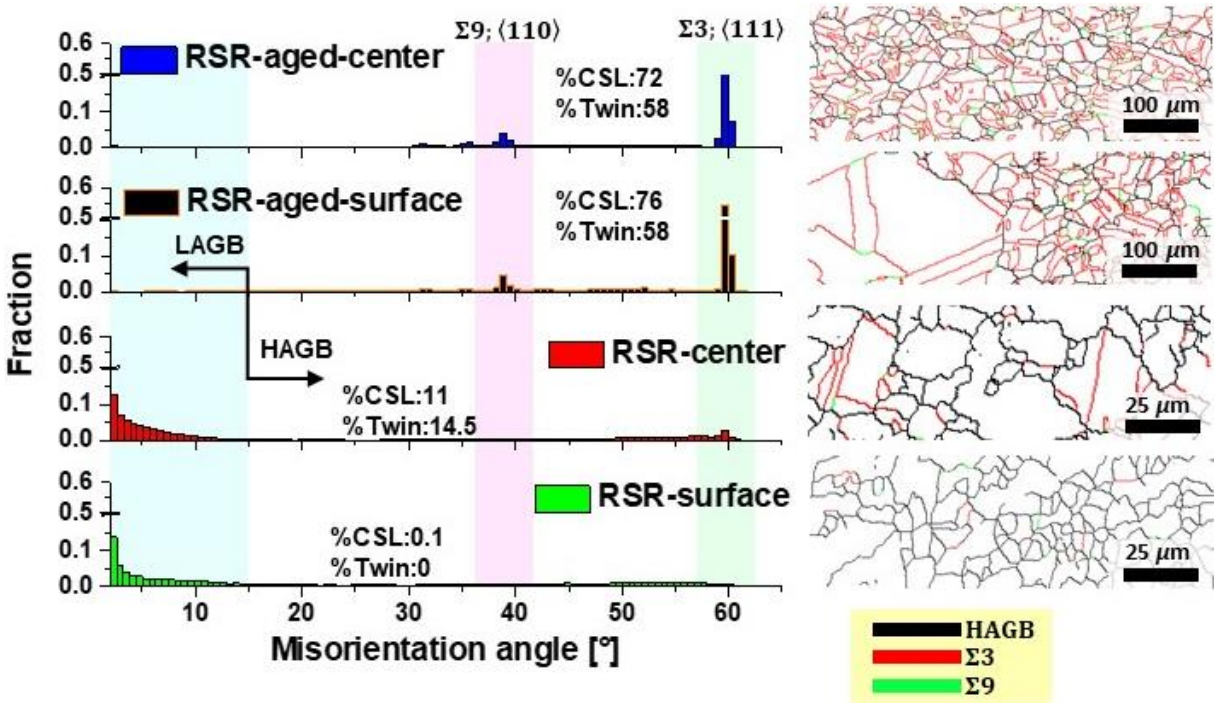

Fig. 12 Misorientation angle distributions and CSL maps for the different zones across the rod radius

The presence of Σ3 coherent twins in low stacking fault energy (SFE) face-centered cubic (FCC) structures such as copper has been related to the combination of deformation processes followed by heat treatment. In this study, the multiple RSR passes of deformation until obtaining the desired diameter combined with the heat treatment at high temperature promote the grain boundaries character change. In this way, it can be established that the effect of temperature after RSR processing changes the boundaries that initially contain high energy to a coherent twin form. The large number of Σ3 grain boundaries observed in the RSR + aged material may favor mechanical properties such as fatigue strength by reducing the rate of crack propagation since these boundaries are less prone to intergranular fracture [48].

4.2 Material heterogeneity

The RSR processing generates a heterogeneous state of deformation between the surface and the center of the bar. This deformation state gives rise to more prominent grain refinement close to the rod surface while the areas away from the surface present a larger grain size (see Fig. 4a and Fig. 4b). This heterogeneity prior to the aging treatment results, in the more deformed areas (that is, a larger number of subgrains, high density of GNDs, and high energy) after aging in a more accelerated recrystallization phenomenon than in the center of the bars. According to Muñoz et al. [49,50], bars of metallic materials processed by high magnitudes of plastic deformation can generate microstructural gradients when applying high temperatures. This

behavior is attributed to the fact that the temperature necessary for recrystallization is lower in the deformed areas than in the less deformed ones. In this direction, since the areas near the surface are more deformed than the center of the bar and the quenching temperature of the aging treatment is much higher than the copper recrystallization temperature (i.e., 960 °C for the quenching followed by the 495 °C for the aging, both higher than 200 °C, copper recrystallization temperature), it is easier to go from recrystallization to abnormal grain growth on the surface than in the center of the rod.

The grain fragmentation, recrystallization, multiplication, and annihilation of dislocations in the alloy are corroborated by the representation of kernel average misorientation (KAM) in Fig. 13a. This figure shows that through the KAM distributions and maps, the microstructure after RSR registers higher KAM values inside the grains than in the RSR + aged material. This behavior is due to the more significant presence of mobile dislocations inside the grains generated by the RSR process's deformation. These dislocations generate curvature in the grains that translate into orientation differences inside the grains, indicating potential places for further grain size reduction. On the other hand, after the solubilization and aging treatment, the annihilation of dislocations and subsequent grain growth takes place in the material microstructure. Thus, a continuous curvature in the material's microstructure with lower and less scattered KAM values is observed for the RSR+aged material.

In this order of ideas, Fig. 13b indicates the average grain size evolution for both RSR and RSR + aged, in the bars' radial direction. This figure confirms the formation of microstructural gradients in both processes. The grain size profiles for the RSR process demonstrate a more significant grain size refinement in the vicinity of the bar surface, which begins to change towards the center of the bar with grain growth that approximately doubles the size of the surface. On the other hand, after the aging treatment, the material experiences a substantial change in the grain size growth, especially in the surface's neighborhood, becoming 20 times greater than the material before aging. Thus, moving away from the aged material's surface, the formation of an interface can be observed where the transition from large grain sizes (~ 200 µm) to smaller sizes (~ 40 µm) occurs. Hence, grain size profiles demonstrate the formation of a recrystallization gradient, which is more intense at the surface than at the center of the rod.

As a consequence of the aging treatment, the recrystallization phenomenon gives rise to larger grain size in the RSR + aged material than in the RSR condition. However, Fig. 13c indicates that, although the grain size in the RSR + aged material is much larger than the RSR, the former's yield strength is greater than that of the latter. This apparent contradiction is supported by the precipitation hardening mechanism. According to various authors and studies using TEM [51,52], the processing of Cu alloys with plastic deformation and subsequent aging heat treatment gives rise to the formation of nanoprecipitates. The authors showed that nanoprecipitates act as elements that pinned the dislocations while dividing them, creating more defects. Therefore, under the influence of stress, nanoprecipitates act as elements that nucleate new dislocations, and that can help to improve ductility. Thus, it can be established and confirmed that the main hardening mechanisms come from dislocations and precipitates.

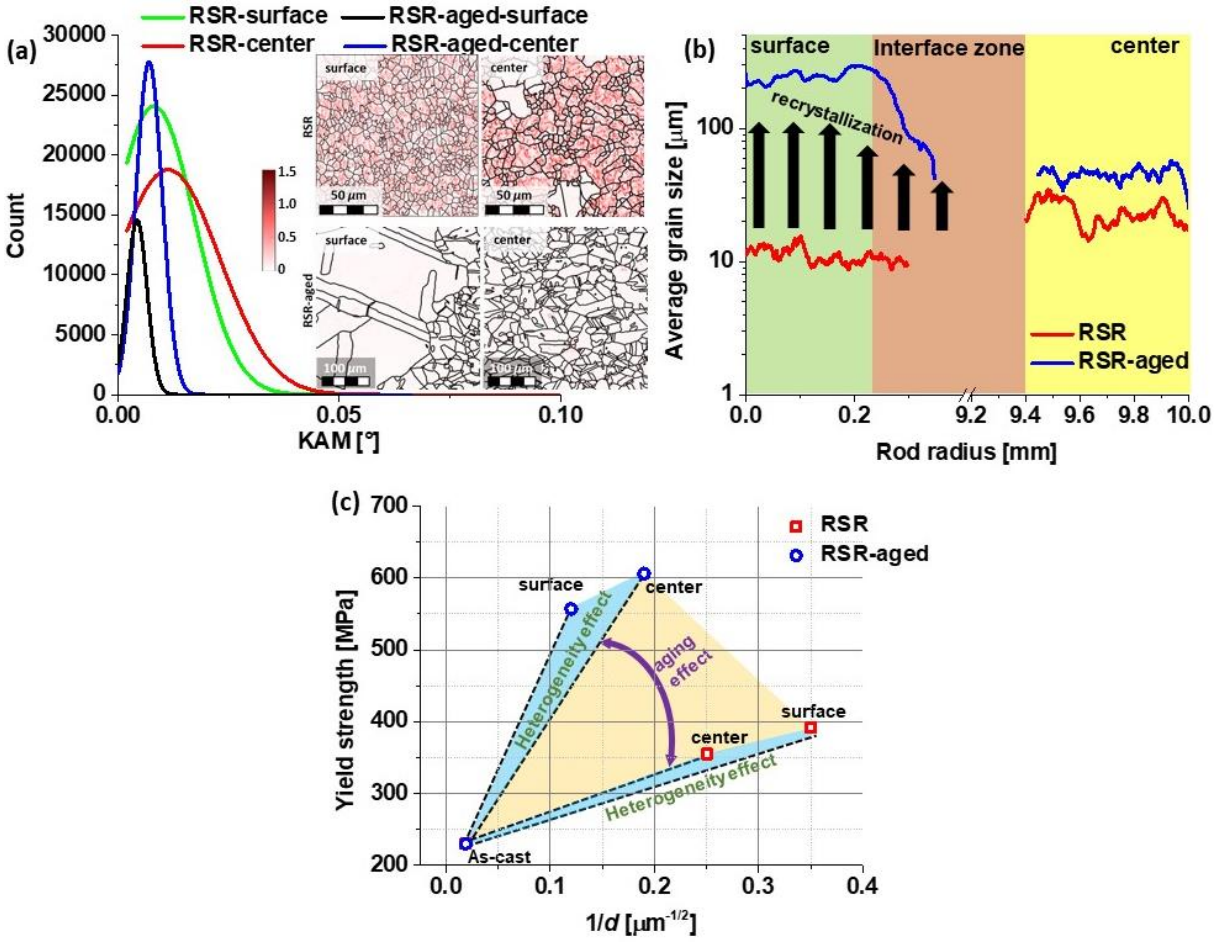

Fig. 13 Microstructure heterogeneity, KAM maps and distributions across the rod radius (a), average grain size profiles after RSR and RSR+aged treatment (b), and yield strength and grain size changes after RSR and RSR+aged treatment (c).

4.3 Electroconductivity and hybrid properties

The conductivity measurements are presented in MS/m (megasiemens/meter) and %IACS, that is, as a percentage of pure copper's conductivity (58 MS/m). Fig. 14 shows a diagram of the electrical conductivity values after RSR and aging treatment. At first glance, the heat treatment has a significant effect on electrical conductivity. However, after RSR, the electrical conductivity is 30.52% IACS. Quenching and subsequent aging of the samples lead to an increase in the electrical conductivity value by 48% (Fig. 14). Therefore, the electrical conductivity increment of the aged material is associated with the purification phenomenon of the Cu matrix with precipitates, as demonstrated by the EDS maps and by Yang et al. [51] in a Cu alloy deformed by rolling and subsequent aging treatment.

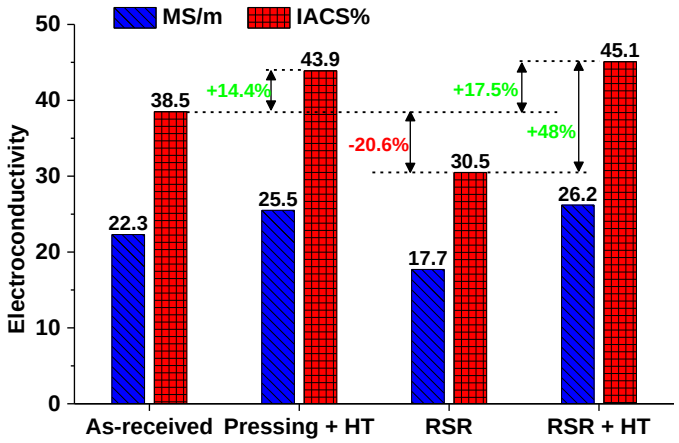

Fig. 14 Electrical conductivity of Cu-Ni-Cr-Si alloy after RSR and heat treatment

The technical standard for Cu-Ni-Cr-Si alloy semi-finished products shows a conductivity value of at least 24 MS/m. Therefore, the two analyzed conditions comply with this requirement. It is also worth noting that these values are obtained based on the conditions used in an industrial environment to obtain semi-finished products by extrusion and drawing.

Table 5 compares the Cu-Ni-Cr-Si alloy properties obtained by an industrial method of hot extrusion (e.g., drawing) and the properties of rods subjected to RSR. The main requirements for heat-resistant low alloy products for electrical purposes are hardness and electrical conductivity. In addition, thermal conductivity and strength properties can be taken into account. Therefore, the main task when choosing technological modes of deformation and hardening heat treatment is to find the best compromise between hardness and electrical conductivity. So, rods obtained by the RSR method meet the electrical conductivity requirements of technical standards and the hardness.

The RSR + aged material's improvement electrical conductivity concerning the RSR is associated with factors such as the decrease in the density of dislocations, Cu matrix purification, and the change in the grain boundaries character because of the heat treatment after RSR processing. The effect of temperature leads to dislocation annihilation and grain growth reflected in a lower density of grain boundaries. According to Wu et al. [37], electrical resistivity is a function of different contributions such as dislocations, solid solution, precipitates, and grain boundaries. Therefore, it is clear that the RSR material's resistivity is higher due to the greater number of dislocations and grain boundaries.

Table 5. Comparative properties indicators of the rods made of Cu-Ni-Cr-Si alloy

Parameter name	Method of hot deformation	
	Extrusion or drawing [39]	Radial-shear rolling
Hardness (HV)	210	260-280
Ultimate tensile strength (MPa)	750	650-750
Yield strength (MPa)	700	557-606
Elongation (%)	10	12-17
Electrical conductivity (MS/m)	24	26.2

For a better appreciation of the effect of the RSR and RSR + aged processes on the alloy properties, Fig. 15a shows the relationship between mechanical strength and conductivity for various copper alloys. As a first observation, depending on the alloying elements, different behaviors are highlighted. For example, the alloys of Cu-Ni-Si-Al [53,54] and Cu-Ni-Co-Si-Mg [55] reach strengths larger than 900 MPa due to the formation of Ni and Si clusters with sizes of 2 nm. However, the conductivity was lower than 30% IACS and the homogeneous elongation less than 5%. Comparing the current RSR + aged alloy with alloys of the same type Cu-Ni-Si-Cr [35,37,56] it was found that these latter alloys achieved high strengths (> 700 MPa) with conductivity values lower than 27% IACS and above 45% IACS when the material is pre-formed by rolling. These observations suggest that the use of the RSR process and the combination with the aging treatment gives rise to a wider range of properties than the simple use of heat treatments. On the other hand, the alloys of Cu-Ni-Si [57–59], and with additions of Vanadium [60] deformed by rolling and later aging, allow to achieve high electrical conductivities (> 50% IACS) at the cost of their mechanical strength reduction. Therefore, Fig. 15a confirms that the methodology proposed in this study allows obtaining remarkable properties in terms of conductivity that are similar to alloys like Cu-Ni-Si-Ti [61–64], Cu-Ni-Si-Co-Cr [65], and Cu-Ni-Si-P [66]. Additionally, Fig. 15b proves that the heterogeneous

microstructure produces an alloy with a strong combination of strength and ductility. Finally, it can be concluded that the RSR process, together with the appropriate aging heat treatment, allows obtaining a structural heterogeneous copper alloy that stands out among different copper alloys by combining strength, conductivity, and ductility.

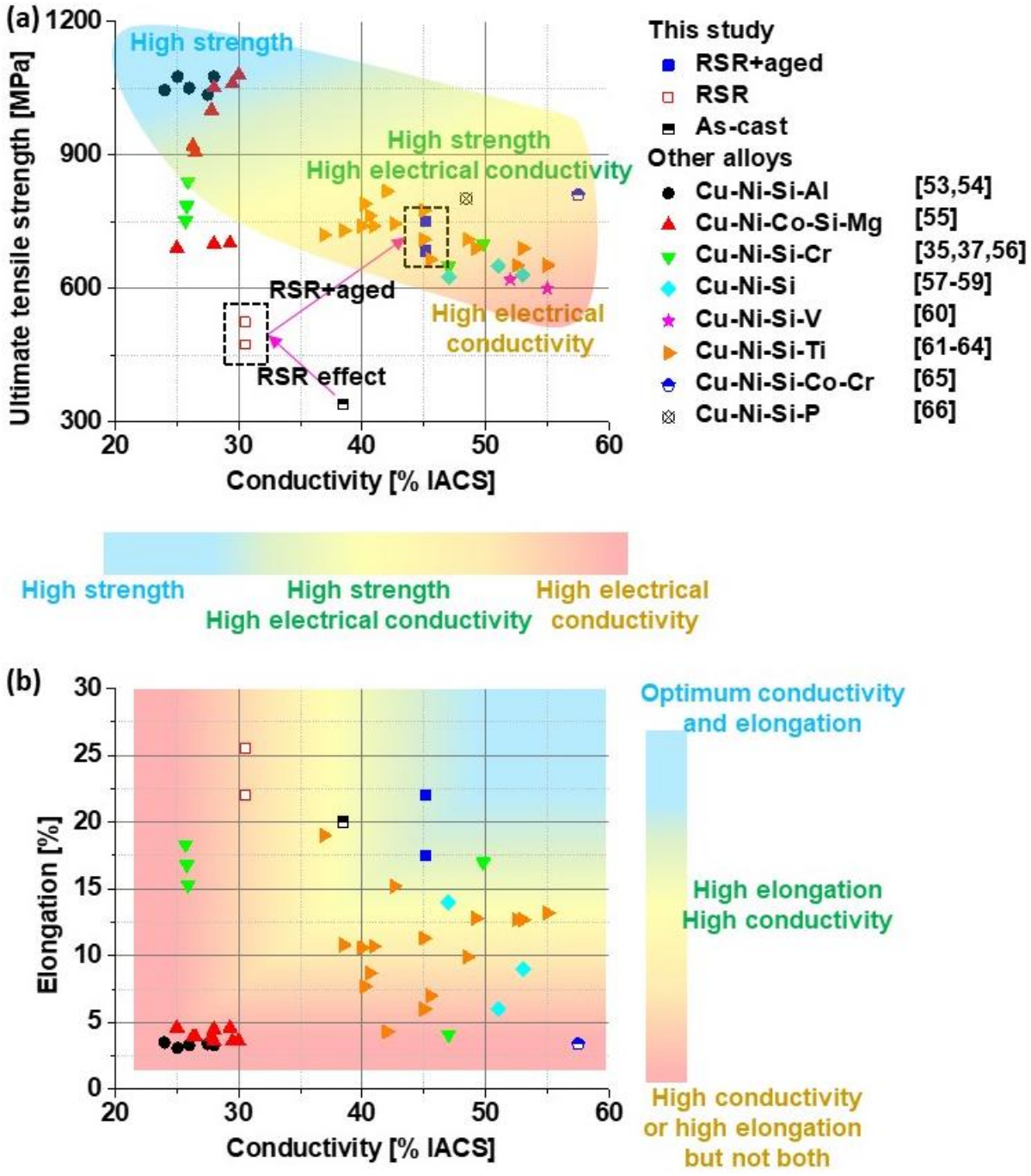

Fig. 15 Comparison of the Cu-Ni-Cr-Si alloy properties with different Cu alloys: Cu-Ni-Si-Al [53,54], Cu-Ni-Co-Si-Mg [55], Cu-Ni-Si-Cr [35,37,56], Cu-Ni-Si [57–59], Cu-Ni-Si-V [60], Cu-Ni-Si-Ti [61–64], Cu-Ni-Si-Co-Cr [65], Cu-Ni-Si-P [66]. Ultimate tensile strength and conductivity (a), and elongation vs conductivity (b).

5 Conclusions

The article describes a method for producing semi-finished products from a Cu-Ni-Cr-Si alloy by the radial-shear rolling process.

1. In the radial-shear rolling process, the alloy hardening occurs due to intense shear deformations in the surface layers of the rod, giving rise to microstructure heterogeneity. Subsequent aging treatment leads to precipitation hardening due to the release of Ni_2Cr and Cr_3Si hardener phases dispersed in the matrix as particles uniformly distributed in the bulk of the samples in the form of small inclusions with an average size of 0.56-0.65 μm.

2. The RSR process generates deformation gradients that, after the aging heat treatment, are transformed into recrystallization gradients in the bars' radial direction that give rise to a structural material with a remarkable combination of strength ductility and electrical conductivity. Therefore, the abnormal grain growth results from the deformation gradient across the rod diameter after RSR processing. Thus, the strain heterogeneity between the rod surface and its center zone gives rise to recrystallization gradients after the heat treatment.

3. After RSR, the main strength contribution comes from dislocations. The second contribution is associated with the grain size due to the greater grain refinement. After the aging treatment, the main strength contributions come from the precipitates and dislocation components in both the surface and center areas. This behavior demonstrates the greater strength of the heat-treated material concerning the RSR due to the additional contribution of the precipitates.

4. After RSR and heat treatment, the alloy increased the strength by 50% with elongations ranging between 17-22% and obtaining an electrical conductivity of 45.17% IACS concerning the 30.52% IACS of the RSR material. Thus, the RSR process, together with the appropriate aging heat treatment, allows obtaining a structural heterogeneous copper alloy that stands out among different copper alloys by combining strength, conductivity, and ductility.

5. Hardness and yield strength values infer that the RSR method is a good and versatile alternative for producing bars with diameters in the range of 10-55 mm. The radial-shear rolling method at the large industrial production scale for bars will reduce the tool's cost, the occupied floor space, and equipment downtime associated with the readjustment and replacement of the tool.

Data availability statement: The raw/processed data required to reproduce these findings cannot be shared at this time as the data also forms part of an ongoing study.

Credit authorship contribution statement

Yu.V. Gamin: Investigation, formal analysis, writing original draft, writing review and editing. **Jairo Alberto Muñoz:** Investigation, formal analysis, writing review and editing. **A.S. Aleschenko:** Data curation, formal analysis and investigation. **A.A. Komissarov:** Supervision, funding acquisition, investigation. **N.S. Bunits:** Investigation, writing review and editing. **D.A. Nikolaev:** Investigation. **A.V. Fomin:** Data curation. **V.V. Cheverikin:** Investigation, data curation.

Conflict of interest: The authors declare no conflict of interest.

Acknowledges

The authors are grateful to the metallurgical company LLC «Astrinsplav SK» for the materials provided for this research. JAMB acknowledge the financial support of the Ministry of Science and Higher Education of the Russian Federation in the framework of Increase Competitiveness Program of NUST «MISiS» (№ К4-2019-045), implemented by a governmental decree dated 16th of March 2013, N 211.

References

[1] J.R. Davis, others, Copper and copper alloys, ASM international, 2001.
[2] A. V Zinov'ev, A.N. Koshmin, A.Y. Chasnikov, Effect of Continuous Extrusion Parameters on Alloy M1 Round Section Bar Microstructure and Mechanical Property Formation, Metallurgist. 63 (2019) 422–428. https://doi.org/10.1007/s11015-019-00838-3.
[3] Y. Sun, D. He, F. Xue, R. Lai, G. He, Microstructure and Mechanical Characterization of a Dissimilar Friction-Stir-Welded CuCrZr/CuNiCrSi Butt Joint, Metals (Basel). 8 (2018). https://doi.org/10.3390/met8050325.
[4] Q. Liu, X. Zhang, Y. Ge, J. Wang, J.-Z. Cui, Effect of processing and heat treatment on behavior of Cu-Cr-Zr alloys to railway contact wire, Metall. Mater. Trans. A. 37 (2006) 3233–3238. https://doi.org/10.1007/BF02586158.
[5] Y. V Gamin, B.A. Romantsev, A.N. Pashkov, P. V Patrin, I.A. Bystrov, A. V Fomin, M. V Kadach, Obtaining Hollow Semifinished Products Based on Copper Alloys for Electrical Purposes by Means of Screw Rolling, Russ. J. Non-Ferrous Met. 61 (2020) 162–171. https://doi.org/10.3103/S1067821220020054.
[6] Q. Lei, Z. Xiao, W. Hu, B. Derby, Z. Li, Phase transformation behaviors and properties of a high strength Cu-Ni-Si alloy, Mater. Sci. Eng. A. 697 (2017) 37–47. https://doi.org/https://doi.org/10.1016/j.msea.2017.05.001.
[7] H. Kim, J.H. Ahn, S.Z. Han, J. Jo, H. Baik, M. Kim, H.N. Han, Microstructural characterization of cold-drawn Cu–Ni–Si alloy having high strength and high conductivity, J. Alloys Compd. 832 (2020) 155059. https://doi.org/https://doi.org/10.1016/j.jallcom.2020.155059.
[8] V. Segal, Review: Modes and Processes of Severe Plastic Deformation (SPD)., Mater.

(Basel, Switzerland). 11 (2018). https://doi.org/10.3390/ma11071175.
[9] R.G. Chembarisova, E.A. Sarkeeva, I. V Alexandrov, W. Wei, Analysis of the effect of equal-channel angular pressing on the strength and electrical conductivity of low-alloyed alloys of the Cu-Cr-Zr system, J. Phys. Conf. Ser. 1431 (2020) 12065. https://doi.org/10.1088/1742-6596/1431/1/012065.
[10] E.N. Borodin, A. Morozova, V. Bratov, A. Belyakov, A.P. Jivkov, Experimental and numerical analyses of microstructure evolution of Cu-Cr-Zr alloys during severe plastic deformation, Mater. Charact. 156 (2019) 109849. https://doi.org/https://doi.org/10.1016/j.matchar.2019.109849.
[11] Y. Miyajima, M. Uchiyama, H. Adachi, T. Fujii, S. Onaka, M. Kato, Effect of Roll-Bonding and Subsequent Annealing on Microstructure Evolution of Accumulative Roll Bonded Pure Copper, Mater. Trans. 57 (2016) 1411–1417.
[12] W. Wang, H. Kang, Z. Chen, Z. Chen, C. Zou, R. Li, G. Yin, T. Wang, Effects of Cr and Zr additions on microstructure and properties of Cu-Ni-Si alloys, Mater. Sci. Eng. A. 673 (2016) 378–390. https://doi.org/https://doi.org/10.1016/j.msea.2016.07.021.
[13] A.B. Naizabekov, S.N. Lezhnev, E. Panin, Formation of a Gradient Structure in Austenitic Stainless Steel AISI 321 by Radial-Shear Rolling, in: Mater. Eng. Technol. Prod. Process. VI, Trans Tech Publications Ltd, 2021: pp. 246–251. https://doi.org/10.4028/www.scientific.net/SSP.316.246.
[14] X. Ding, L. Sun, X. Huang, Z. Zhao, Research on Three-Roll Screw Rolling Process for Ti6Al4V Titanium Alloy Bar, High Temp. Mater. Process. 38 (2019) 178–182.
[15] I.S. Valeev, A.K. Valeeva, R.F. Fazlyakhmetov, G.R. Khalikova, Effect of radial-shear rolling on structure of aluminum alloy D16 (Al-4.4Cu-1.6Mg), Inorg. Mater. Appl. Res. 6 (2015) 45–48. https://doi.org/10.1134/S2075113315010153.
[16] Y. Gamin, T. Akopyan, A. Koshmin, A. Dolbachev, A. Aleshchenko, S.P. Galkin, B.A. Romantsev, Investigation of the microstructure evolution and properties of A1050 aluminum alloy during radial-shear rolling using FEM analysis, Int. J. Adv. Manuf. Technol. 108 (2020) 695–704. https://doi.org/10.1007/s00170-020-05227-8.
[17] S. Shukla, D. Choudhuri, T. Wang, K. Liu, R. Wheeler, S. Williams, B. Gwalani, R.S. Mishra, Hierarchical features infused heterogeneous grain structure for extraordinary strength-ductility synergy, Mater. Res. Lett. 6 (2018) 676–682. https://doi.org/10.1080/21663831.2018.1538023.
[18] Y. Ma, M. Yang, F. Yuan, X. Wu, A Review on Heterogeneous Nanostructures: A Strategy for Superior Mechanical Properties in Metals, Metals (Basel). 9 (2019) 598. https://doi.org/10.3390/met9050598.
[19] J. Li, C. Fang, Y. Liu, Z. Huang, S. Wang, Q. Mao, Y. Li, Deformation mechanisms of 304L stainless steel with heterogeneous lamella structure, Mater. Sci. Eng. A. 742 (2019) 409–413. https://doi.org/10.1016/j.msea.2018.11.047.
[20] J. Duan, H. Wen, C. Zhou, X. He, R. Islamgaliev, R. Valiev, Discontinuous grain growth in an equal-channel angular pressing processed Fe-9Cr steel with a heterogeneous microstructure, Mater. Charact. (2019) 110004. https://doi.org/10.1016/J.MATCHAR.2019.110004.
[21] P. Sathiyamoorthi, H.S. Kim, Progress in Materials Science High-entropy alloys with heterogeneous microstructure : Processing and mechanical properties, Prog. Mater. Sci. (2020) 100709. https://doi.org/10.1016/j.pmatsci.2020.100709.
[22] P. Cai, X. Lian, Z. Tang, L. Zhang, T. Wang, L. Chai, G. Wu, Effect of heterogeneous laser surface treatment on mechanical properties of interstitial free steel, {IOP} Conf. Ser. Mater. Sci. Eng. 580 (2019) 12029. https://doi.org/10.1088/1757-899x/580/1/012029.
[23] J.A. Muñoz, O.F.H. Cobos, R. M'Doihoma, M. Avalos, R.E. Bolmaro, Inducing

heterogeneity in an austenitic stainless steel by equal channel angular sheet extrusion (ECASE), J. Mater. Res. Technol. 8 (2019) 2473–2479. https://doi.org/10.1016/j.jmrt.2019.04.013.
[24] J.A. Muñoz, M. Avalos, R.E. Bolmaro, Heterogeneity of strain path, texture and microstructure evolution of AA6063-T6 processed by Equal Channel Angular Sheet Extrusion (ECASE), J. Alloys Compd. 768 (2018) 349–357. https://doi.org/10.1016/j.jallcom.2018.07.216.
[25] J.A. Muñoz, A. Komissarov, M. Avalos, R.E. Bolmaro, Mechanical and microstructural behavior of a heterogeneous austenitic stainless steel processed by Equal Channel Angular Sheet Extrusion (ECASE), Mater. Sci. Eng. A. 792 (2020) 139779. https://doi.org/https://doi.org/10.1016/j.msea.2020.139779.
[26] M. Jamalian, M. Hamid, N. De Vincentis, Q. Buck, D.P. Field, H.M. Zbib, Creation of heterogeneous microstructures in copper using high-pressure torsion to enhance mechanical properties, Mater. Sci. Eng. A. 756 (2019) 142–148. https://doi.org/10.1016/j.msea.2019.04.024.
[27] A. Arbuz, A. Kawalek, K. Ozhmegov, H. Dyja, E. Panin, A. Lepsibayev, S. Sultanbekov, R. Shamenova, Using of Radial-Shear Rolling to Improve the Structure and Radiation Resistance of Zirconium-Based Alloys, Materials (Basel). 13 (2020). https://doi.org/10.3390/ma13194306.
[28] S.P. Galkin, Radial shear rolling as an optimal technology for lean production, Steel Transl. 44 (2014) 61–64. https://doi.org/10.3103/S0967091214010069.
[29] Gamin, Yury, Koshmin, Alexander, Ta, Dinh Xuan, Analysis of radial-shear rolling process parameters of aluminum alloys based on FEM modeling, MATEC Web Conf. 315 (2020) 11001. https://doi.org/10.1051/matecconf/202031511001.
[30] J. Blaber, B. Adair, A. Antoniou, Ncorr: Open-Source 2D Digital Image Correlation Matlab Software, Exp. Mech. 55 (2015) 1105–1122. https://doi.org/10.1007/s11340-015-0009-1.
[31] O.F. Higuera, J.A. Muñoz, J.M. Cabrera, Mechanical properties of different coppers processed by equal channel angular pressing, in: Mater. Sci. Forum, 2011: pp. 713–718.
[32] T.K. Akopyan, Y. V Gamin, S.P. Galkin, A.S. Prosviryakov, A.S. Aleshchenko, M.A. Noshin, A.N. Koshmin, A. V Fomin, Radial-shear rolling of high-strength aluminum alloys: Finite element simulation and analysis of microstructure and mechanical properties, Mater. Sci. Eng. A. 786 (2020) 139424. https://doi.org/https://doi.org/10.1016/j.msea.2020.139424.
[33] Y. V Gamin, T.K. Akopyan, A.N. Koshmin, A.P. Dolbachev, A. V Goncharuk, Microstructure evolution and property analysis of commercial pure Al alloy processed by radial-shear rolling, Arch. Civ. Mech. Eng. 20 (2020) 143. https://doi.org/10.1007/s43452-020-00143-w.
[34] Z. Rdzawski, J. Stobrawa, Thermomechanical processing of Cu–Ni–Si–Cr–Mg alloy, Mater. Sci. Technol. 9 (1993) 142–150. https://doi.org/10.1179/mst.1993.9.2.142.
[35] J.Y. Cheng, B.B. Tang, F.X. Yu, B. Shen, Evaluation of nanoscaled precipitates in a Cu–Ni–Si–Cr alloy during aging, J. Alloys Compd. 614 (2014) 189–195. https://doi.org/https://doi.org/10.1016/j.jallcom.2014.06.089.
[36] C. Igathinathane, L.O. Pordesimo, E.P. Columbus, W.D. Batchelor, S.R. Methuku, Shape identification and particles size distribution from basic shape parameters using ImageJ, Comput. Electron. Agric. 63 (2008) 168–182. https://doi.org/10.1016/j.compag.2008.02.007.
[37] Y. Wu, Y. Li, J. Lu, S. Tan, F. Jiang, J. Sun, Correlations between microstructures and properties of Cu-Ni-Si-Cr alloy, Mater. Sci. Eng. A. 731 (2018) 403–412.

https://doi.org/10.1016/j.msea.2018.06.075.
[38] O. V Samoilova, E.A. Trofimov, Phase equilibria in the copper-rich corner of the Cu-Ni-Si-Cr system, in: Mater. Sci. Forum, 2016: pp. 107–112.
[39] «Астринсплав СК» Металлургическое предприятие, Пруток бронзовый круглый, сплав, (n.d.). https://assk.ru/product/prutok-bronzovyj-kruglyj-splav-brnxkf-dkrnt-md-nd-5-35-mm/ (accessed June 3, 2021).
[40] O.E. Osintsev, V.N. Fedorov, Copper and Copper Alloys: Domestic and Foreign Brands, Mashinostr. Publ., Moscow. (2004).
[41] I.S. Yasnikov, A. Vinogradov, Y. Estrin, Revisiting the Considère criterion from the viewpoint of dislocation theory fundamentals, Scr. Mater. 76 (2014) 37–40. https://doi.org/10.1016/j.scriptamat.2013.12.009.
[42] Y. Chen, N. Gao, G. Sha, S.P. Ringer, M.J. Starink, Microstructural evolution, strengthening and thermal stability of an ultrafine-grained Al–Cu–Mg alloy, Acta Mater. 109 (2016) 202–212. https://doi.org/https://doi.org/10.1016/j.actamat.2016.02.050.
[43] M.A. Meyers, K.K. Chawla, Mechanical Behavior of Materials, Prentice Hall, 1999. https://books.google.ru/books?id=caJRAAAAMAAJ.
[44] H. Watanabe, T. Kunimine, C. Watanabe, R. Monzen, Y. Todaka, Tensile deformation characteristics of a Cu−Ni−Si alloy containing trace elements processed by high-pressure torsion with subsequent aging, Mater. Sci. Eng. A. 730 (2018) 10–15. https://doi.org/https://doi.org/10.1016/j.msea.2018.05.090.
[45] U.F. Kocks, H. Mecking, Physics and phenomenology of strain hardening: The FCC case, Prog. Mater. Sci. 48 (2003) 171–273. https://doi.org/10.1016/S0079-6425(02)00003-8.
[46] J.A. Muñoz, T. Khelfa, A. Komissarov, J.-M. Cabrera, Ductility and plasticity of ferritic-pearlitic steel after severe plastic deformation, Mater. Sci. Eng. A. 805 (2020) 140624. https://doi.org/https://doi.org/10.1016/j.msea.2020.140624.
[47] W.Q. Cao, C.F. Gu, E. V Pereloma, C.H.J. Davies, Stored energy, vacancies and thermal stability of ultra-fine grained copper, Mater. Sci. Eng. A. 492 (2008) 74–79. https://doi.org/https://doi.org/10.1016/j.msea.2008.02.048.
[48] S. Kobayashi, M. Hirata, S. Tsurekawa, T. Watanabe, Grain boundary engineering for control of fatigue crack propagation in austenitic stainless steel, Procedia Eng. 10 (2011) 112–117. https://doi.org/https://doi.org/10.1016/j.proeng.2011.04.021.
[49] J.A. Muñoz, A. Komissarov, I. Mejía, H. Hernández-Belmontes, J.-M. Cabrera, Characterization of the Gas Tungsten Arc Welding (GTAW) joint of Armco iron nanostructured by Equal-Channel Angular Pressing (ECAP), J. Mater. Process. Technol. 288 (2021) 116902. https://doi.org/https://doi.org/10.1016/j.jmatprotec.2020.116902.
[50] J.A. Muñoz, O.F. Higuera, A.H. Expósito, A. Boulaajaj, R.E. Bolmaro, F.D. Dumitru, P.R. Calvillo, A.M. Jorge, J.M. Cabrera, Thermal stability of ARMCO iron processed by ECAP, Int. J. Adv. Manuf. Technol. 98 (2018) 2917–2932. https://doi.org/10.1007/s00170-018-2353-7.
[51] H. Yang, K. Li, Y. Bu, J. Wu, Y. Fang, L. Meng, J. Liu, H. Wang, Nanoprecipitates induced dislocation pinning and multiplication strategy for designing high strength, plasticity and conductivity Cu alloys, Scr. Mater. 195 (2021) 113741. https://doi.org/https://doi.org/10.1016/j.scriptamat.2021.113741.
[52] B.G. Clark, I.M. Robertson, L.M. Dougherty, D.C. Ahn, P. Sofronis, High-temperature Dislocation-precipitate Interactions in Al Alloys: An in situ Transmission Electron Microscopy Deformation Study, J. Mater. Res. 20 (2005) 1792–1801. https://doi.org/10.1557/JMR.2005.0224.

[53] Q. Lei, S. Li, J. Zhu, Z. Xiao, F. Zhang, Z. Li, Microstructural evolution, phase transition, and physics properties of a high strength Cu–Ni–Si–Al alloy, Mater. Charact. 147 (2019) 315–323. https://doi.org/https://doi.org/10.1016/j.matchar.2018.11.018.
[54] Q. Lei, Z. Li, C. Dai, J. Wang, X. Chen, J.M. Xie, W.W. Yang, D.L. Chen, Effect of aluminum on microstructure and property of Cu–Ni–Si alloys, Mater. Sci. Eng. A. 572 (2013) 65–74. https://doi.org/https://doi.org/10.1016/j.msea.2013.02.024.
[55] J. Huang, Z. Xiao, J. Dai, Z. Li, H. Jiang, W. Wang, X. Zhang, Microstructure and Properties of a Novel Cu–Ni–Co–Si–Mg Alloy with Super-high Strength and Conductivity, Mater. Sci. Eng. A. 744 (2019) 754–763. https://doi.org/https://doi.org/10.1016/j.msea.2018.12.075.
[56] Y. Wu, Y. Li, J. Lu, S. Tan, F. Jiang, J. Sun, Effects of pre-deformation on precipitation behaviors and properties in Cu-Ni-Si-Cr alloy, Mater. Sci. Eng. A. 742 (2019) 501–507. https://doi.org/https://doi.org/10.1016/j.msea.2018.11.045.
[57] P. Stavroulakis, A. Toulfatzis, A. Vazdirvanidis, G. Pantazopoulos, S. Papaefthymiou, Investigation of the Aging Behavior of a Cu–Ni–Si Rolled Alloy, Metallogr. Microstruct. Anal. 8 (2019) 167–181. https://doi.org/10.1007/s13632-019-00531-6.
[58] S.Z. Han, J. Lee, S.H. Lim, J.H. Ahn, K. Kim, S. Kim, Optimization of conductivity and strength in Cu-Ni-Si alloys by suppressing discontinuous precipitation, Met. Mater. Int. 22 (2016) 1049–1054. https://doi.org/10.1007/s12540-016-6156-9.
[59] D.M. Zhao, Q.M. Dong, P. Liu, B.X. Kang, J.L. Huang, Z.H. Jin, Structure and strength of the age hardened Cu–Ni–Si alloy, Mater. Chem. Phys. 79 (2003) 81–86. https://doi.org/https://doi.org/10.1016/S0254-0584(02)00451-0.
[60] S.Z. Han, J.H. Gu, J.H. Lee, Z.P. Que, J.H. Shin, S.H. Lim, S.S. Kim, Effect of V addition on hardness and electrical conductivity in Cu-Ni-Si alloys, Met. Mater. Int. 19 (2013) 637–641. https://doi.org/10.1007/s12540-013-4002-x.
[61] H.G. Kim, T.W. Lee, S.M. Kim, S.Z. Han, K. Euh, W.Y. Kim, S.H. Lim, Effects of Ti addition and heat treatments on mechanical and electrical properties of Cu-Ni-Si alloys, Met. Mater. Int. 19 (2013) 61–65. https://doi.org/10.1007/s12540-013-1011-8.
[62] E. Lee, S. Han, K. Euh, S. Lim, S. Kim, Effect of Ti addition on tensile properties of Cu-Ni-Si alloys, Met. Mater. Int. 17 (2011) 569. https://doi.org/10.1007/s12540-011-0807-7.
[63] E. Lee, K. Euh, S.Z. Han, S. Lim, J. Lee, S. Kim, Tensile and electrical properties of direct aged Cu-Ni-Si-x%Ti alloys, Met. Mater. Int. 19 (2013) 183–188. https://doi.org/10.1007/s12540-013-2007-0.
[64] C. Watanabe, S. Takeshita, R. Monzen, Effects of Small Addition of Ti on Strength and Microstructure of a Cu-Ni-Si Alloy, Metall. Mater. Trans. A. 46 (2015) 2469–2475. https://doi.org/10.1007/s11661-015-2870-z.
[65] Z. Zhao, Z. Xiao, Z. Li, W. Qiu, H. Jiang, Q. Lei, Z. Liu, Y. Jiang, S. Zhang, Microstructure and properties of a Cu–Ni–Si–Co–Cr alloy with high strength and high conductivity, Mater. Sci. Eng. A. 759 (2019) 396–403. https://doi.org/https://doi.org/10.1016/j.msea.2019.05.003.
[66] Y. Zhang, B. Tian, A.A. Volinsky, H. Sun, Z. Chai, P. Liu, X. Chen, Y. Liu, Microstructure and Precipitate's Characterization of the Cu-Ni-Si-P Alloy, J. Mater. Eng. Perform. 25 (2016) 1336–1341. https://doi.org/10.1007/s11665-016-1987-6.

Figure captions

Fig. 1 Heat treatment diagram for Cu-Ni-Cr-Si alloy.
Fig. 2 Microstructure and hardness measurement scheme (a), and electroconductivity measurement scheme (b).
Fig. 3 Initial microstructure after casting process (a), grain size in the casting condition (b), tensile properties (c), EBSD map (d), and misorientation profiles for the lines indicated in the EBSD map (e).
Fig. 4 Surface grain diameter map after RSR (a), center grain diameter map after RSR (b), grain size evolution after RSR (c), surface grain diameter map after RSR+aging (d), center grain diameter map after RSR+aging (e), grain size evolution after RSR+aging (f).
Fig. 5 SEM map after aging treatment (a), EDS map (b), EDS spectrums for the red squares indicated in figure (a) (c), and Cu, Si, Ni, and Cr EDS maps (d)
Fig. 6 Precipitation particles sizes.
Fig. 7 Diffraction pattern for the Cu-Ni-Cr-Si alloy after RSR + Aging treatment
Fig. 8 Hardness evolution in the cross section after RSR and RSR + aging treatment.
Fig. 9 Mechanical properties at different zones of the samples after RSR and RSR + aging, (a) tensile curves, and (b) Considère criterion evolution.
Fig. 10 Strain evolution at the plastic instability points indicated in Fig. 8b, (a) RSR, and (b) RSR+aging.
Fig. 11 Strength contributions for the (a) RSR, (b) RSR+aged conditions, and (c) Kock's model fitting.
Fig. 12 Misorientation angle distributions and CSL maps for the different zones across the rod radius
Fig. 13 Microstructure heterogeneity, KAM maps and distributions across the rod radius (a), average grain size profiles after RSR and RSR+aged treatment (b), and yield strength and grain size changes after RSR and RSR+aged treatment (c).
Fig. 14 Electrical conductivity of Cu-Ni-Cr-Si alloy after RSR and heat treatment
Fig. 15 Comparison of the Cu-Ni-Cr-Si alloy properties with different Cu alloys: Cu-Ni-Si-Al [53,54], Cu-Ni-Co-Si-Mg [55], Cu-Ni-Si-Cr [35,37,56], Cu-Ni-Si [57–59], Cu-Ni-Si-V [60], Cu-Ni-Si-Ti [61–64], Cu-Ni-Si-Co-Cr [65], Cu-Ni-Si-P [66]. Ultimate tensile strength and conductivity (a), and elongation vs conductivity (b).

Table captions

Table 1. Chemical composition of Cu alloy (% wt.)
Table 2. Experimental properties of Cu-Ni-Cr-Si alloy in the initial state
Table 3. Deformation conditions of Rolling.
Table 4. Microstructural properties
Table 5. Comparative properties indicators of the rods made of Cu-Ni-Cr-Si alloy

Influence of the Radial-Shear Rolling (RSR) process on the microstructure, electrical conductivity and mechanical properties of a Cu-Ni-Cr-Si alloy

Yu.V. Gamin[1, *], Jairo Alberto Muñoz Bolaños[1, 2, *], A.S. Aleschenko[1], A.A. Komissarov[1], N.S. Bunits[1], D.A. Nikolaev[1], A.V. Fomin[1], V.V. Cheverikin[1]

[1]National University of Science and Technology «MISIS», 4 Leninsky pr., Moscow 119049, Russia.
[2]Instituto de Física Rosario, Consejo Nacional de Investigaciones Científicas y Técnicas-CONICET, Universidad Nacional de Rosario, Ocampo y Esmeralda, 2000 Rosario, Argentina

*Corresponding author email: gamin910@gmail.com.

Abstract

The article describes a method for producing semi-finished products from a copper alloy of the Cu-Ni-Cr-Si system for electrical purposes through the radial-shear rolling (RSR). From the Cu-Ni-Cr-Si alloy by hot deformation, rods with a diameter of 20 mm were obtained, which were then heat treated with quenching and aging. A detailed analysis of the microstructure and properties (mechanical and electrical) of the obtained samples was carried out after RSR and after heat treatment (HT). After RSR, material hardening occurs due to shear deformations forming a gradient structure with grain sizes varying from 8.22 μm to 15.95 μm between the surface and the center of the rod. The microstructure and mechanical property analysis showed that after heat treatment, the alloy is thermally hardened due to the precipitation of Ni_2Si and Cr_3Si particles uniformly distributed in the sample volume in the form of fine inclusions with an average size of 0.56-0.65 μm. After heat treatment, the alloy enhanced its mechanical properties (ultimate tensile strength (UTS) ~ 700-750 MPa, yield strength (YS) ~ 557-606 MPa, and elongation between 17 and 22%) and its electrical conductivity of 45.17% IACS from the 30.52% IACS of the RSR material. The improved mechanical properties of the heat-treated material are due to the different strength contributions mainly coming from dislocations and precipitates. The electrical conductivity improvement after the heat treatment is related to the dislocation density reduction and the increase in grain boundary misorientation due to the recrystallization phenomenon giving rise to a lower number of boundaries but with a twinning character. Thus, the RSR method offers a new industrial alternative for the production of semi-finished products from a Cu-Ni-Cr-Si alloy in the form of rods with diameters ranging from 10-55 mm.

Keywords: *copper alloys; radial-shear rolling; plastic deformation; electroconductivity.*

1 Introduction

Copper-based alloys are one of the most sought-after materials in industry [1]. Due to the good combination of high hardness, thermal and electrical conductivity, such alloys are widely used in electric welding production as contactors, connectors, and other products [2,3]. E.g., rail contact tires made of copper alloys should have high mechanical strength combined with high electrical conductivity [4]. Cu-Cr systems are promising materials for this purpose [5]. Adding small amounts of Zr to a Cu-Cr leads to an increase in strength and ductility properties at elevated temperatures (400-650 °C).

An analogue of the Cu-Cr-Zr alloy for use in electrical engineering is the alloy of the Cu-Ni-Cr-Si system. This alloy possess lower electrical conductivity, but it has improved strength properties, like high wear resistance and temperature stability [6]. For that reason, it has found application in the manufacture of electrodes, tips and parts of resistance welding machines, instrument connectors, and the electrical equipment of transport networks [7].

One way to increase the mechanical properties of materials is to reduce their structure to an ultrafine-grained scale using severe plastic deformation (SPD) [8]. Several investigations describe methods for improving the properties of Cu alloys after SPD by equal channel angular pressing (ECAP) and heat treatment [9,10]. Other methods like screw extrusion and accumulative rolling are also used for producing materials with ultra-fine grain (UFG) structure [11]. For the Cu-Ni-Si-Cr alloy system, some recent investigations are mainly aimed at the evolution of properties during heat treatment in various modes [12].

However, at the moment, the leading industrial methods for producing semi-finished products from copper alloys for electrical purposes are extrusion and drawing [1]. From the manufacturability point of view, the extrusion method has significant disadvantages. These include the inability to quickly reconfigure to a different size and the need for a large number of extrusion tools. To obtain semi-finished products from copper alloys with a high level of operational properties, the application of the radial-shear rolling (RSR) method may be relevant. This method of metal forming has found a full application for producing long round bars of various steel grades [13], titanium alloys [14], and aluminum alloys [15]. Due to the action of shear strains, a spiral-shaped gradient structure is formed with an ultrafine-grained surface layer, which provides an increase in strength properties while maintaining satisfactory ductility [16].

Today, heterogeneous structures have aroused great interest due to their excellent combination of strength and ductility [17,18]. Several methodologies have been proposed to obtain heterogeneous microstructures with different microstructural configurations (for example, heterogeneous distribution of grain sizes, localized distribution of phases in the piece's geometry, heterogeneous dislocation densities, among other characteristics) [17,19–23]. One methodology that has been used is controlled severe plastic deformation applied to sheets, bars, and discs using ECAP and high pressure torsion (HPT), respectively [24–26]. Thus, the initial deformation stages of SPD produce deformation gradients across the sample dimensions. For example, high surface shear strains are obtained after ECAP processing while maintaining its central section less deformed. Although RSR cannot be considered an SPD technique due to the change in the sample's dimensions, it does produce a similar effect between the surface and the center of the deformed material giving rise to a heterogeneous structure [27].

The developed designs of RSR mills allow obtaining long rods (up to 9 m) with different diameters on one set of working tools-rolls [28]. The weight and dimensions of such equipment are significantly lower compared to press equipment. When it is necessary to organize the production of small batches, but a large number of different sized rods, it may be relevant to replace the press equipment with RSR mills. There is no need for a large number of working tools for each bar size; the total weight of the equipment and the occupied floor space is reduced, and the wear resistance of the tool is increased. In this regard, an urgent task may be to study RSR process of copper alloys and compare it with deformation methods used in industry.

The main purpose of this work is to show the capacity of the RSR process for producing semi-finished products from Cu-Ni-Cr-Si alloy with properties quite similar or even better than traditional methods such as extrusion. The RSR process influence was studying by the evolution of microstructure and mechanical properties across the diameter of the rods and the electrical conductivity measurements under the deformed and heat-treated condition.

2 Experimental materials and methods

The initial billet (cylindrical ingot with a diameter of 110 mm) was obtained by chill casting and then deformed by hot pressing until the 60 mm rod diameter. Further, a hot-pressed rod was used for rolling. The initial billet diameter was 60 mm, and the length was 250 mm. Table 1 presents the alloy's chemical composition obtained from the EDS spectrum of several SEM images employing TESCAN VEGA SBH3 scanning electron microscope (SEM-EDS) from Oxford Instruments.

Table 1. Chemical composition of Cu alloy (% wt.)

Alloy	Cu	Ni	Cr	Si	Al	Zn	Fe	Other
Cu-Ni-Cr-Si	95.04	2.89	1.03	0.92	0.03	0.08	0.03	≤ 0.1

Table 2 summarizes the alloy's experimental electrical conductivity and mechanical properties.

Table 2. Experimental properties of Cu-Ni-Cr-Si alloy in the initial state

Parameter name	Value
Hardness (HV)	130-150
Ultimate tensile strength (MPa)	340-380
Yield strength (MPa)	220-240
Elongation (%)	20
Electrical conductivity (MS/m)	22.3

The initial billets were deformed in the hot state by radial-shear rolling. RSR was carried out at the semi-industrial rolling mill located in the laboratory of the Department of Metal forming (NUST "MISIS", Moscow). The mills are equipped with three work rolls that are deployed at a feed angle β and a toe angle δ, as indicated in previous studies [29]. Work rolls located symmetrically concerning the central rolling axis form a deformation zone rotating in one direction and deforming the workpiece. The sample moves along the deformation zone following a helicoidal path.

Before deformation, the initial billet was heated in a chamber furnace for 2 hours to a temperature of 900 °C. Rolling was carried out in 4 passes following the modes summarized in Table 3. After each pass, the bar returned to the furnace to equalize the temperature over the entire cross section. The rotary velocity of the working rolls was 30 rpm.

The elongation ratio (μ_i) for the *i* pass is defined as the ratio of the cross-sectional area of the bar in the (*i – 1*) pass (F_{i-1}) to the cross-sectional area of the bar in the *i* pass (F_i):

$$\mu_i = \frac{F_{i-1}}{F_i} = \frac{D_{i-1}^2}{D_i^2} \quad (1)$$

Where D_{i-1} and D^2 represent the initial and final rod diameter, respectively.

The total elongation ratio for several passes is defined as the ratio of the cross-sectional area of the initial billet (F_0) to the cross-sectional area of the bar after the last pass (F_n):

$$\sum_{i=1}^{n} \mu_i = \frac{F_0}{F_n} = \mu_1 \cdot \mu_2 \cdot \mu_3 \cdot \ldots \cdot \mu_n \quad (2)$$

Table 3. Deformation conditions of Rolling.

Pass Number, i	Diameter of workpiece D_{i-1}, mm	Diameter of the resulting rod D_i, mm	Elongation ratio μ_i	$\Sigma\mu_i$
1	60	46	1.70	1.70
2	46	36	1.63	2.78
3	36	28	1.65	4.60
4	28	20	1.96	9.00

After RSR, heat treatment was performed, which consisted of quenching and aging. The heat treatment cycle for the studied alloy is shown in Fig. 1.

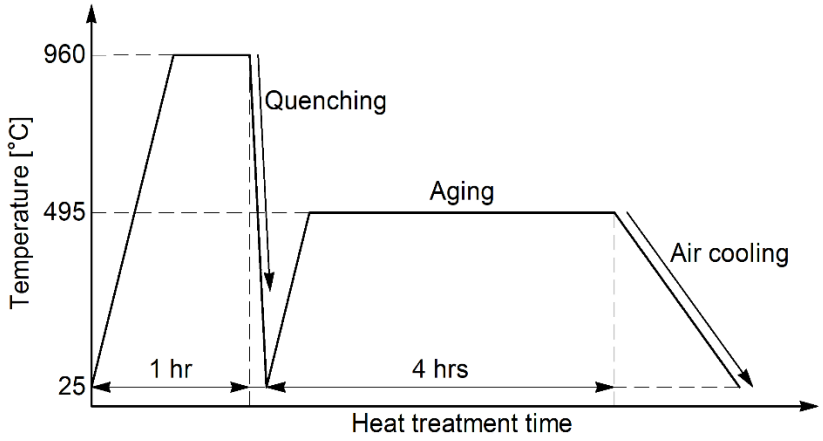

Fig. 1 Heat treatment diagram for Cu-Ni-Cr-Si alloy.

For the 20 mm diameter rods after RSR and heat treatment, electrical conductivity and microhardness distribution over the cross and longitudinal sections were measured. The microstructure was analyzed across the radial direction in three zones: i.e., the surface, the middle of the radius, and the center. Fig. 2a illustrates the microhardness measurement scheme and the microstructure analysis zones.

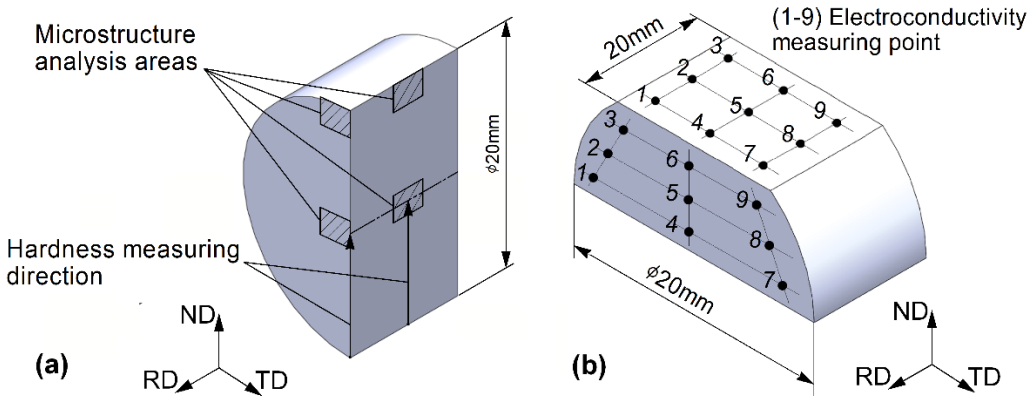

Fig. 2 Microstructure and hardness measurement scheme (a), and electroconductivity measurement scheme (b).

The microstructure was studied using a Carl Zeiss Axio Lab.A1 optical microscope. The microhardness of specimens was measured by the Vickers method (HV) on a DUROLINE MH-6 durometer (load 300 g, dwell time of 30 s). The electrical conductivity of the samples was measured at eddy current structuroscope (Scientific Research Institute of Introscopy "Srektr", Russia) at 9 points in parallel and perpendicular to the rolling direction (Fig. 2b). The final value was determined as the average value of measurements at all points.

For better understanding the microstructural characteristics of the material processed by RSR and after the aging heat treatment, a TESCAN VEGA SBH3 scanning electron microscope (SEM-EDS) from Oxford Instruments was used. The material's microstructure was analyzed at different points on the cross-sectional area of the bars using electron back-scattering diffraction (EBSD). The samples were prepared by mechanical polishing using SiC sandpaper up to 2500 granulometry and subsequent fine polishing with diamond pastes of 9 µm, 6 µm 1 µm and colloidal silica with a particle size of 0.05 µm. Data were analyzed using TSL-OIM 7 and Mtex toolbox. Grains with less than two pixels were not considered in the statistical analysis. Grain boundaries with misorientations between 3° and 15° were defined as low-angle grain boundaries (LAGB). Those with misorientations greater than 15° as high-angle grain boundaries (HAGB).

The analysis of the phase composition was carried out using the X-Ray diffraction method by the Multifunctional X-ray diffractometer DRON-8. The following parameters were used for scanning: voltage 40 kV, Amperage 20 mA, scanning step 0.05°, exposure time 4 s - discrete mode, PDF-2 Release 2014 ICDD database.

Tensile tests in different zones across the sample diameter (surface and center) were evaluated using a universal testing machine at room temperature. Sample gauge dimensions of 4 mm x 1.5 mm x 2 mm tested at a constant strain rate of $1 \cdot 10^{-3}$ s^{-1}. Strain maps were obtained

by digital image correlation (DIC) during the tensile test employing the Ncorr free software [30].

3 Results and analysis

3.1 As-received material

The initial material was obtained by casting, obtaining bars of 110 mm in diameter. Thus, Fig. 3a indicates the microstructure obtained by optical microscopy (OM) after casting. This figure shows the formation of a structure of coarse grains of different sizes. Due to the solidification process in which the surfaces are cooled before the central zone, a variation in grain size occurs, as indicated in Fig. 3b. This figure indicates the existence of two families of grain size, one formed by sizes smaller than 3 mm located around the surface with an average value of 0.92 mm and the other comprising sizes between 4 mm and 8 mm located preferably in the center of the bar with an average value of 4.83 mm. Concerning alloy tensile behavior, Fig. 3c indicates that the as-cast material reaches a yield strength of 220 MPa with a fracture strain of 20%. Additionally, the EBSD characterization in Fig. 3d confirms a microstructure with large grains. Those grains are free of dislocations and substructures in its interior, as confirmed by the misorientation profile lines 1-2 and 3-4 in Fig. 3e. The misorientation profiles show constant behaviors inside the grains, and only appreciable changes in misorientation occur when crossing the grain boundaries. This yield strength reflect the effect of the alloying elements in the material, i.e., an increase in yield strength of 60% concerning high-purity electrolytic copper (87 MPa, yield strength) [31].

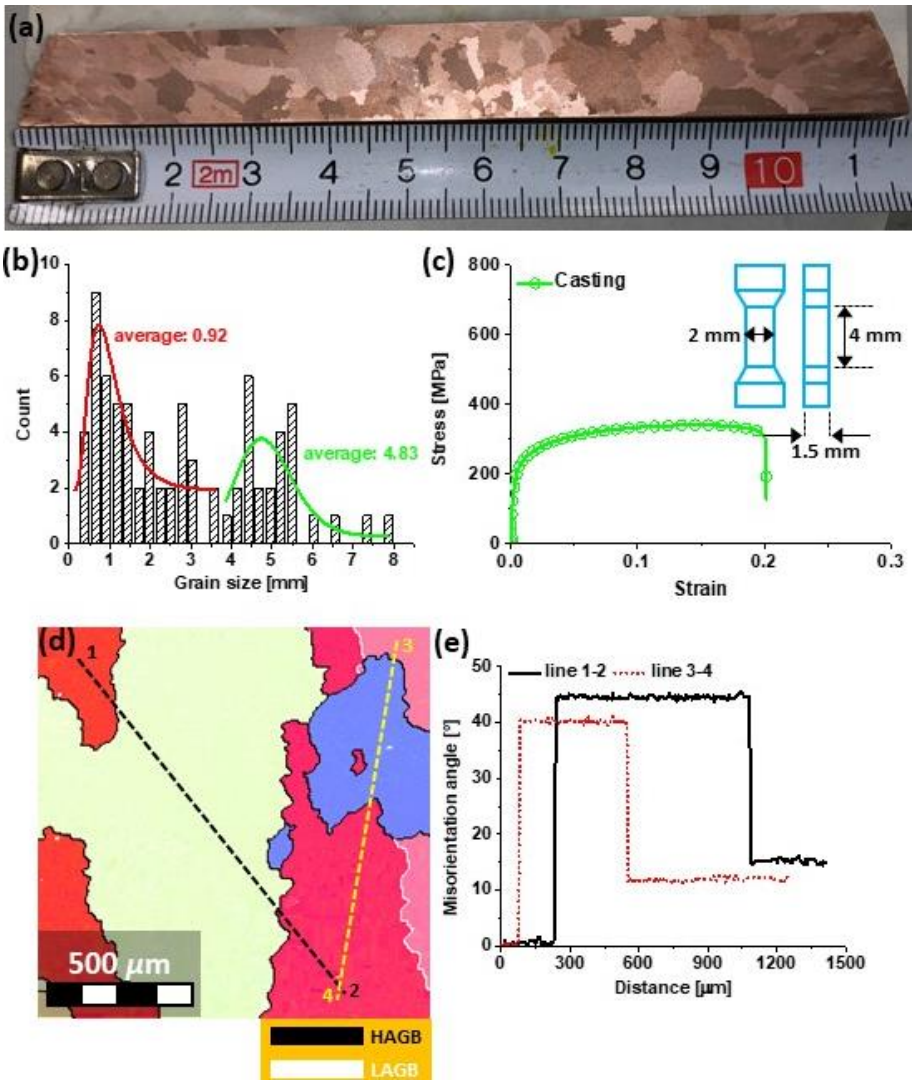

Fig. 3 Initial microstructure after casting process (a), grain size in the casting condition (b), tensile properties (c), EBSD map (d), and misorientation profiles for the lines indicated in the EBSD map (e).

3.2 Processed material

Fig. 4 display the microstructure of the rods after RSR and RSR plus heat treatment, respectively. In the RSR process, a gradient structure is formed, with a spiral morphology that reflects the helicoidal motion of metal layers in the deformation zone [16,32,33]. Fig. 4a and Fig. 4c allows seeing that the microstructure around the surface in cross-section after RSR is mainly formed by small grains with an average size of 8.22 µm. The smallest grain size is formed here due to the localization of severe shear deformations in the surface layer. Conversely, the central zone in Fig. 4b, and Fig. 4c shows a mix of small and large grain sizes ranging between 2 µm and 40 µm, with an average grain size of 15.9 µm. This effect is attributed to the heterogeneous equivalent strain distribution along the radial direction.

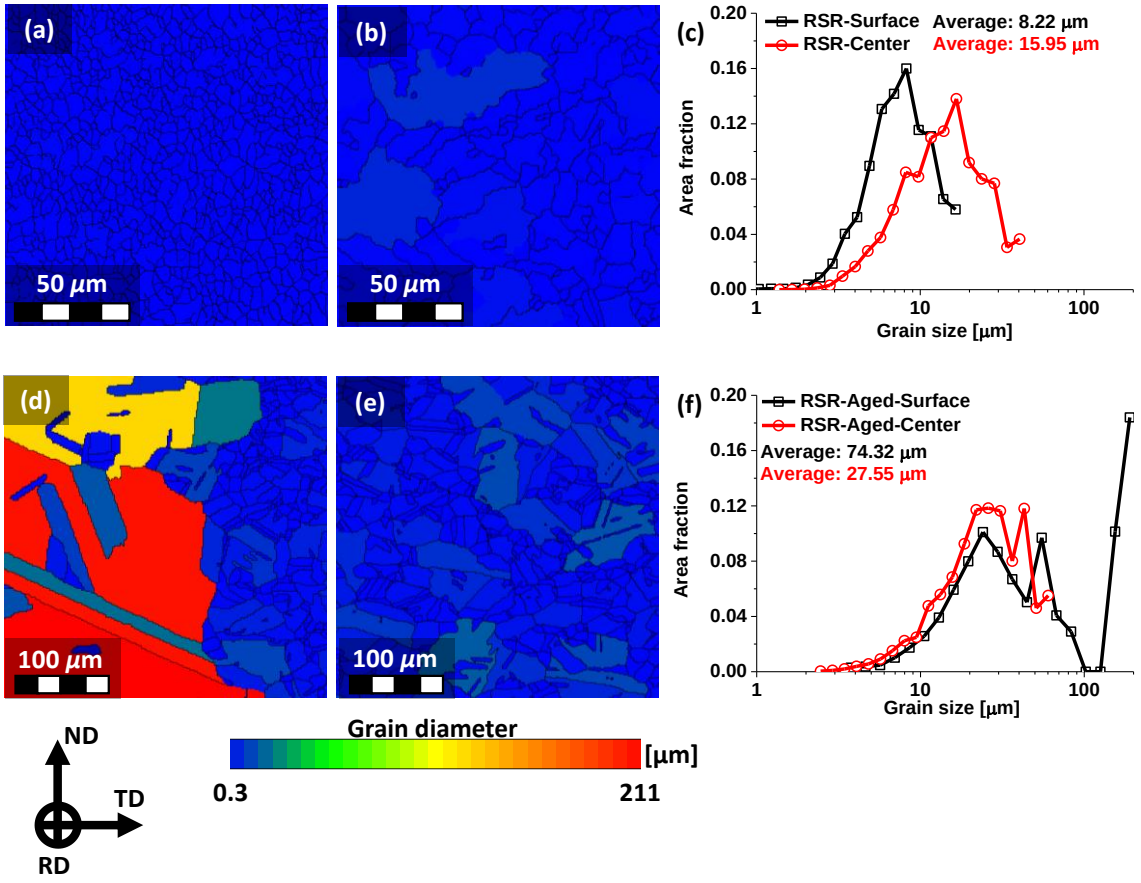

Fig. 4 Surface grain diameter map after RSR (a), center grain diameter map after RSR (b), grain size evolution after RSR (c), surface grain diameter map after RSR+aging (d), center grain diameter map after RSR+aging (e), grain size evolution after RSR+aging (f).

In the hardening process by heat treatment, Fig. 4d through Fig. 4f manifests an evident grain structure change. After the heat treatment, grain recrystallization occurs in a heterogeneous way, as the grain size increases, especially in the surface layer, which may be due to different deformation degree induced by the RSR process across the rod diameter. After the aging treatment, the microstructure evolution in Fig. 4d and Fig. 4e shows the opposite behavior concerning the RSR material. The average grain size in the central part of the rod after heat treatment is 27.5 μm. At the surface of the rod, coarse grains larger than 100 μm in size are observed, while the average grain size, according to measurements, is 74.32 μm. Besides, in the microstructure of samples after heat treatment, one can observe characteristic annealing twins formed during grain growth. Therefore, the abnormal grain growth is a consequence of the deformation gradient across the rod diameter after RSR processing. Thus, the strain heterogeneity between the rod surface and its center zone gives rise to recrystallization gradients after the heat treatment.

To better describe microstructural characteristics, energy dispersive spectroscopy (EDS) analyses were performed. Fig. 5a indicates the material's microstructure after RSR processing plus aging treatment, indicating the different regions analyzed (red squares). The SEM image allows observing the grain boundaries and the presence of particles of different sizes. In Fig. 5b, the main alloying elements' EDS map is indicated for the spectrum area 1. At first glance, it can be assessed that Ni and Cu concentrations are homogeneously distributed throughout the material. On the contrary, Cr and Si elements seem to be located in small regions forming particle colonies close to the grain boundaries. Fig. 5c shows the EDS spectra for the different areas indicated in Fig. 5a. Spectrum number 1, corresponding to the entire analyzed area shows alloying elements such as Ni, Cr, and Si. Looking in more detail at spectra 2 and 3, corresponding to the black particles observed in Fig. 5a, we see a high Si and Cr concentrations. On the other hand, spectra 4 and 5 within the grains indicate low concentrations of Cr and Si and a domain of Cu and Ni. In this way, the previous observations confirm the formation of precipitates rich in Cr, and Si with a Ni matrix enriched. Looking in more detail at the EDS maps for Cu, Si, Ni, and Cr in Fig. 5d, we see that many of the high Si concentration spots also show high Cr content. According to Rdzawski et al. [34], these particles with a high content of Cr and Si correspond to Cr_3Si precipitates, which are preferentially located around the grain boundaries.

Aging treatment also favors the precipitation of Ni_2Si phases in the matrix as particles uniformly distributed in the bulk of the samples in the form of small inclusions. Cheng et al. [35] also reported the formation of this type of precipitates after aging at a temperature of 500 °C for a Cu-Ni-Si-Cr alloy. Analyzing the EDS images for each element using ImageJ [36], an appreciation of the precipitate particles' size can be made, as indicated in Fig. 6. The histograms show an average particle size between 0.56 μm and 0.65 μm that follows a lognormal function. The inset in Fig. 6 highlights a microstructure where some small particles appear either inside the grains (blue ellipse) or forming colonies close to the grain boundaries (green ellipse). However, several authors have reported via TEM that after plastic deformation, the Cu-Cr-Ni-Si alloy can form nano-precipitates with average sizes of 8 nm [35,37]. Therefore, the analyses from the SEM images represent a more descriptive than quantitative result of the precipitates' real size.

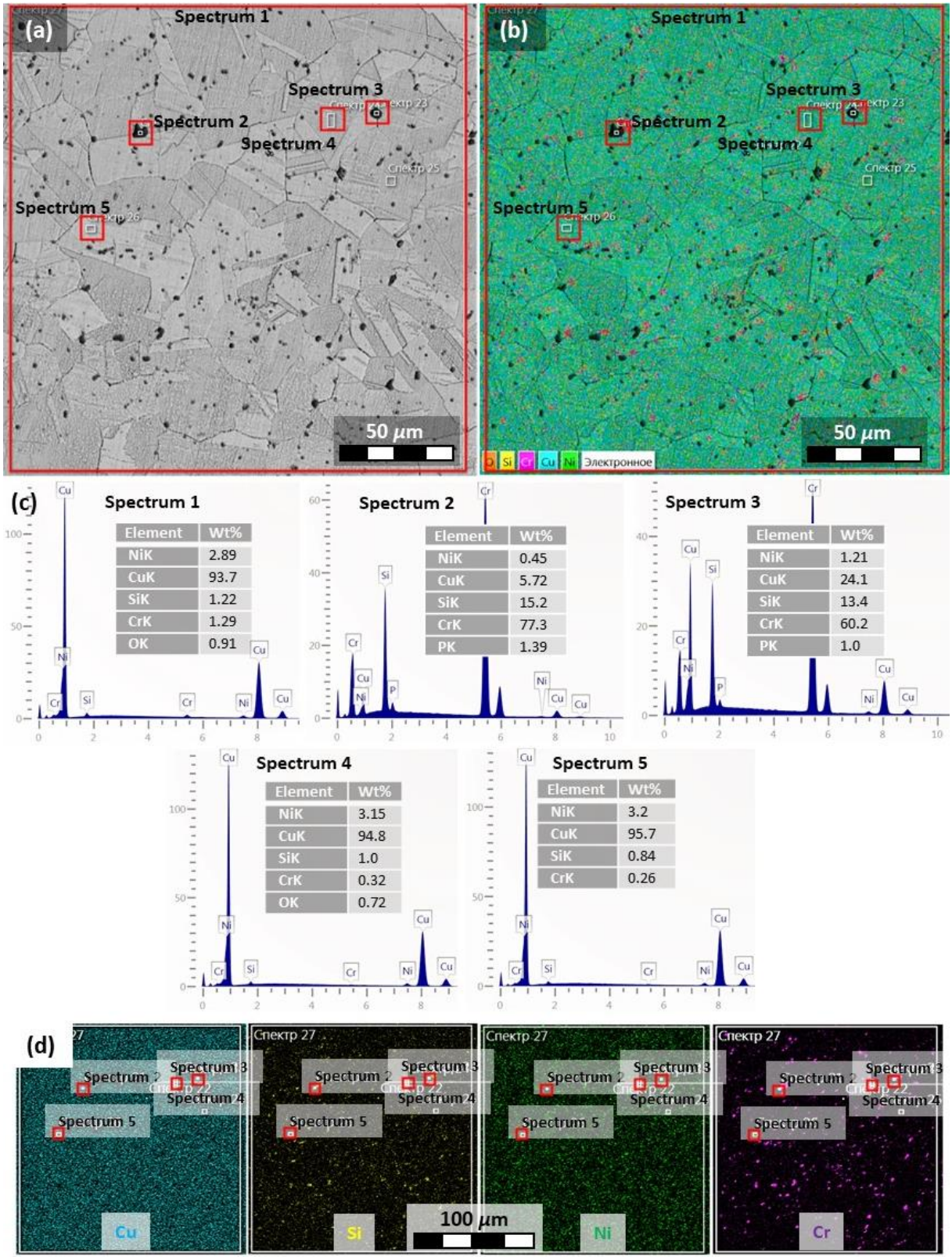

Fig. 5 SEM map after aging treatment (a), EDS map (b), EDS spectrums for the red squares indicated in figure (a) (c), and Cu, Si, Ni, and Cr EDS maps (d)

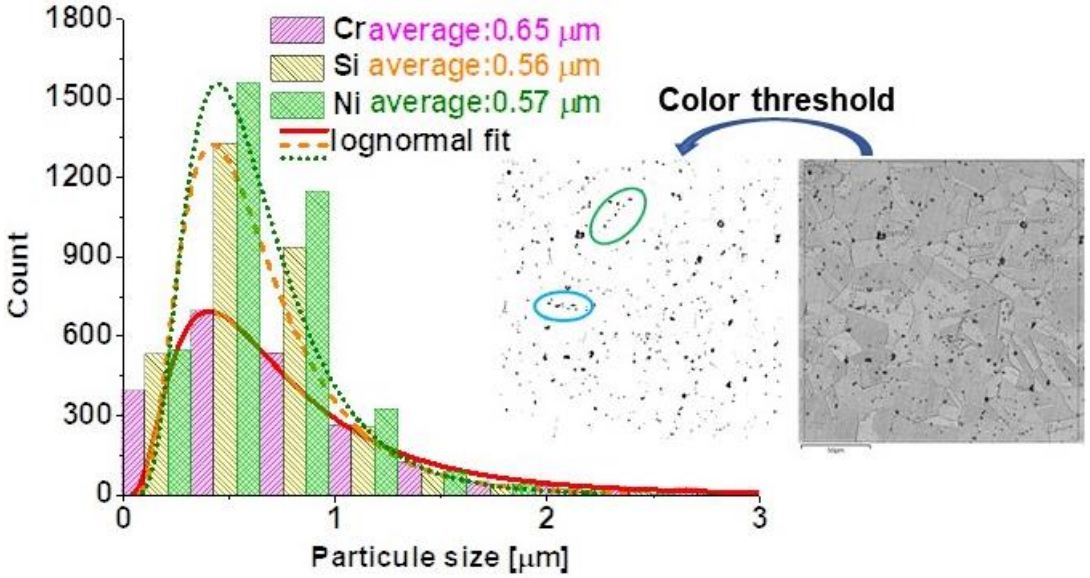

Fig. 6 Precipitation particles sizes.

X-ray diffraction confirms the formation of different types of precipitates such as Cr_3Si and Ni_2Si. Fig. 7 shows the diffraction patterns for samples after RSR and aging heat treatment. It can be seen that the chromium silicide and nickel silicide phase concentrations are about 0.84% and 0.9%, respectively. Samoilova et al. [38] showed that for the Cu-3%Ni-1.5%Si-1%Cr alloy, the main phases observed after heat treatment are Cr_3Si and Ni_2Si. The formation of these precipitates suggests the activation of an additional hardening mechanism in the material processed by RSR and subsequently heat treated.

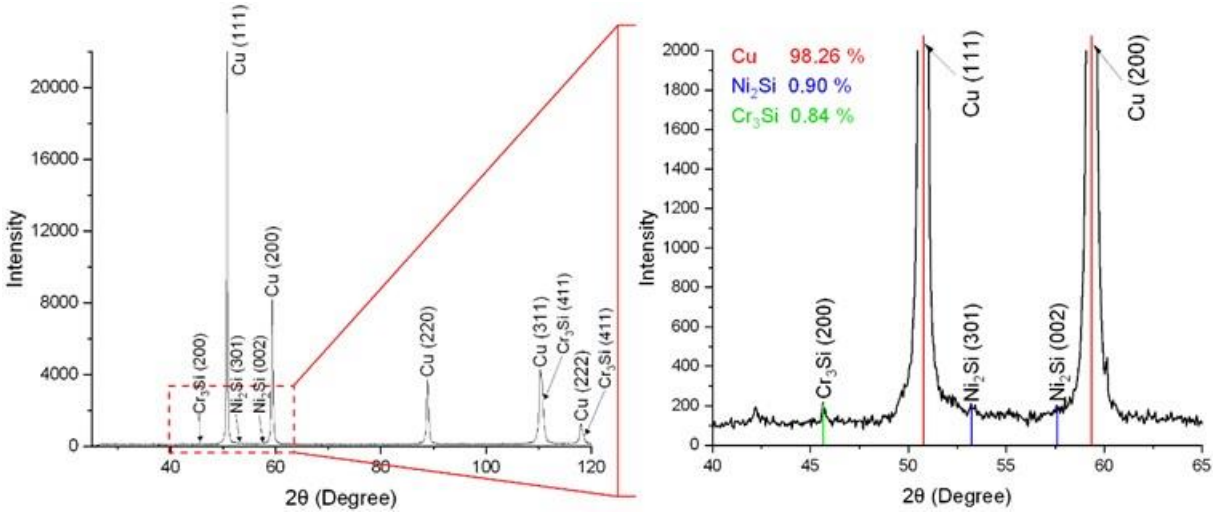

Fig. 7 Diffraction pattern for the Cu-Ni-Cr-Si alloy after RSR + Aging treatment

3.3 Mechanical properties

Fig. 8 shows the hardness distribution in the cross section for both conditions RSR and heat-treated RSR. The RSR material shows some hardness variation from the surface to the rod center. The opposite behavior is observed in the heat-treated RSR material, where hardness values are high close to the center and decrease near the surface. Additionally, a hardness value of ~260-280 HV above the ~180-200 HV of the RSR condition was obtained after the aging treatment representing a hardness increment of 40-45%.

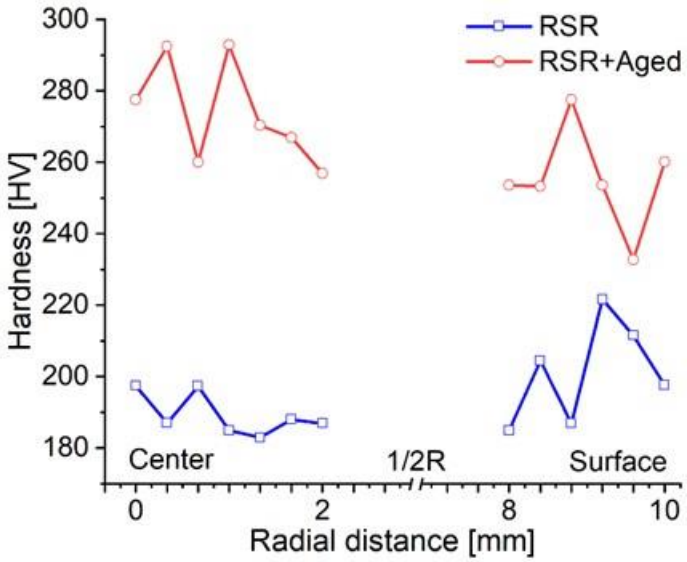

Fig. 8 Hardness evolution in the cross section after RSR and RSR + aging treatment.

According to the standard specifications for this alloy, the Vickers hardness of hot-pressed rods should not be lower than 200 HB (210 HV) [39]. Thus, the obtained hardness values for aged samples are higher than the standard values.

Fig. 9a illustrates typical engineering stress-strain curves for samples subjected to RSR and aging treatment. It worth mentioning that the samples cut near the surface of the rod and in its center region differ on their mechanical strengths, what is explained by the microstructure heterogeneity of the samples in those zones. After hot radial-shear rolling with a total elongation ratio μ = 9.0, the ultimate tensile strength is ~ 480-520 MPa, the yield strength is about 355-392 MPa. At the same time, the strain to failure lies typically around 0.22 and 0.27 for the center and surface samples, respectively.

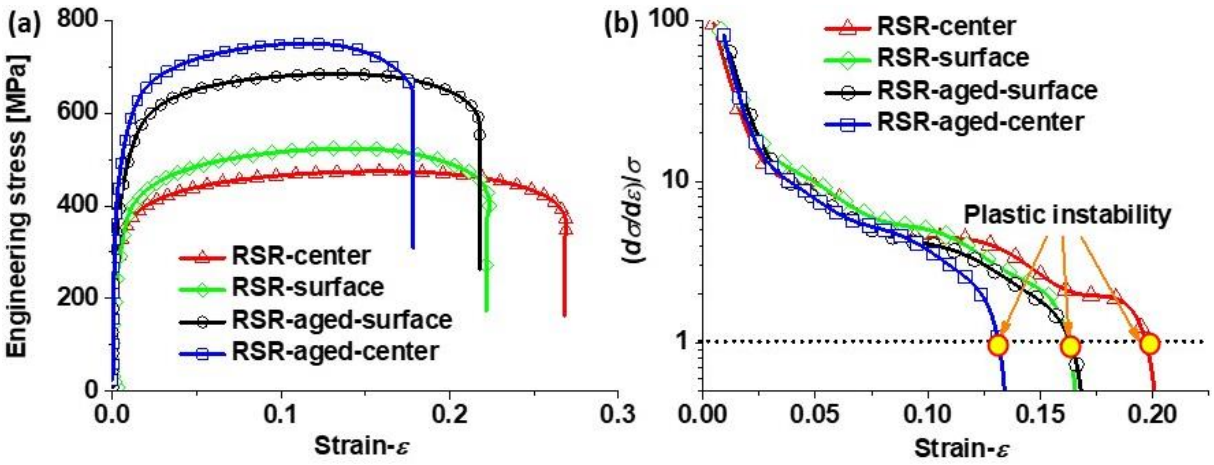

Fig. 9 Mechanical properties at different zones of the samples after RSR and RSR + aging, (a) tensile curves, and (b) Considère criterion evolution.

As a result of the aging of the samples, the ultimate tensile strength increases to 650–750 MPa, the yield strength increases to 557–606 MPa, and the strain to failure lies in the range 0.17–0.22. Although the microstructure shows a marked difference in grain sizes between the surface and the center, the tensile specimens do not correspond precisely to each zone. This is because the specimens' minimum thickness was 1.5 mm, which indicates that the surface sample also considers grains from the central area. Therefore, although the tensile samples cover more than one region, the strength increments due to aging, and the strength-ductility changes between the two zones can still be differentiated—these behaviors in good agreement with the hardness values. The mechanical properties increase is explained by the presence of two hardened excess phases. The Ni_2Si phase hardens the alloy due to dispersion hardening through aging, and the Cr_3Si phase increases the strength properties because of the structure heterogenization [40]. As shown in [40], the Cr_3Si phase is formed during crystallization and does not depend on subsequent deformation and heat treatment, and thus can prevent grain growth. On the other hand, high strength nickel silicide Ni_2Si phase precipitates in the matrix in the form of dispersoids during the aging process.

Additionally, Fig. 9b represents the Considère criterion evolution for the tensile curves of Fig. 9a. This criterion establishes that the appearance of plastic instability occurs when the strain hardening rate $(\partial\sigma/\partial\varepsilon)$ equals the flow stress (σ) of the material according to the following equation [41]:

$$(\partial\sigma/\partial\varepsilon)/\sigma \leq 1 \qquad (3)$$

This figure shows that the heat-treated material reaches plastic instability first, especially the center area. On the other hand, the surface area of the two materials (i.e., RSR

and RSR + HT) show similar behaviors. On the other hand, the material deformed by RSR indicates more significant extensions of the homogeneous deformation zone, resulting in plastic instability at higher deformations. This behavior can be associated with the fewer number of precipitates in the RSR material leading to a greater mean free path for dislocations movement and larger deformation before fracture. The Considère plot also allows checking the heterogeneity of both materials across the diameter of the bars.

4 Discussion

The processing of the alloy by RSR produces heterogeneity in the material, what can influence its properties, giving it a combination of unusual properties such as good strength and ductility or good strength keeping good electrical conductivity. In this way, the discussion of the results obtained in this work will focus on microstructural and mechanical heterogeneity.

4.1 Microstructure strengthening

Material heterogeneity is transferred to the deformation evolution as indicated by the strain maps analyzed at the plastic instability points represented in Fig. 9b. In this way, Fig. 10a demonstrates that the RSR material achieves higher deformations than the aged material. Furthermore, strains in the center and surface areas of the deformed material are 40% (0.08/0.2) and 43.7% (0.07/0.16) higher than the average value. This behavior explains the better ductility of the RSR material. On the other hand, for the heat-treated material, Fig. 10b indicates lower deformations along the length of the tensile samples, highlighting that the surfer area achieves higher strains than the center region. Therefore, the lower ductility of the aged material is associated with the appearance of several peaks along the length of the tensile sample, as Fig. 10b shows. This behavior can be associated to a more significant number of precipitates that give rise to multiple stress concentration points as a consequence of interaction between precipitates, dislocations and dislocations sources.

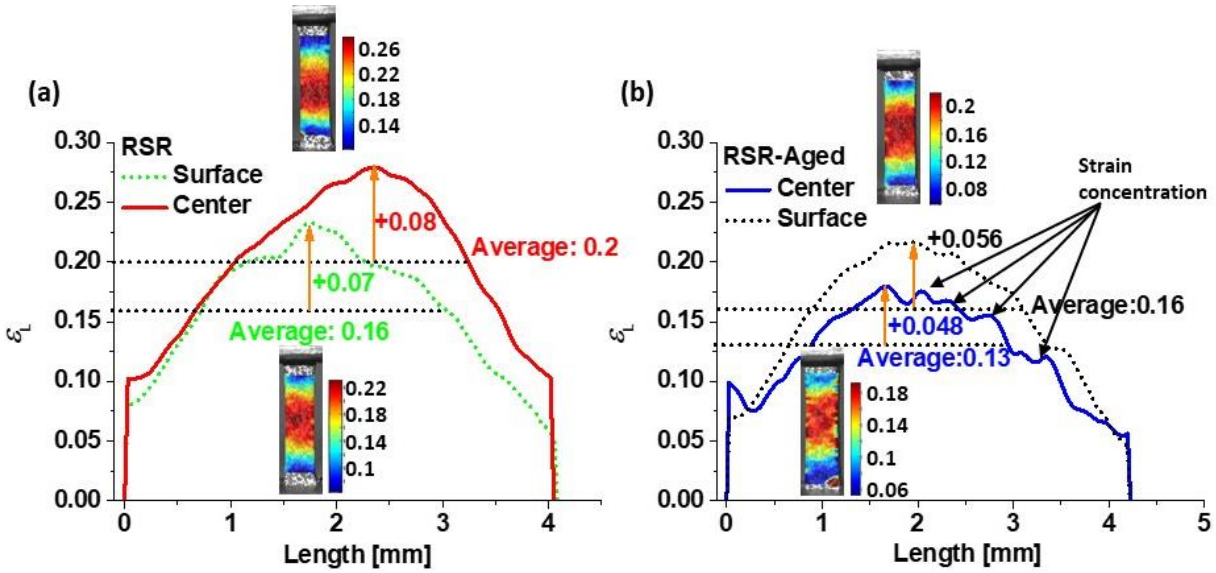

Fig. 10 Strain evolution at the plastic instability points indicated in Fig. 9b, (a) RSR, and (b) RSR+aging.

Copper and aluminum alloys present different contributions to their strengths, e.g., from lattice friction stress (σ_0) equal to 20 MPa [37], grain size (σ_G), solid solution elements (σ_{SS}), precipitates (σ_P), and dislocations (σ_ρ). Thus, the material yield strength (σ_Y) can be described by the sum of the different components, as indicated by equation (4) [42]:

$$\sigma_Y = \sigma_0 + \sigma_G + \sigma_{SS} + \sigma_P + \sigma_\rho \tag{4}$$

Where the grain size contribution follows the next equation:

$$\sigma_G = \frac{k_{HP}}{d^{1/2}} \tag{5}$$

with k_{HP} as the de Hall-Petch slope, with a value of 112 MPa·μm$^{1/2}$ [43], and d the average grain size. In this way, the first two terms of equation (4) correspond to the Hall-Petch equation, so: $\sigma_{HP} = \sigma_0 + \sigma_G$.

The solid solution contribution from Ni and Si can be expressed by the next equation:

$$\sigma_{SS} = M\frac{G\epsilon_{SS}^{3/2}c^{1/2}}{700} \tag{6}$$

where M = 3.06 is the Taylor factor, G the shear module for Ni and Si (77 GPa and 65 GPa, respectively), c the Ni and Si fractions, and ϵ_{SS} is a parameter that correlates the energy from dislocations (edge and screw) with the resolved shear stress per unit solute concentration. ϵ_{SS} can take values of 0.559 and 1.17 for Ni and Si, respectively [37].

On the other hand, the dislocation contribution can be obtained through the equation (7):

$$\sigma_\rho = \alpha M G b \sqrt{\rho} \tag{7}$$

where α = 0.3 is a dislocation hardening constant, M= 3.02 the Taylor factor, G = 44 GPa as the copper shear module, and b = 0.255 nm the matrix Burgers vector. Therefore, for the RSR material, the dislocations' contributions can be obtained assuming that the precipitation effect is absent. From equation (4), contributions of 291 MPa and 243 MPa can be obtained for the surface and center, respectively. Employing equation (7), dislocation densities between 8.1×10^{14} m^{-2} and 5.7×10^{14} m^{-2} can be estimated, which agree with values reported by other investigations. E.g., Watanabe et al. [44], after processing a Cu-Ni-Si alloy using high-pressure torsion (HPT), reported a dislocations density of 8×10^{14} m^{-2}, which remained in the peak aged state and it was reduced to 6×10^{14} m^{-2} in the over-aged state. For the RSR + aged material, the precipitates contribution was obtained as the difference in the aged material's yield strength and the as-cast state.

In this way, Fig. 11 collects the different strength contributions of the materials obtained through equations (4)-(7). Fig. 11a indicates how the main strength contribution comes from dislocations. It is also shown that in the surface zone, the second contribution associated with the grain size is due to the bigger grain refinement in this area, as shown in Fig. 4a. After the aging treatment, Fig. 11b shows that the main strength contributions come from the precipitates and dislocations components in both the surface and center areas. This behavior demonstrates the greater strength of the heat-treated material concerning the RSR as a consequence of the additional contribution of the precipitates. Fig. 11b shows that the aging treatment generated larger amounts of precipitates near the center due to a possible recrystallization gradient as a consequence of the microstructure heterogeneity after the RSR process. Thus, hardness and the yield strengths values lead to infer that the RSR method is a good and versatile alternative for the production of rods with diameters in the range of 10-55 mm.

Using the model proposed by Kocks et al. [45], which describes the rate of change in the density of dislocations with deformation ($\frac{\partial \rho}{\partial \varepsilon}$) as a function of the density of dislocations (ρ), it is possible to know more about dislocations in materials through the following equation:

$$\frac{\partial \rho}{\partial \varepsilon} = M(K_1\sqrt{\rho} - K_2\rho) \quad (8)$$

Where the terms $K_1\sqrt{\rho}$ and $K_2\rho$ describe the storage and recovery or annihilation of dislocations, respectively, and M the Taylor factor. Through Fig. 11c, the adjustment of equation (8) is indicated for each plastic zone of the traction curves of Fig. 9a. When the dislocation density evolution during the tensile test is not known, it can be approximated by the change in the yield stress (i.e., $\rho \propto (\sigma - \sigma_Y)$). Hence, the change in the density of dislocations with the deformation is proportional to the strain hardening rate (i.e., $\frac{\partial \rho}{\partial \varepsilon} \propto \frac{\partial \sigma}{\partial \varepsilon}$).

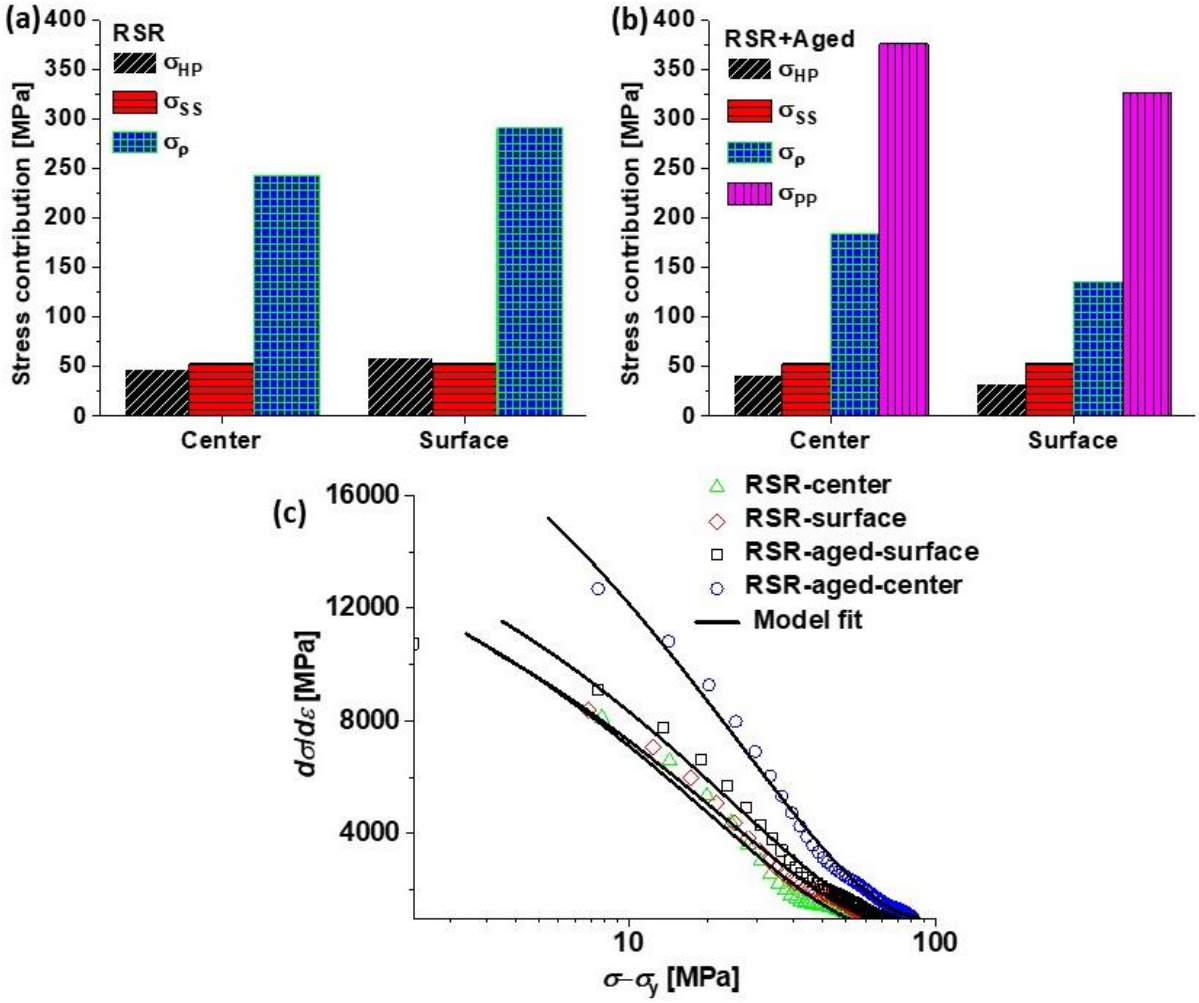

Fig. 11 Strength contributions for the (a) RSR, (b) RSR+aged conditions, and (c) Kock's model fitting.

The curve fits show good correlations that allow the calculation of K_1 and K_2 values as summarized in Table 4 for the different conditions and areas analyzed. Initially, it is observed that the surface of the material processed by RSR register greater values for both the K_1 and K_2

coefficients than the center. Conversely, the RSR + aged material exhibits the oppositive behavior, i.e., greater values for both the K_1 and K_2 in the center than in the surface. However, between the two conditions, there is a marked difference for the coefficients. The RSR + aged material has a lower dislocation multiplication rate of approximately half of the one for RSR material. On the other hand, the dislocation annihilation rate in RSR + aged material is lower than in RSR. This behavior is due to the lower density of dislocations in the RSR + aged material due to the previous annihilation of dislocations by the solubilization and aging treatment. However, it should be noted that the dislocation annihilation magnitudes are much lower than those observed in severe plastic deformation processes where magnitudes close to 1000 are reached for the K_2 coefficient [46]. Thus, the low dislocation annihilation rate suggests a good strain hardening capacity in the RSR + aged material.

The aging treatment effect is also reflected in the material grain boundaries character. Table 4 indicates a substantial change in the fraction of high-angle grain boundaries (HAGB) obtained by EBSD from 47% in the RSR state to a microstructure dominated by HAGB with a fraction larger than 97%. Thus, using the equation proposed by Read-Shockley, the energy contributions of the different types of grain boundaries can be quantified [47]:

$$\gamma(\theta) = \begin{cases} \gamma_m \frac{\theta}{15}\left[1 - ln\left(\frac{\theta}{15}\right)\right], if\ \theta \leq 15° \\ \gamma_m, if\ \theta > 15° \end{cases} \quad (9)$$

With $\gamma_{\mathrm{m}} = 0.625$ J/m^2 representing the energy per unit area of a HAGB and θ the misorientation angles. Hence, the average energy ($\bar{\gamma}$) is obtained as the sum of the different contributions of the misorientation angles as indicated in the following equation [47]:

$$\bar{\gamma} = \sum_{2}^{63.5} \gamma(\theta) f(\theta) \quad (10)$$

where $f(\theta)$ is the fraction of a determined misorientation. While the energy stored in grain edges can be obtained through the following equation [47]:

$$E_b = \frac{2\bar{\gamma}}{d_{sub-grain}} \quad (11)$$

Solving equations (9)-(11), the energy stored in the grain boundaries is obtained as indicated in Table 4. Despite the average energy increases after the aging treatment due to the increase in

the HAGB fraction, the boundary stored energy decreases as a consequence of the subgrain growth. This behavior shows that the increase in the temperature in the material due to the heat treatment after RSR processing produces abnormal grain growth and a reduction in stored dislocations, especially geometrically necessary dislocations (GNDs).

Table 4. Microstructural properties

Condition	K_1	K_2	%HAGB	ρ [m^{-2}]	$d_{\mathrm{sub-grain}}$ [μm]	$\bar{\gamma}$ [J/m^2]	E_b [J/g]
RSR-surface	1.1×10^{10}	126.8	47.2	8.1×10^{14}	3.20	0.52	0.036
RSR-center	9.8×10^{9}	112.9	40.7	5.7×10^{14}	7.14	0.50	0.016
RSR-aged-surface	3.8×10^{9}	54.8	98.1	1.7×10^{14}	13.05	0.62	0.011
RSR-aged-center	4.6×10^{9}	63.7	97.9	2.1×10^{14}	11.85	0.62	0.012

Fig. 12 shows the substantial change in the grain boundaries' misorientations, highlighting different types of boundaries. For example, it is noted that the material properties after RSR processing are dominated by low-angle grain boundaries (LAGB) with small fractions of twins and coincident sites lattice (CSL), especially in the surface area. Conversely, after aging, the presence of misorientation peaks for angles of 38.9° and 60° corresponding to twins of the type ⟨110⟩ and ⟨111⟩, respectively, is appreciated. Therefore, the RSR+aged material boundaries are mainly formed by a high fraction of twins and CSL, as indicated by the misorientation distributions and the CSL maps.

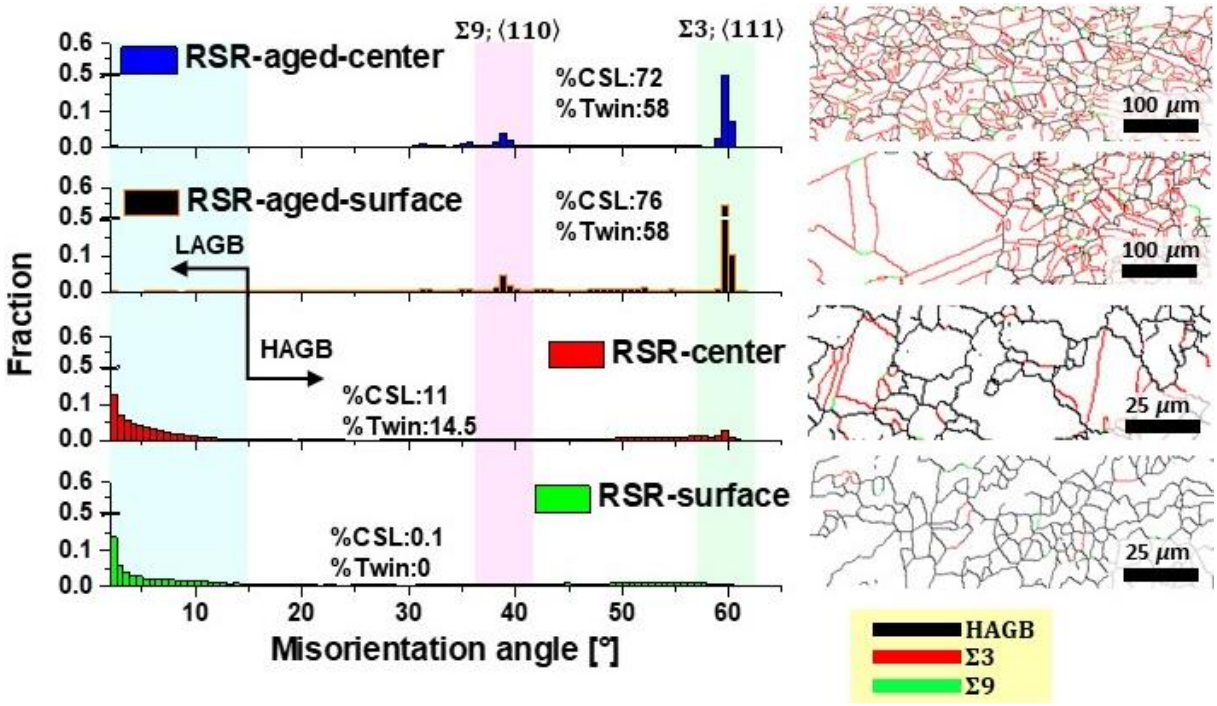

Fig. 12 Misorientation angle distributions and CSL maps for the different zones across the rod radius

The presence of Σ3 coherent twins in low stacking fault energy (SFE) face-centered cubic (FCC) structures such as copper has been related to the combination of deformation processes followed by heat treatment. In this study, the multiple RSR passes of deformation until obtaining the desired diameter combined with the heat treatment at high temperature promote the grain boundaries character change. In this way, it can be established that the effect of temperature after RSR processing changes the boundaries that initially contain high energy to a coherent twin form. The large number of Σ3 grain boundaries observed in the RSR + aged material may favor mechanical properties such as fatigue strength by reducing the rate of crack propagation since these boundaries are less prone to intergranular fracture [48].

4.2 Material heterogeneity

The RSR processing generates a heterogeneous state of deformation between the surface and the center of the bar. This deformation state gives rise to more prominent grain refinement close to the rod surface while the areas away from the surface present a larger grain size (see Fig. 4a and Fig. 4b). This heterogeneity prior to the aging treatment results, in the more deformed areas (that is, a larger number of subgrains, high density of GNDs, and high energy) after aging in a more accelerated recrystallization phenomenon than in the center of the bars. According to Muñoz et al. [49,50], bars of metallic materials processed by high magnitudes of plastic deformation can generate microstructural gradients when applying high temperatures. This

behavior is attributed to the fact that the temperature necessary for recrystallization is lower in the deformed areas than in the less deformed ones. In this direction, since the areas near the surface are more deformed than the center of the bar and the quenching temperature of the aging treatment is much higher than the copper recrystallization temperature (i.e., 960 °C for the quenching followed by the 495 °C for the aging, both higher than 200 °C, copper recrystallization temperature), it is easier to go from recrystallization to abnormal grain growth on the surface than in the center of the rod.

The grain fragmentation, recrystallization, multiplication, and annihilation of dislocations in the alloy are corroborated by the representation of kernel average misorientation (KAM) in Fig. 13a. This figure shows that through the KAM distributions and maps, the microstructure after RSR registers higher KAM values inside the grains than in the RSR + aged material. This behavior is due to the more significant presence of mobile dislocations inside the grains generated by the RSR process's deformation. These dislocations generate curvature in the grains that translate into orientation differences inside the grains, indicating potential places for further grain size reduction. On the other hand, after the solubilization and aging treatment, the annihilation of dislocations and subsequent grain growth takes place in the material microstructure. Thus, a continuous curvature in the material's microstructure with lower and less scattered KAM values is observed for the RSR+aged material.

In this order of ideas, Fig. 13b indicates the average grain size evolution for both RSR and RSR + aged, in the bars' radial direction. This figure confirms the formation of microstructural gradients in both processes. The grain size profiles for the RSR process demonstrate a more significant grain size refinement in the vicinity of the bar surface, which begins to change towards the center of the bar with grain growth that approximately doubles the size of the surface. On the other hand, after the aging treatment, the material experiences a substantial change in the grain size growth, especially in the surface's neighborhood, becoming 20 times greater than the material before aging. Thus, moving away from the aged material's surface, the formation of an interface can be observed where the transition from large grain sizes (~ 200 μm) to smaller sizes (~ 40 μm) occurs. Hence, grain size profiles demonstrate the formation of a recrystallization gradient, which is more intense at the surface than at the center of the rod.

As a consequence of the aging treatment, the recrystallization phenomenon gives rise to larger grain size in the RSR + aged material than in the RSR condition. However, Fig. 13c indicates that, although the grain size in the RSR + aged material is much larger than the RSR, the former's yield strength is greater than that of the latter. This apparent contradiction is supported by the precipitation hardening mechanism. According to various authors and studies using TEM [51,52], the processing of Cu alloys with plastic deformation and subsequent aging heat treatment gives rise to the formation of nanoprecipitates. The authors showed that nanoprecipitates act as elements that pinned the dislocations while dividing them, creating more defects. Therefore, under the influence of stress, nanoprecipitates act as elements that nucleate new dislocations, and that can help to improve ductility. Thus, it can be established and confirmed that the main hardening mechanisms come from dislocations and precipitates.

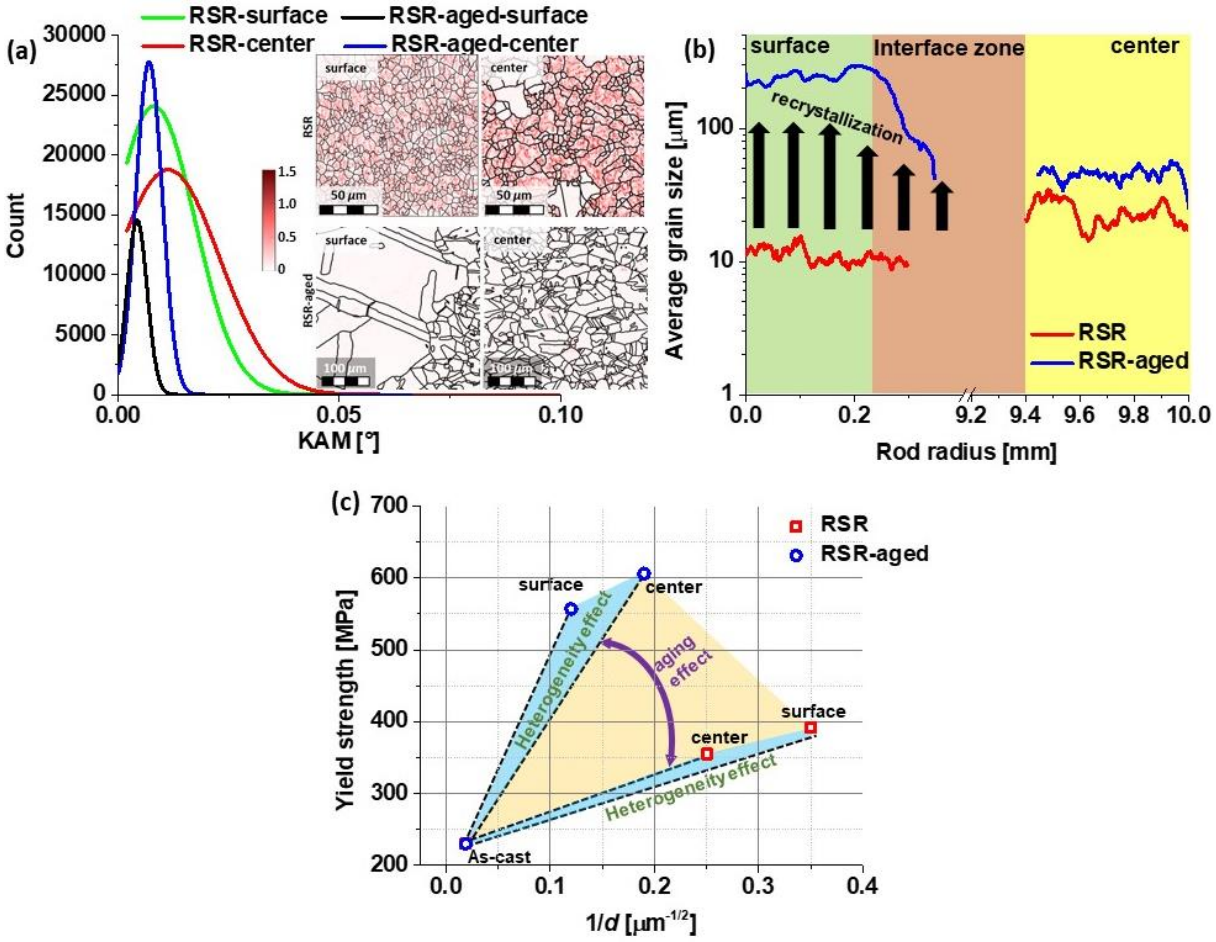

Fig. 13 Microstructure heterogeneity, KAM maps and distributions across the rod radius (a), average grain size profiles after RSR and RSR+aged treatment (b), and yield strength and grain size changes after RSR and RSR+aged treatment (c).

4.3 Electroconductivity and hybrid properties

The conductivity measurements are presented in MS/m (megasiemens/meter) and %IACS, that is, as a percentage of pure copper's conductivity (58 MS/m). Fig. 14 shows a diagram of the electrical conductivity values after RSR and aging treatment. At first glance, the heat treatment has a significant effect on electrical conductivity. However, after RSR, the electrical conductivity is 30.52% IACS. Quenching and subsequent aging of the samples lead to an increase in the electrical conductivity value by 48% (Fig. 14). Therefore, the electrical conductivity increment of the aged material is associated with the purification phenomenon of the Cu matrix with precipitates, as demonstrated by the EDS maps and by Yang et al. [51] in a Cu alloy deformed by rolling and subsequent aging treatment.

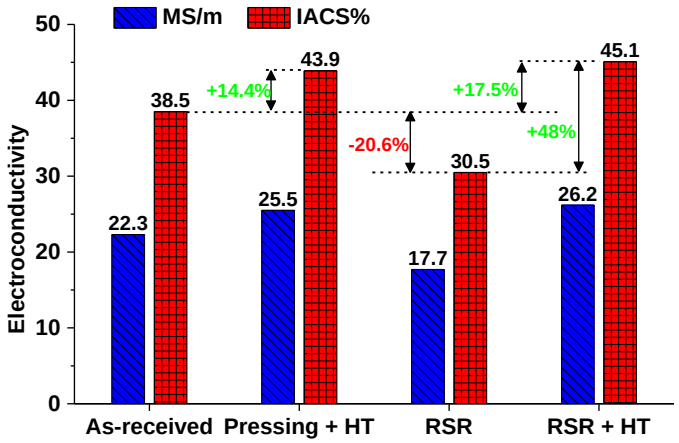

Fig. 14 Electrical conductivity of Cu-Ni-Cr-Si alloy after RSR and heat treatment

The technical standard for Cu-Ni-Cr-Si alloy semi-finished products shows a conductivity value of at least 24 MS/m. Therefore, the two analyzed conditions comply with this requirement. It is also worth noting that these values are obtained based on the conditions used in an industrial environment to obtain semi-finished products by extrusion and drawing.

Table 5 compares the Cu-Ni-Cr-Si alloy properties obtained by an industrial method of hot extrusion (e.g., drawing) and the properties of rods subjected to RSR. The main requirements for heat-resistant low alloy products for electrical purposes are hardness and electrical conductivity. In addition, thermal conductivity and strength properties can be taken into account. Therefore, the main task when choosing technological modes of deformation and hardening heat treatment is to find the best compromise between hardness and electrical conductivity. So, rods obtained by the RSR method meet the electrical conductivity requirements of technical standards and the hardness.

The RSR + aged material's improvement electrical conductivity concerning the RSR is associated with factors such as the decrease in the density of dislocations, Cu matrix purification, and the change in the grain boundaries character because of the heat treatment after RSR processing. The effect of temperature leads to dislocation annihilation and grain growth reflected in a lower density of grain boundaries. According to Wu et al. [37], electrical resistivity is a function of different contributions such as dislocations, solid solution, precipitates, and grain boundaries. Therefore, it is clear that the RSR material's resistivity is higher due to the greater number of dislocations and grain boundaries.

Table 5. Comparative properties indicators of the rods made of Cu-Ni-Cr-Si alloy

Parameter name	Method of hot deformation	
	Extrusion or drawing [39]	Radial-shear rolling
Hardness (HV)	210	260-280
Ultimate tensile strength (MPa)	750	650-750
Yield strength (MPa)	700	557-606
Elongation (%)	10	12-17
Electrical conductivity (MS/m)	24	26.2

For a better appreciation of the effect of the RSR and RSR + aged processes on the alloy properties, Fig. 15a shows the relationship between mechanical strength and conductivity for various copper alloys. As a first observation, depending on the alloying elements, different behaviors are highlighted. For example, the alloys of Cu-Ni-Si-Al [53,54] and Cu-Ni-Co-Si-Mg [55] reach strengths larger than 900 MPa due to the formation of Ni and Si clusters with sizes of 2 nm. However, the conductivity was lower than 30% IACS and the homogeneous elongation less than 5%. Comparing the current RSR + aged alloy with alloys of the same type Cu-Ni-Si-Cr [35,37,56] it was found that these latter alloys achieved high strengths (> 700 MPa) with conductivity values lower than 27% IACS and above 45% IACS when the material is pre-formed by rolling. These observations suggest that the use of the RSR process and the combination with the aging treatment gives rise to a wider range of properties than the simple use of heat treatments. On the other hand, the alloys of Cu-Ni-Si [57–59], and with additions of Vanadium [60] deformed by rolling and later aging, allow to achieve high electrical conductivities (> 50% IACS) at the cost of their mechanical strength reduction. Therefore, Fig. 15a confirms that the methodology proposed in this study allows obtaining remarkable properties in terms of conductivity that are similar to alloys like Cu-Ni-Si-Ti [61–64], Cu-Ni-Si-Co-Cr [65], and Cu-Ni-Si-P [66]. Additionally, Fig. 15b proves that the heterogeneous

microstructure produces an alloy with a strong combination of strength and ductility. Finally, it can be concluded that the RSR process, together with the appropriate aging heat treatment, allows obtaining a structural heterogeneous copper alloy that stands out among different copper alloys by combining strength, conductivity, and ductility.

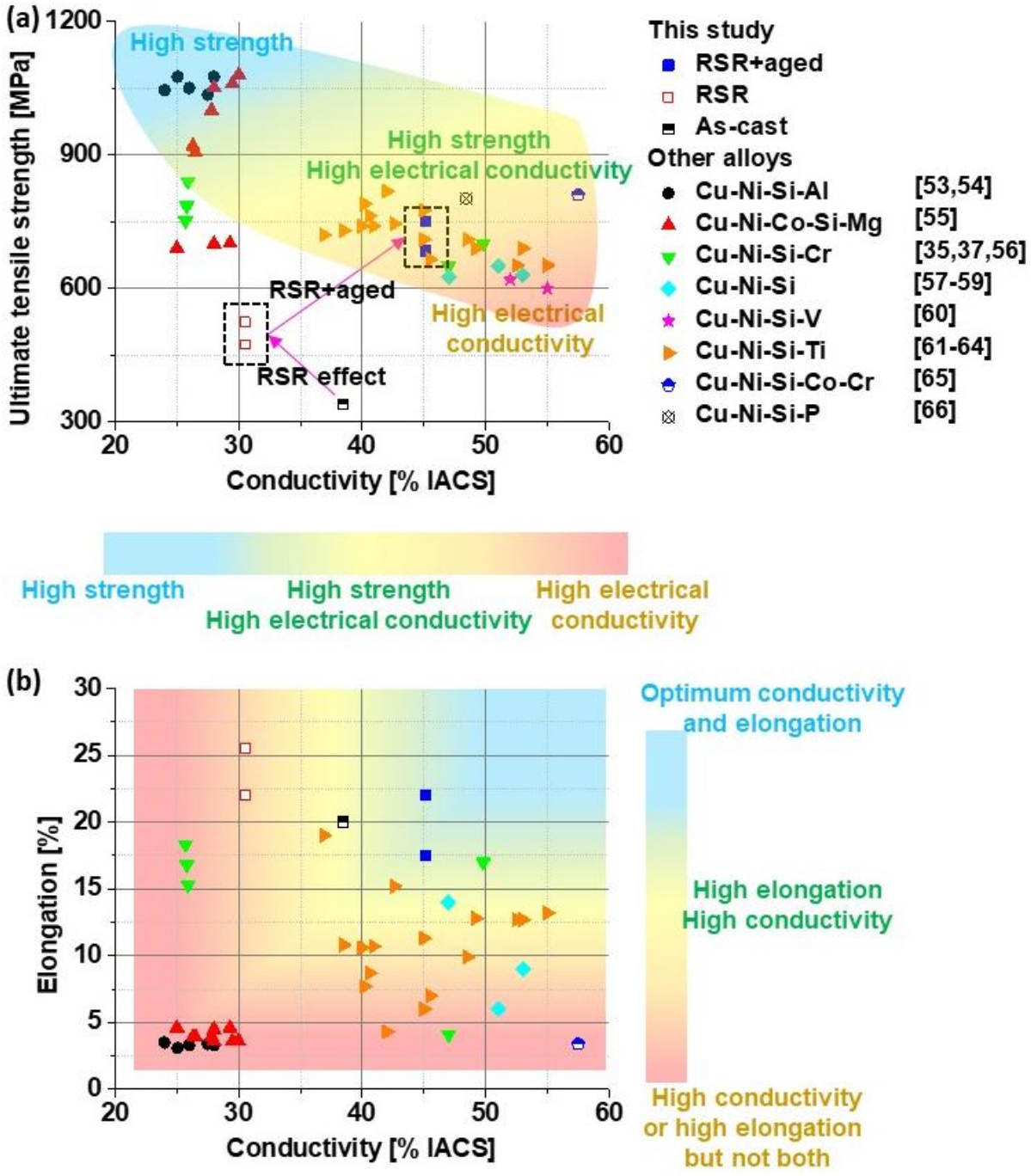

Fig. 15 Comparison of the Cu-Ni-Cr-Si alloy properties with different Cu alloys: Cu-Ni-Si-Al [53,54], Cu-Ni-Co-Si-Mg [55], Cu-Ni-Si-Cr [35,37,56], Cu-Ni-Si [57–59], Cu-Ni-Si-V [60], Cu-Ni-Si-Ti [61–64], Cu-Ni-Si-Co-Cr [65], Cu-Ni-Si-P [66]. Ultimate tensile strength and conductivity (a), and elongation vs conductivity (b).

5 Conclusions

The article describes a method for producing semi-finished products from a Cu-Ni-Cr-Si alloy by the radial-shear rolling process.

1. In the radial-shear rolling process, the alloy hardening occurs due to intense shear deformations in the surface layers of the rod, giving rise to microstructure heterogeneity. Subsequent aging treatment leads to precipitation hardening due to the release of Ni_2Cr and Cr_3Si hardener phases dispersed in the matrix as particles uniformly distributed in the bulk of the samples in the form of small inclusions with an average size of 0.56-0.65 μm.

2. The RSR process generates deformation gradients that, after the aging heat treatment, are transformed into recrystallization gradients in the bars' radial direction that give rise to a structural material with a remarkable combination of strength ductility and electrical conductivity. Therefore, the abnormal grain growth results from the deformation gradient across the rod diameter after RSR processing. Thus, the strain heterogeneity between the rod surface and its center zone gives rise to recrystallization gradients after the heat treatment.

3. After RSR, the main strength contribution comes from dislocations. The second contribution is associated with the grain size due to the greater grain refinement. After the aging treatment, the main strength contributions come from the precipitates and dislocation components in both the surface and center areas. This behavior demonstrates the greater strength of the heat-treated material concerning the RSR due to the additional contribution of the precipitates.

4. After RSR and heat treatment, the alloy increased the strength by 50% with elongations ranging between 17-22% and obtaining an electrical conductivity of 45.17% IACS concerning the 30.52% IACS of the RSR material. Thus, the RSR process, together with the appropriate aging heat treatment, allows obtaining a structural heterogeneous copper alloy that stands out among different copper alloys by combining strength, conductivity, and ductility.

5. Hardness and yield strength values infer that the RSR method is a good and versatile alternative for producing bars with diameters in the range of 10-55 mm. The radial-shear rolling method at the large industrial production scale for bars will reduce the tool's cost, the occupied floor space, and equipment downtime associated with the readjustment and replacement of the tool.

Data availability statement: The raw/processed data required to reproduce these findings cannot be shared at this time as the data also forms part of an ongoing study.

Credit authorship contribution statement

Yu.V. Gamin: Investigation, formal analysis, writing original draft, writing review and editing. **Jairo Alberto Muñoz:** Investigation, formal analysis, writing review and editing. **A.S. Aleschenko:** Data curation, formal analysis and investigation. **A.A. Komissarov:** Supervision, funding acquisition, investigation. **N.S. Bunits:** Investigation, writing review and editing. **D.A. Nikolaev:** Investigation. **A.V. Fomin:** Data curation. **V.V. Cheverikin:** Investigation, data curation.

Conflict of interest: The authors declare no conflict of interest.

Acknowledges

The authors are grateful to the metallurgical company LLC «Astrinsplav SK» for the materials provided for this research. JAMB acknowledge the financial support of the Ministry of Science and Higher Education of the Russian Federation in the framework of Increase Competitiveness Program of NUST «MISiS» (№ К4-2019-045), implemented by a governmental decree dated 16th of March 2013, N 211.

References

[1] J.R. Davis, others, Copper and copper alloys, ASM international, 2001.
[2] A. V Zinov'ev, A.N. Koshmin, A.Y. Chasnikov, Effect of Continuous Extrusion Parameters on Alloy M1 Round Section Bar Microstructure and Mechanical Property Formation, Metallurgist. 63 (2019) 422–428. https://doi.org/10.1007/s11015-019-00838-3.
[3] Y. Sun, D. He, F. Xue, R. Lai, G. He, Microstructure and Mechanical Characterization of a Dissimilar Friction-Stir-Welded CuCrZr/CuNiCrSi Butt Joint, Metals (Basel). 8 (2018). https://doi.org/10.3390/met8050325.
[4] Q. Liu, X. Zhang, Y. Ge, J. Wang, J.-Z. Cui, Effect of processing and heat treatment on behavior of Cu-Cr-Zr alloys to railway contact wire, Metall. Mater. Trans. A. 37 (2006) 3233–3238. https://doi.org/10.1007/BF02586158.
[5] Y. V Gamin, B.A. Romantsev, A.N. Pashkov, P. V Patrin, I.A. Bystrov, A. V Fomin, M. V Kadach, Obtaining Hollow Semifinished Products Based on Copper Alloys for Electrical Purposes by Means of Screw Rolling, Russ. J. Non-Ferrous Met. 61 (2020) 162–171. https://doi.org/10.3103/S1067821220020054.
[6] Q. Lei, Z. Xiao, W. Hu, B. Derby, Z. Li, Phase transformation behaviors and properties of a high strength Cu-Ni-Si alloy, Mater. Sci. Eng. A. 697 (2017) 37–47. https://doi.org/https://doi.org/10.1016/j.msea.2017.05.001.
[7] H. Kim, J.H. Ahn, S.Z. Han, J. Jo, H. Baik, M. Kim, H.N. Han, Microstructural characterization of cold-drawn Cu–Ni–Si alloy having high strength and high conductivity, J. Alloys Compd. 832 (2020) 155059. https://doi.org/https://doi.org/10.1016/j.jallcom.2020.155059.
[8] V. Segal, Review: Modes and Processes of Severe Plastic Deformation (SPD)., Mater.

(Basel, Switzerland). 11 (2018). https://doi.org/10.3390/ma11071175.
[9] R.G. Chembarisova, E.A. Sarkeeva, I. V Alexandrov, W. Wei, Analysis of the effect of equal-channel angular pressing on the strength and electrical conductivity of low-alloyed alloys of the Cu-Cr-Zr system, J. Phys. Conf. Ser. 1431 (2020) 12065. https://doi.org/10.1088/1742-6596/1431/1/012065.
[10] E.N. Borodin, A. Morozova, V. Bratov, A. Belyakov, A.P. Jivkov, Experimental and numerical analyses of microstructure evolution of Cu-Cr-Zr alloys during severe plastic deformation, Mater. Charact. 156 (2019) 109849. https://doi.org/https://doi.org/10.1016/j.matchar.2019.109849.
[11] Y. Miyajima, M. Uchiyama, H. Adachi, T. Fujii, S. Onaka, M. Kato, Effect of Roll-Bonding and Subsequent Annealing on Microstructure Evolution of Accumulative Roll Bonded Pure Copper, Mater. Trans. 57 (2016) 1411–1417.
[12] W. Wang, H. Kang, Z. Chen, Z. Chen, C. Zou, R. Li, G. Yin, T. Wang, Effects of Cr and Zr additions on microstructure and properties of Cu-Ni-Si alloys, Mater. Sci. Eng. A. 673 (2016) 378–390. https://doi.org/https://doi.org/10.1016/j.msea.2016.07.021.
[13] A.B. Naizabekov, S.N. Lezhnev, E. Panin, Formation of a Gradient Structure in Austenitic Stainless Steel AISI 321 by Radial-Shear Rolling, in: Mater. Eng. Technol. Prod. Process. VI, Trans Tech Publications Ltd, 2021: pp. 246–251. https://doi.org/10.4028/www.scientific.net/SSP.316.246.
[14] X. Ding, L. Sun, X. Huang, Z. Zhao, Research on Three-Roll Screw Rolling Process for Ti6Al4V Titanium Alloy Bar, High Temp. Mater. Process. 38 (2019) 178–182.
[15] I.S. Valeev, A.K. Valeeva, R.F. Fazlyakhmetov, G.R. Khalikova, Effect of radial-shear rolling on structure of aluminum alloy D16 (Al-4.4Cu-1.6Mg), Inorg. Mater. Appl. Res. 6 (2015) 45–48. https://doi.org/10.1134/S2075113315010153.
[16] Y. Gamin, T. Akopyan, A. Koshmin, A. Dolbachev, A. Aleshchenko, S.P. Galkin, B.A. Romantsev, Investigation of the microstructure evolution and properties of A1050 aluminum alloy during radial-shear rolling using FEM analysis, Int. J. Adv. Manuf. Technol. 108 (2020) 695–704. https://doi.org/10.1007/s00170-020-05227-8.
[17] S. Shukla, D. Choudhuri, T. Wang, K. Liu, R. Wheeler, S. Williams, B. Gwalani, R.S. Mishra, Hierarchical features infused heterogeneous grain structure for extraordinary strength-ductility synergy, Mater. Res. Lett. 6 (2018) 676–682. https://doi.org/10.1080/21663831.2018.1538023.
[18] Y. Ma, M. Yang, F. Yuan, X. Wu, A Review on Heterogeneous Nanostructures: A Strategy for Superior Mechanical Properties in Metals, Metals (Basel). 9 (2019) 598. https://doi.org/10.3390/met9050598.
[19] J. Li, C. Fang, Y. Liu, Z. Huang, S. Wang, Q. Mao, Y. Li, Deformation mechanisms of 304L stainless steel with heterogeneous lamella structure, Mater. Sci. Eng. A. 742 (2019) 409–413. https://doi.org/10.1016/j.msea.2018.11.047.
[20] J. Duan, H. Wen, C. Zhou, X. He, R. Islamgaliev, R. Valiev, Discontinuous grain growth in an equal-channel angular pressing processed Fe-9Cr steel with a heterogeneous microstructure, Mater. Charact. (2019) 110004. https://doi.org/10.1016/J.MATCHAR.2019.110004.
[21] P. Sathiyamoorthi, H.S. Kim, Progress in Materials Science High-entropy alloys with heterogeneous microstructure : Processing and mechanical properties, Prog. Mater. Sci. (2020) 100709. https://doi.org/10.1016/j.pmatsci.2020.100709.
[22] P. Cai, X. Lian, Z. Tang, L. Zhang, T. Wang, L. Chai, G. Wu, Effect of heterogeneous laser surface treatment on mechanical properties of interstitial free steel, {IOP} Conf. Ser. Mater. Sci. Eng. 580 (2019) 12029. https://doi.org/10.1088/1757-899x/580/1/012029.
[23] J.A. Muñoz, O.F.H. Cobos, R. M'Doihoma, M. Avalos, R.E. Bolmaro, Inducing

heterogeneity in an austenitic stainless steel by equal channel angular sheet extrusion (ECASE), J. Mater. Res. Technol. 8 (2019) 2473–2479. https://doi.org/10.1016/j.jmrt.2019.04.013.
[24] J.A. Muñoz, M. Avalos, R.E. Bolmaro, Heterogeneity of strain path, texture and microstructure evolution of AA6063-T6 processed by Equal Channel Angular Sheet Extrusion (ECASE), J. Alloys Compd. 768 (2018) 349–357. https://doi.org/10.1016/j.jallcom.2018.07.216.
[25] J.A. Muñoz, A. Komissarov, M. Avalos, R.E. Bolmaro, Mechanical and microstructural behavior of a heterogeneous austenitic stainless steel processed by Equal Channel Angular Sheet Extrusion (ECASE), Mater. Sci. Eng. A. 792 (2020) 139779. https://doi.org/https://doi.org/10.1016/j.msea.2020.139779.
[26] M. Jamalian, M. Hamid, N. De Vincentis, Q. Buck, D.P. Field, H.M. Zbib, Creation of heterogeneous microstructures in copper using high-pressure torsion to enhance mechanical properties, Mater. Sci. Eng. A. 756 (2019) 142–148. https://doi.org/10.1016/j.msea.2019.04.024.
[27] A. Arbuz, A. Kawalek, K. Ozhmegov, H. Dyja, E. Panin, A. Lepsibayev, S. Sultanbekov, R. Shamenova, Using of Radial-Shear Rolling to Improve the Structure and Radiation Resistance of Zirconium-Based Alloys, Materials (Basel). 13 (2020). https://doi.org/10.3390/ma13194306.
[28] S.P. Galkin, Radial shear rolling as an optimal technology for lean production, Steel Transl. 44 (2014) 61–64. https://doi.org/10.3103/S0967091214010069.
[29] Gamin, Yury, Koshmin, Alexander, Ta, Dinh Xuan, Analysis of radial-shear rolling process parameters of aluminum alloys based on FEM modeling, MATEC Web Conf. 315 (2020) 11001. https://doi.org/10.1051/matecconf/202031511001.
[30] J. Blaber, B. Adair, A. Antoniou, Ncorr: Open-Source 2D Digital Image Correlation Matlab Software, Exp. Mech. 55 (2015) 1105–1122. https://doi.org/10.1007/s11340-015-0009-1.
[31] O.F. Higuera, J.A. Muñoz, J.M. Cabrera, Mechanical properties of different coppers processed by equal channel angular pressing, in: Mater. Sci. Forum, 2011: pp. 713–718.
[32] T.K. Akopyan, Y. V Gamin, S.P. Galkin, A.S. Prosviryakov, A.S. Aleshchenko, M.A. Noshin, A.N. Koshmin, A. V Fomin, Radial-shear rolling of high-strength aluminum alloys: Finite element simulation and analysis of microstructure and mechanical properties, Mater. Sci. Eng. A. 786 (2020) 139424. https://doi.org/https://doi.org/10.1016/j.msea.2020.139424.
[33] Y. V Gamin, T.K. Akopyan, A.N. Koshmin, A.P. Dolbachev, A. V Goncharuk, Microstructure evolution and property analysis of commercial pure Al alloy processed by radial-shear rolling, Arch. Civ. Mech. Eng. 20 (2020) 143. https://doi.org/10.1007/s43452-020-00143-w.
[34] Z. Rdzawski, J. Stobrawa, Thermomechanical processing of Cu–Ni–Si–Cr–Mg alloy, Mater. Sci. Technol. 9 (1993) 142–150. https://doi.org/10.1179/mst.1993.9.2.142.
[35] J.Y. Cheng, B.B. Tang, F.X. Yu, B. Shen, Evaluation of nanoscaled precipitates in a Cu–Ni–Si–Cr alloy during aging, J. Alloys Compd. 614 (2014) 189–195. https://doi.org/https://doi.org/10.1016/j.jallcom.2014.06.089.
[36] C. Igathinathane, L.O. Pordesimo, E.P. Columbus, W.D. Batchelor, S.R. Methuku, Shape identification and particles size distribution from basic shape parameters using ImageJ, Comput. Electron. Agric. 63 (2008) 168–182. https://doi.org/10.1016/j.compag.2008.02.007.
[37] Y. Wu, Y. Li, J. Lu, S. Tan, F. Jiang, J. Sun, Correlations between microstructures and properties of Cu-Ni-Si-Cr alloy, Mater. Sci. Eng. A. 731 (2018) 403–412.

https://doi.org/10.1016/j.msea.2018.06.075.
[38] O. V Samoilova, E.A. Trofimov, Phase equilibria in the copper-rich corner of the Cu-Ni-Si-Cr system, in: Mater. Sci. Forum, 2016: pp. 107–112.
[39] «Астринсплав СК» Металлургическое предприятие, Пруток бронзовый круглый, сплав, (n.d.). https://assk.ru/product/prutok-bronzovyj-kruglyj-splav-brnxkf-dkrnt-md-nd-5-35-mm/ (accessed June 3, 2021).
[40] O.E. Osintsev, V.N. Fedorov, Copper and Copper Alloys: Domestic and Foreign Brands, Mashinostr. Publ., Moscow. (2004).
[41] I.S. Yasnikov, A. Vinogradov, Y. Estrin, Revisiting the Considère criterion from the viewpoint of dislocation theory fundamentals, Scr. Mater. 76 (2014) 37–40. https://doi.org/10.1016/j.scriptamat.2013.12.009.
[42] Y. Chen, N. Gao, G. Sha, S.P. Ringer, M.J. Starink, Microstructural evolution, strengthening and thermal stability of an ultrafine-grained Al–Cu–Mg alloy, Acta Mater. 109 (2016) 202–212. https://doi.org/https://doi.org/10.1016/j.actamat.2016.02.050.
[43] M.A. Meyers, K.K. Chawla, Mechanical Behavior of Materials, Prentice Hall, 1999. https://books.google.ru/books?id=caJRAAAAMAAJ.
[44] H. Watanabe, T. Kunimine, C. Watanabe, R. Monzen, Y. Todaka, Tensile deformation characteristics of a Cu−Ni−Si alloy containing trace elements processed by high-pressure torsion with subsequent aging, Mater. Sci. Eng. A. 730 (2018) 10–15. https://doi.org/https://doi.org/10.1016/j.msea.2018.05.090.
[45] U.F. Kocks, H. Mecking, Physics and phenomenology of strain hardening: The FCC case, Prog. Mater. Sci. 48 (2003) 171–273. https://doi.org/10.1016/S0079-6425(02)00003-8.
[46] J.A. Muñoz, T. Khelfa, A. Komissarov, J.-M. Cabrera, Ductility and plasticity of ferritic-pearlitic steel after severe plastic deformation, Mater. Sci. Eng. A. 805 (2020) 140624. https://doi.org/https://doi.org/10.1016/j.msea.2020.140624.
[47] W.Q. Cao, C.F. Gu, E. V Pereloma, C.H.J. Davies, Stored energy, vacancies and thermal stability of ultra-fine grained copper, Mater. Sci. Eng. A. 492 (2008) 74–79. https://doi.org/https://doi.org/10.1016/j.msea.2008.02.048.
[48] S. Kobayashi, M. Hirata, S. Tsurekawa, T. Watanabe, Grain boundary engineering for control of fatigue crack propagation in austenitic stainless steel, Procedia Eng. 10 (2011) 112–117. https://doi.org/https://doi.org/10.1016/j.proeng.2011.04.021.
[49] J.A. Muñoz, A. Komissarov, I. Mejía, H. Hernández-Belmontes, J.-M. Cabrera, Characterization of the Gas Tungsten Arc Welding (GTAW) joint of Armco iron nanostructured by Equal-Channel Angular Pressing (ECAP), J. Mater. Process. Technol. 288 (2021) 116902. https://doi.org/https://doi.org/10.1016/j.jmatprotec.2020.116902.
[50] J.A. Muñoz, O.F. Higuera, A.H. Expósito, A. Boulaajaj, R.E. Bolmaro, F.D. Dumitru, P.R. Calvillo, A.M. Jorge, J.M. Cabrera, Thermal stability of ARMCO iron processed by ECAP, Int. J. Adv. Manuf. Technol. 98 (2018) 2917–2932. https://doi.org/10.1007/s00170-018-2353-7.
[51] H. Yang, K. Li, Y. Bu, J. Wu, Y. Fang, L. Meng, J. Liu, H. Wang, Nanoprecipitates induced dislocation pinning and multiplication strategy for designing high strength, plasticity and conductivity Cu alloys, Scr. Mater. 195 (2021) 113741. https://doi.org/https://doi.org/10.1016/j.scriptamat.2021.113741.
[52] B.G. Clark, I.M. Robertson, L.M. Dougherty, D.C. Ahn, P. Sofronis, High-temperature Dislocation-precipitate Interactions in Al Alloys: An in situ Transmission Electron Microscopy Deformation Study, J. Mater. Res. 20 (2005) 1792–1801. https://doi.org/10.1557/JMR.2005.0224.

[53] Q. Lei, S. Li, J. Zhu, Z. Xiao, F. Zhang, Z. Li, Microstructural evolution, phase transition, and physics properties of a high strength Cu–Ni–Si–Al alloy, Mater. Charact. 147 (2019) 315–323. https://doi.org/https://doi.org/10.1016/j.matchar.2018.11.018.
[54] Q. Lei, Z. Li, C. Dai, J. Wang, X. Chen, J.M. Xie, W.W. Yang, D.L. Chen, Effect of aluminum on microstructure and property of Cu–Ni–Si alloys, Mater. Sci. Eng. A. 572 (2013) 65–74. https://doi.org/https://doi.org/10.1016/j.msea.2013.02.024.
[55] J. Huang, Z. Xiao, J. Dai, Z. Li, H. Jiang, W. Wang, X. Zhang, Microstructure and Properties of a Novel Cu–Ni–Co–Si–Mg Alloy with Super-high Strength and Conductivity, Mater. Sci. Eng. A. 744 (2019) 754–763. https://doi.org/https://doi.org/10.1016/j.msea.2018.12.075.
[56] Y. Wu, Y. Li, J. Lu, S. Tan, F. Jiang, J. Sun, Effects of pre-deformation on precipitation behaviors and properties in Cu-Ni-Si-Cr alloy, Mater. Sci. Eng. A. 742 (2019) 501–507. https://doi.org/https://doi.org/10.1016/j.msea.2018.11.045.
[57] P. Stavroulakis, A. Toulfatzis, A. Vazdirvanidis, G. Pantazopoulos, S. Papaefthymiou, Investigation of the Aging Behavior of a Cu–Ni–Si Rolled Alloy, Metallogr. Microstruct. Anal. 8 (2019) 167–181. https://doi.org/10.1007/s13632-019-00531-6.
[58] S.Z. Han, J. Lee, S.H. Lim, J.H. Ahn, K. Kim, S. Kim, Optimization of conductivity and strength in Cu-Ni-Si alloys by suppressing discontinuous precipitation, Met. Mater. Int. 22 (2016) 1049–1054. https://doi.org/10.1007/s12540-016-6156-9.
[59] D.M. Zhao, Q.M. Dong, P. Liu, B.X. Kang, J.L. Huang, Z.H. Jin, Structure and strength of the age hardened Cu–Ni–Si alloy, Mater. Chem. Phys. 79 (2003) 81–86. https://doi.org/https://doi.org/10.1016/S0254-0584(02)00451-0.
[60] S.Z. Han, J.H. Gu, J.H. Lee, Z.P. Que, J.H. Shin, S.H. Lim, S.S. Kim, Effect of V addition on hardness and electrical conductivity in Cu-Ni-Si alloys, Met. Mater. Int. 19 (2013) 637–641. https://doi.org/10.1007/s12540-013-4002-x.
[61] H.G. Kim, T.W. Lee, S.M. Kim, S.Z. Han, K. Euh, W.Y. Kim, S.H. Lim, Effects of Ti addition and heat treatments on mechanical and electrical properties of Cu-Ni-Si alloys, Met. Mater. Int. 19 (2013) 61–65. https://doi.org/10.1007/s12540-013-1011-8.
[62] E. Lee, S. Han, K. Euh, S. Lim, S. Kim, Effect of Ti addition on tensile properties of Cu-Ni-Si alloys, Met. Mater. Int. 17 (2011) 569. https://doi.org/10.1007/s12540-011-0807-7.
[63] E. Lee, K. Euh, S.Z. Han, S. Lim, J. Lee, S. Kim, Tensile and electrical properties of direct aged Cu-Ni-Si-x%Ti alloys, Met. Mater. Int. 19 (2013) 183–188. https://doi.org/10.1007/s12540-013-2007-0.
[64] C. Watanabe, S. Takeshita, R. Monzen, Effects of Small Addition of Ti on Strength and Microstructure of a Cu-Ni-Si Alloy, Metall. Mater. Trans. A. 46 (2015) 2469–2475. https://doi.org/10.1007/s11661-015-2870-z.
[65] Z. Zhao, Z. Xiao, Z. Li, W. Qiu, H. Jiang, Q. Lei, Z. Liu, Y. Jiang, S. Zhang, Microstructure and properties of a Cu–Ni–Si–Co–Cr alloy with high strength and high conductivity, Mater. Sci. Eng. A. 759 (2019) 396–403. https://doi.org/https://doi.org/10.1016/j.msea.2019.05.003.
[66] Y. Zhang, B. Tian, A.A. Volinsky, H. Sun, Z. Chai, P. Liu, X. Chen, Y. Liu, Microstructure and Precipitate's Characterization of the Cu-Ni-Si-P Alloy, J. Mater. Eng. Perform. 25 (2016) 1336–1341. https://doi.org/10.1007/s11665-016-1987-6.

Figure captions

Fig. 1 Heat treatment diagram for Cu-Ni-Cr-Si alloy.
Fig. 2 Microstructure and hardness measurement scheme (a), and electroconductivity measurement scheme (b).
Fig. 3 Initial microstructure after casting process (a), grain size in the casting condition (b), tensile properties (c), EBSD map (d), and misorientation profiles for the lines indicated in the EBSD map (e).
Fig. 4 Surface grain diameter map after RSR (a), center grain diameter map after RSR (b), grain size evolution after RSR (c), surface grain diameter map after RSR+aging (d), center grain diameter map after RSR+aging (e), grain size evolution after RSR+aging (f).
Fig. 5 SEM map after aging treatment (a), EDS map (b), EDS spectrums for the red squares indicated in figure (a) (c), and Cu, Si, Ni, and Cr EDS maps (d)
Fig. 6 Precipitation particles sizes.
Fig. 7 Diffraction pattern for the Cu-Ni-Cr-Si alloy after RSR + Aging treatment
Fig. 8 Hardness evolution in the cross section after RSR and RSR + aging treatment.
Fig. 9 Mechanical properties at different zones of the samples after RSR and RSR + aging, (a) tensile curves, and (b) Considère criterion evolution.
Fig. 10 Strain evolution at the plastic instability points indicated in Fig. 8b, (a) RSR, and (b) RSR+aging.
Fig. 11 Strength contributions for the (a) RSR, (b) RSR+aged conditions, and (c) Kock's model fitting.
Fig. 12 Misorientation angle distributions and CSL maps for the different zones across the rod radius
Fig. 13 Microstructure heterogeneity, KAM maps and distributions across the rod radius (a), average grain size profiles after RSR and RSR+aged treatment (b), and yield strength and grain size changes after RSR and RSR+aged treatment (c).
Fig. 14 Electrical conductivity of Cu-Ni-Cr-Si alloy after RSR and heat treatment
Fig. 15 Comparison of the Cu-Ni-Cr-Si alloy properties with different Cu alloys: Cu-Ni-Si-Al [53,54], Cu-Ni-Co-Si-Mg [55], Cu-Ni-Si-Cr [35,37,56], Cu-Ni-Si [57–59], Cu-Ni-Si-V [60], Cu-Ni-Si-Ti [61–64], Cu-Ni-Si-Co-Cr [65], Cu-Ni-Si-P [66]. Ultimate tensile strength and conductivity (a), and elongation vs conductivity (b).

Table captions

Table 1. Chemical composition of Cu alloy (% wt.)
Table 2. Experimental properties of Cu-Ni-Cr-Si alloy in the initial state
Table 3. Deformation conditions of Rolling.
Table 4. Microstructural properties
Table 5. Comparative properties indicators of the rods made of Cu-Ni-Cr-Si alloy

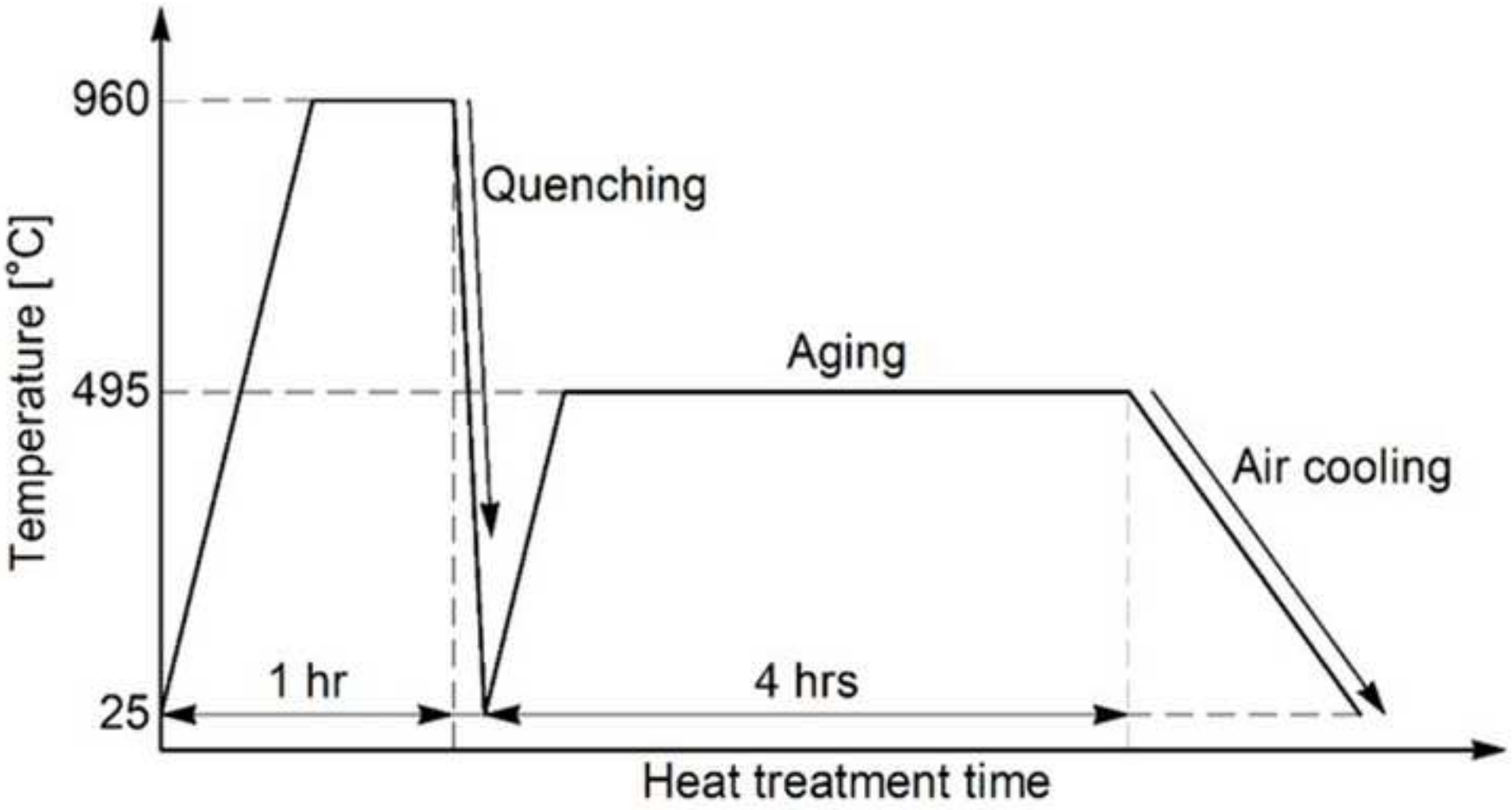

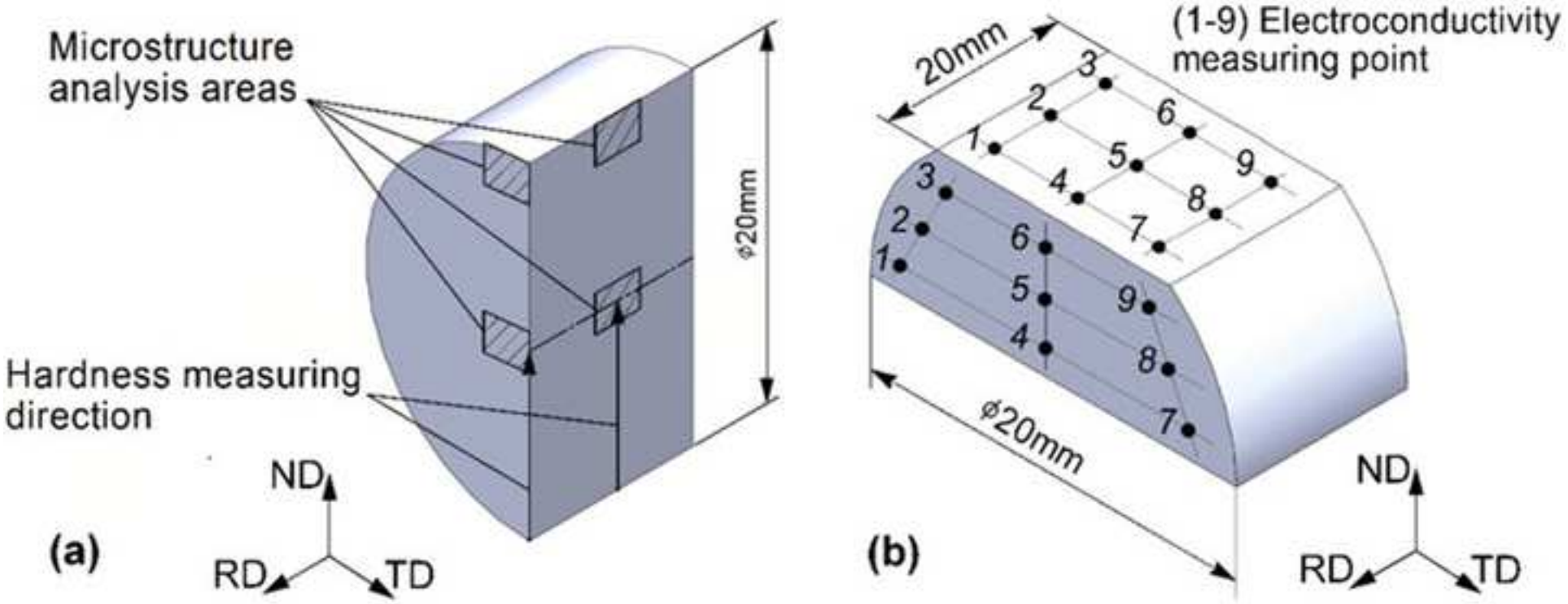

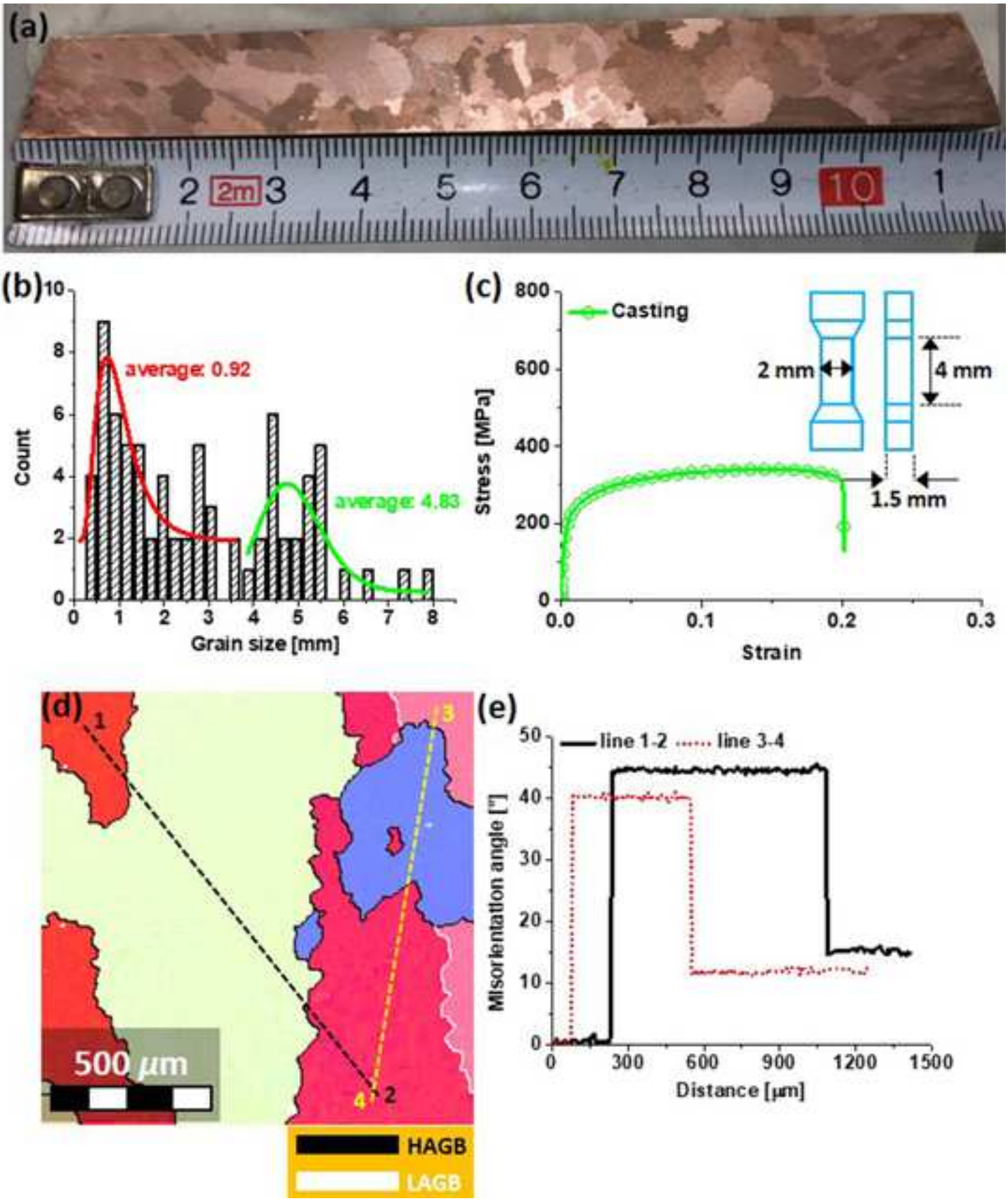
(a)
(b)
Count
Grain size [mm]
average: 0.92
average: 4.83
(c)
Casting
Stress [MPa]
Strain
2 mm
4 mm
1.5 mm
(d)
500 μm
HAGB
LAGB
(e)
line 1-2
line 3-4
Misorientation angle [°]
Distance [μm]

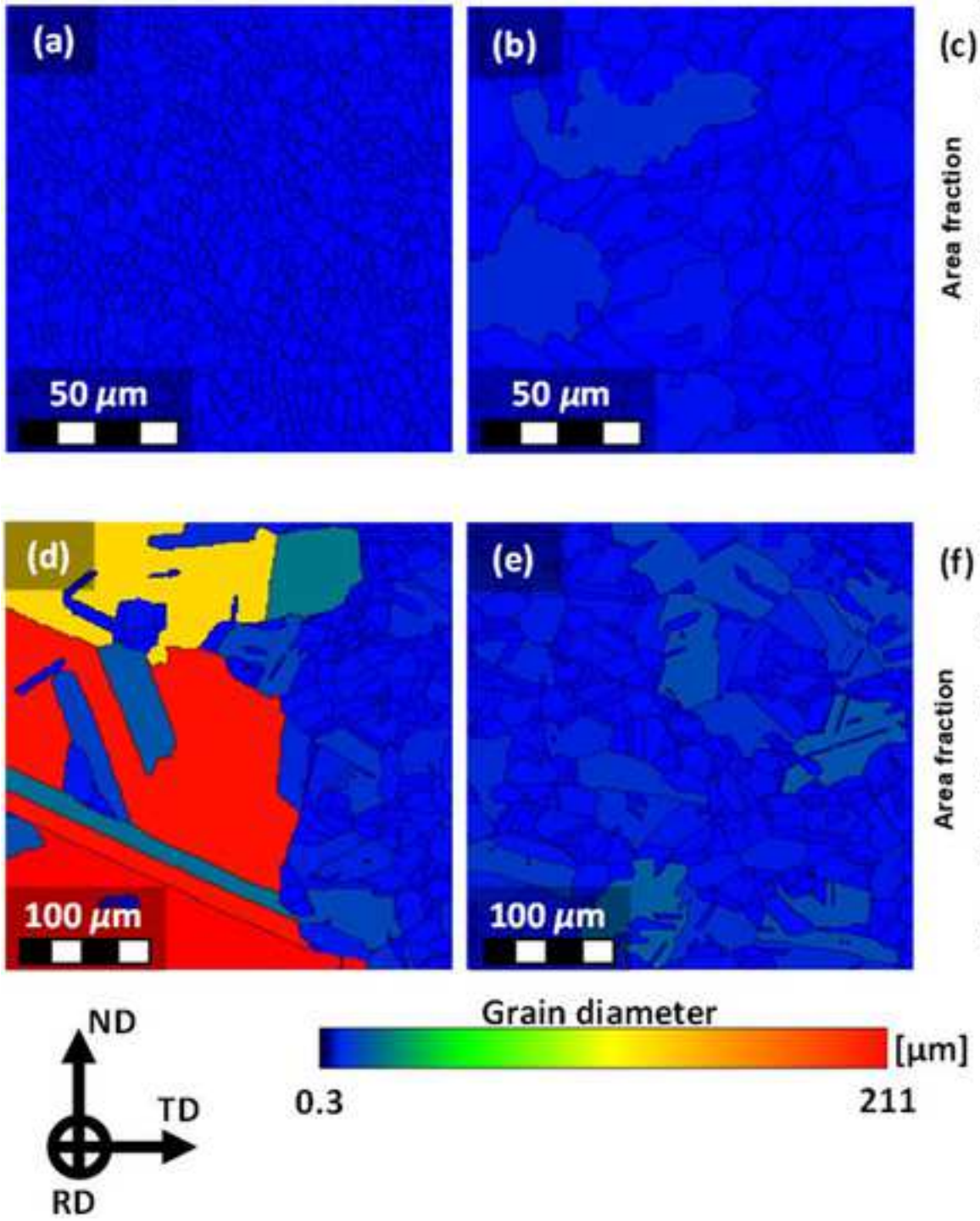

Figure(s)

Click here to access/download;Figure(s);image5.jpg

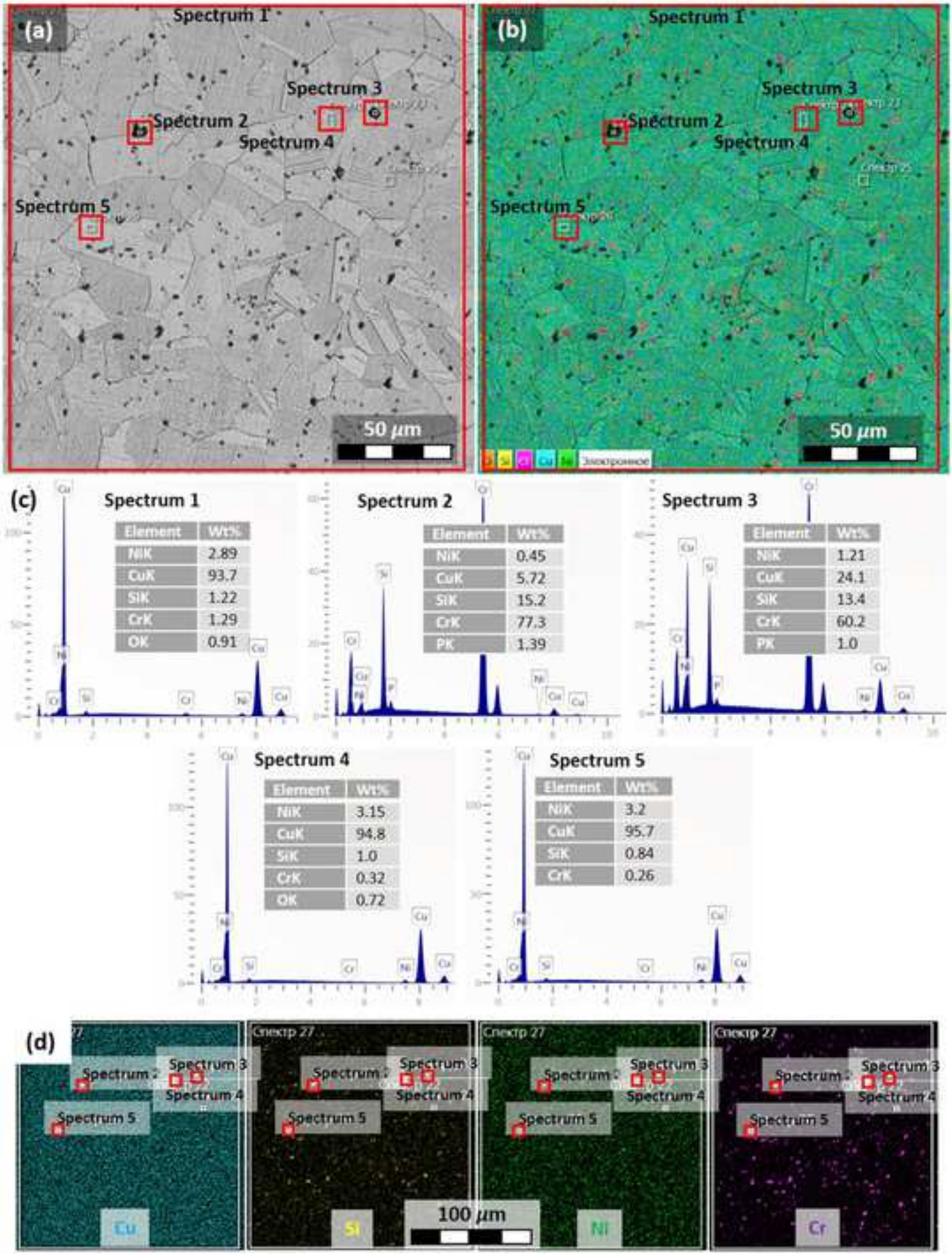

Figure(s)

Click here to access/download;Figure(s);image6.jpg

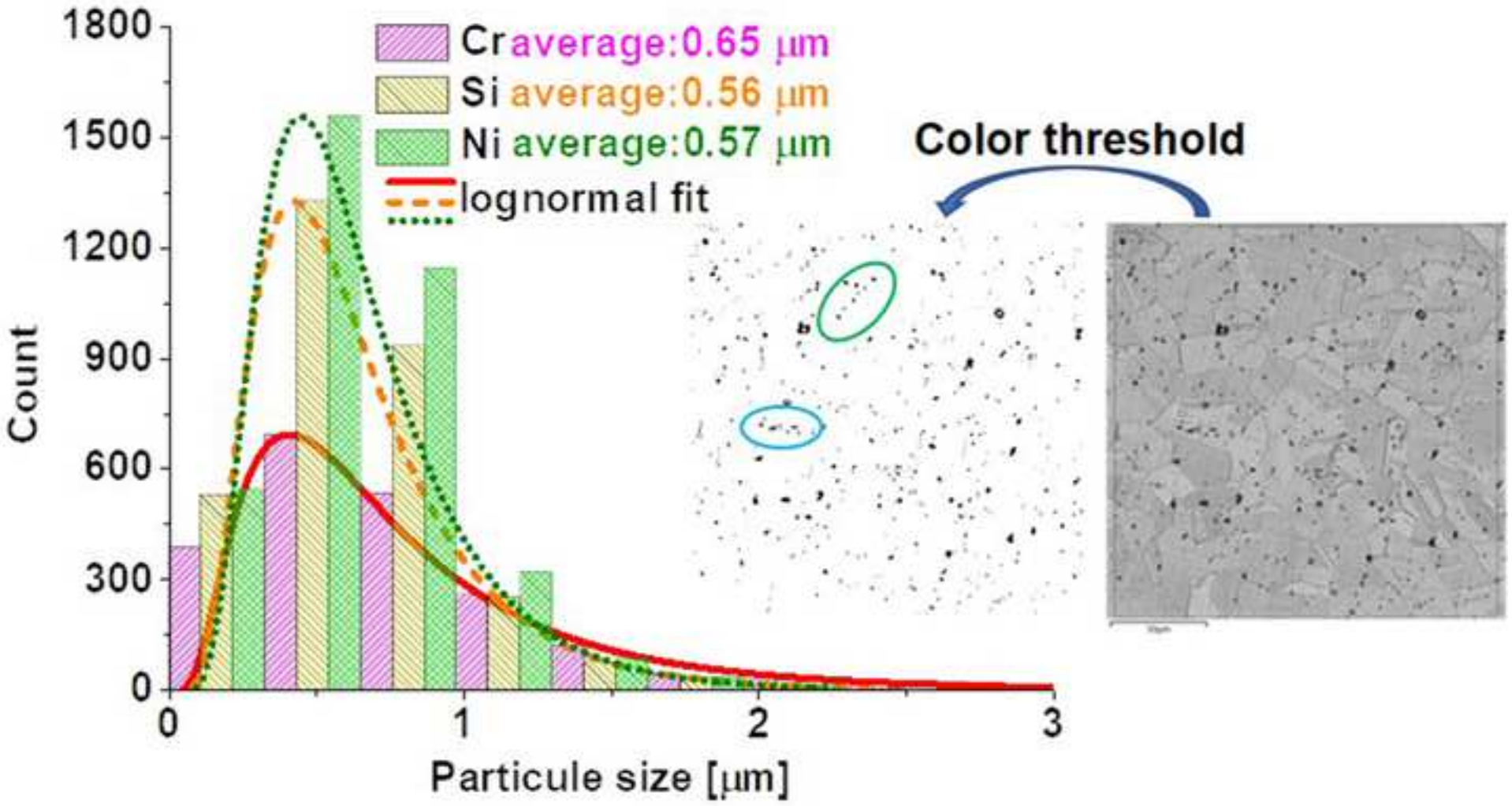

Figure(s)

Click here to access/download;Figure(s);image7.jpg

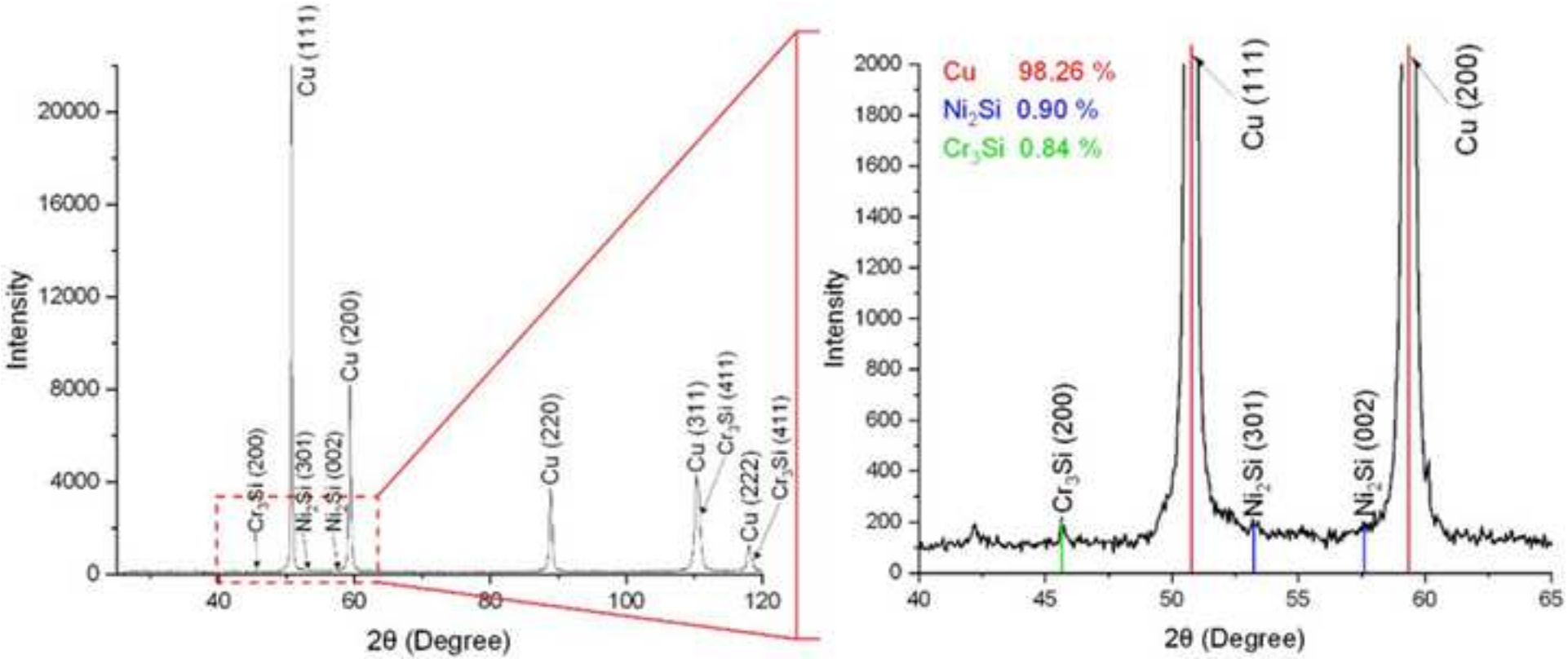

Figure(s)

Click here to access/download;Figure(s);image8.jpg

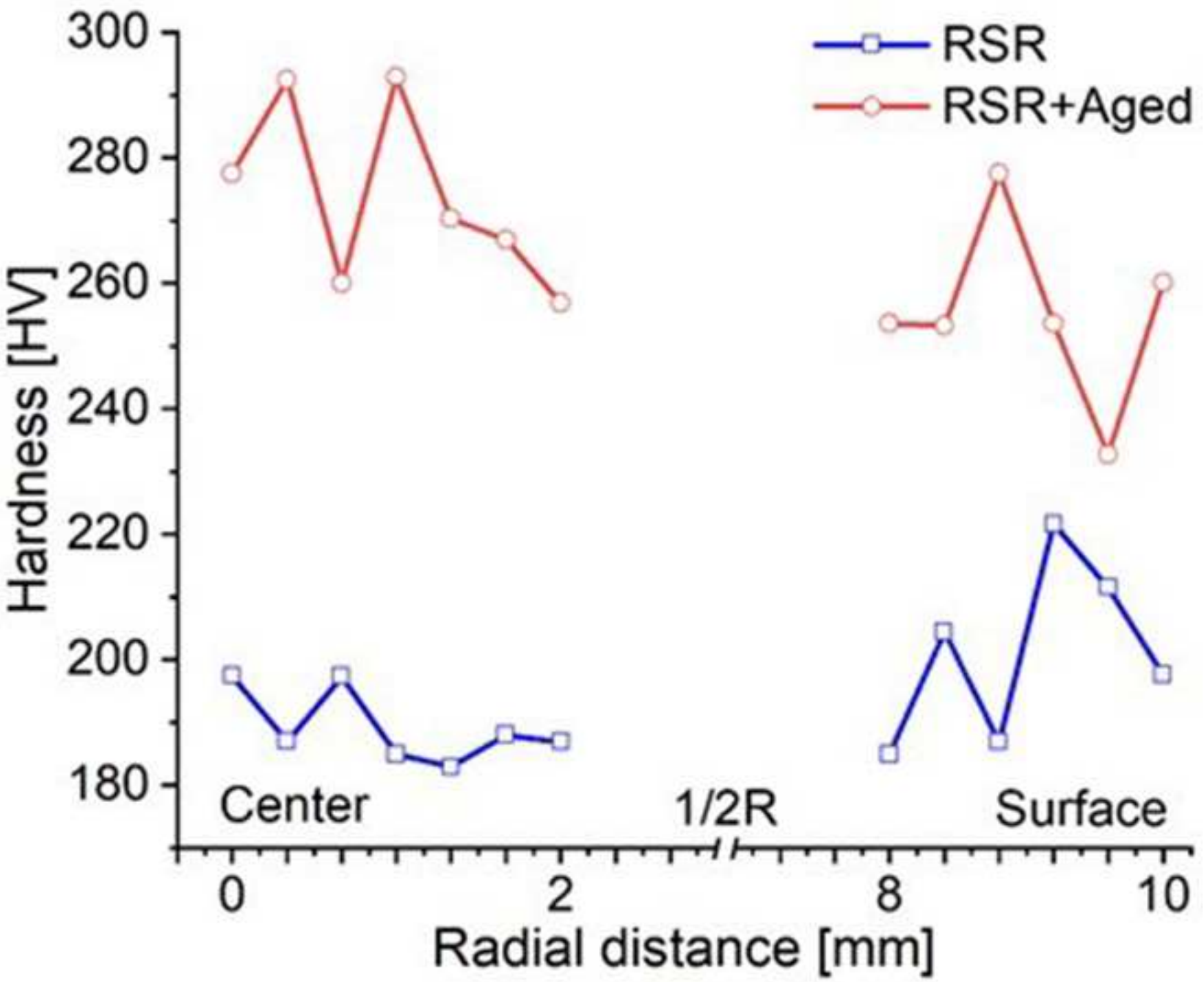

Figure(s)

Click here to access/download;Figure(s);image9.jpg

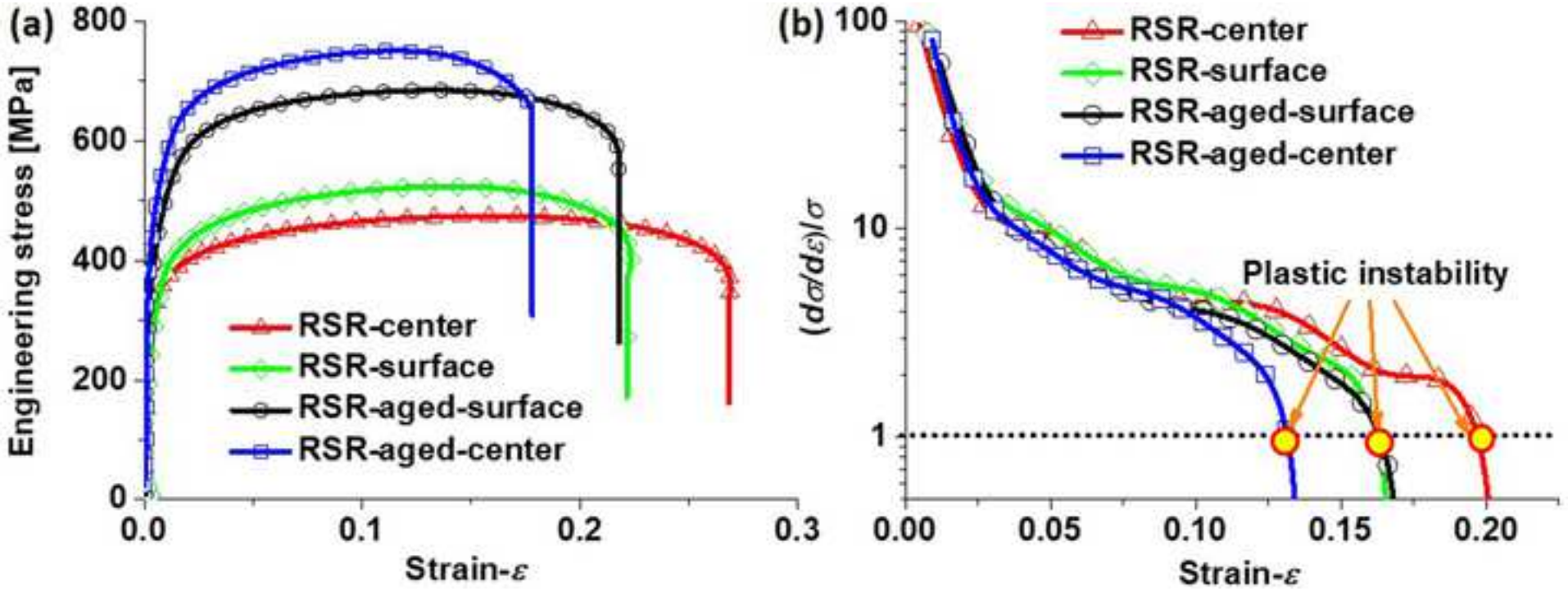

Figure(s)

Click here to access/download;Figure(s);image10.jpg

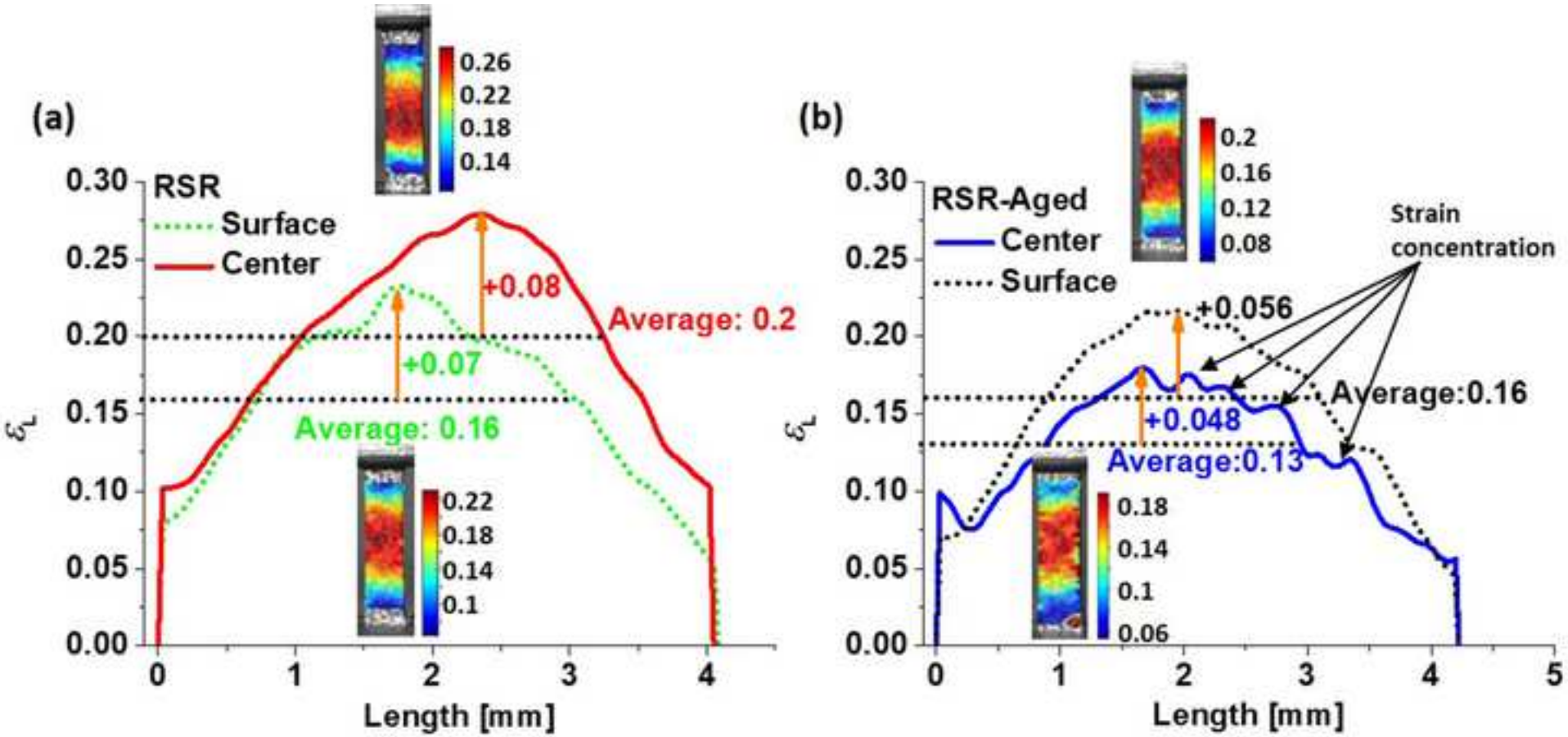

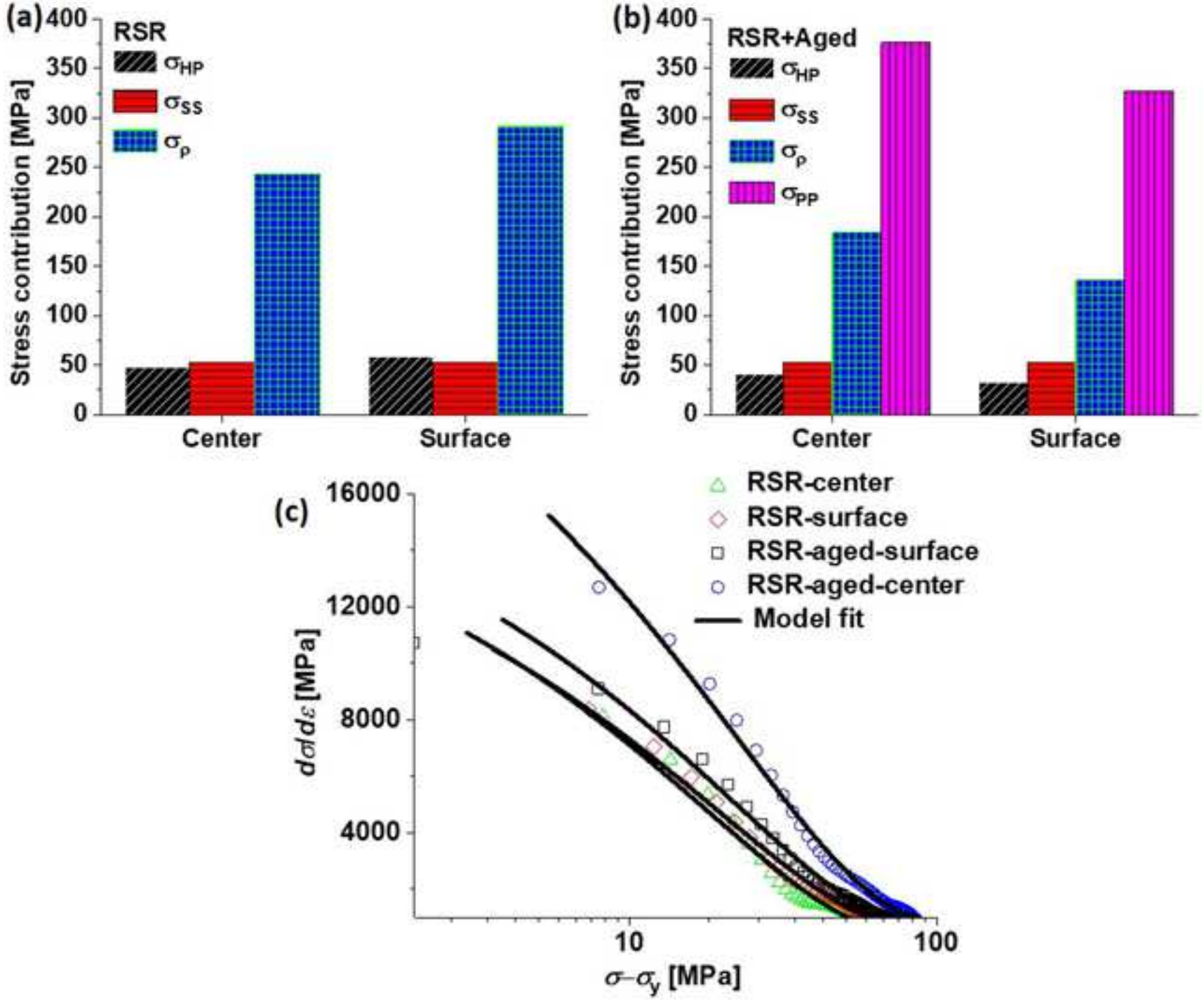

Figure(s)

Click here to access/download;Figure(s);image12.jpg

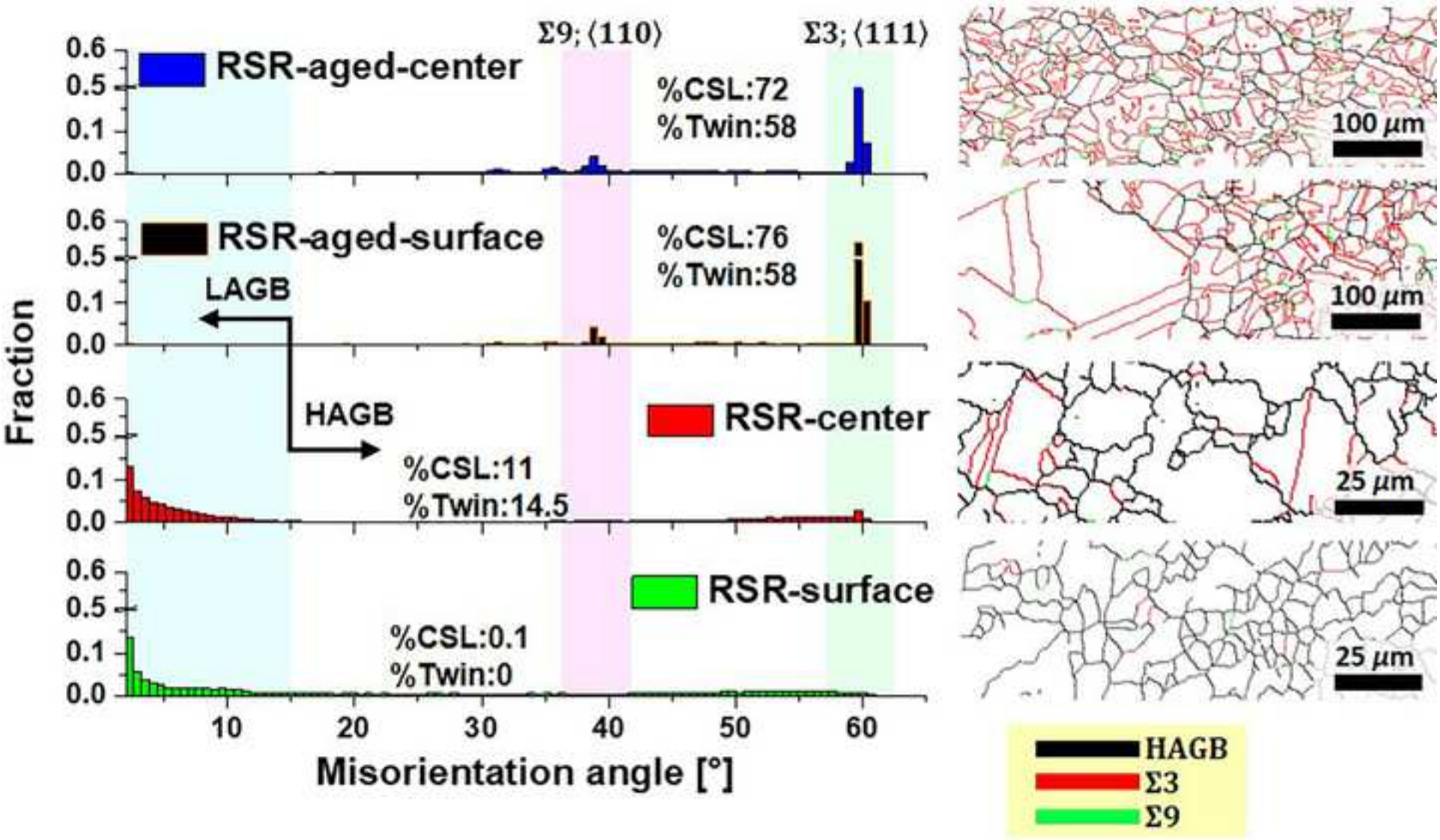

Figure(s)

Click here to access/download;Figure(s);image13.jpg

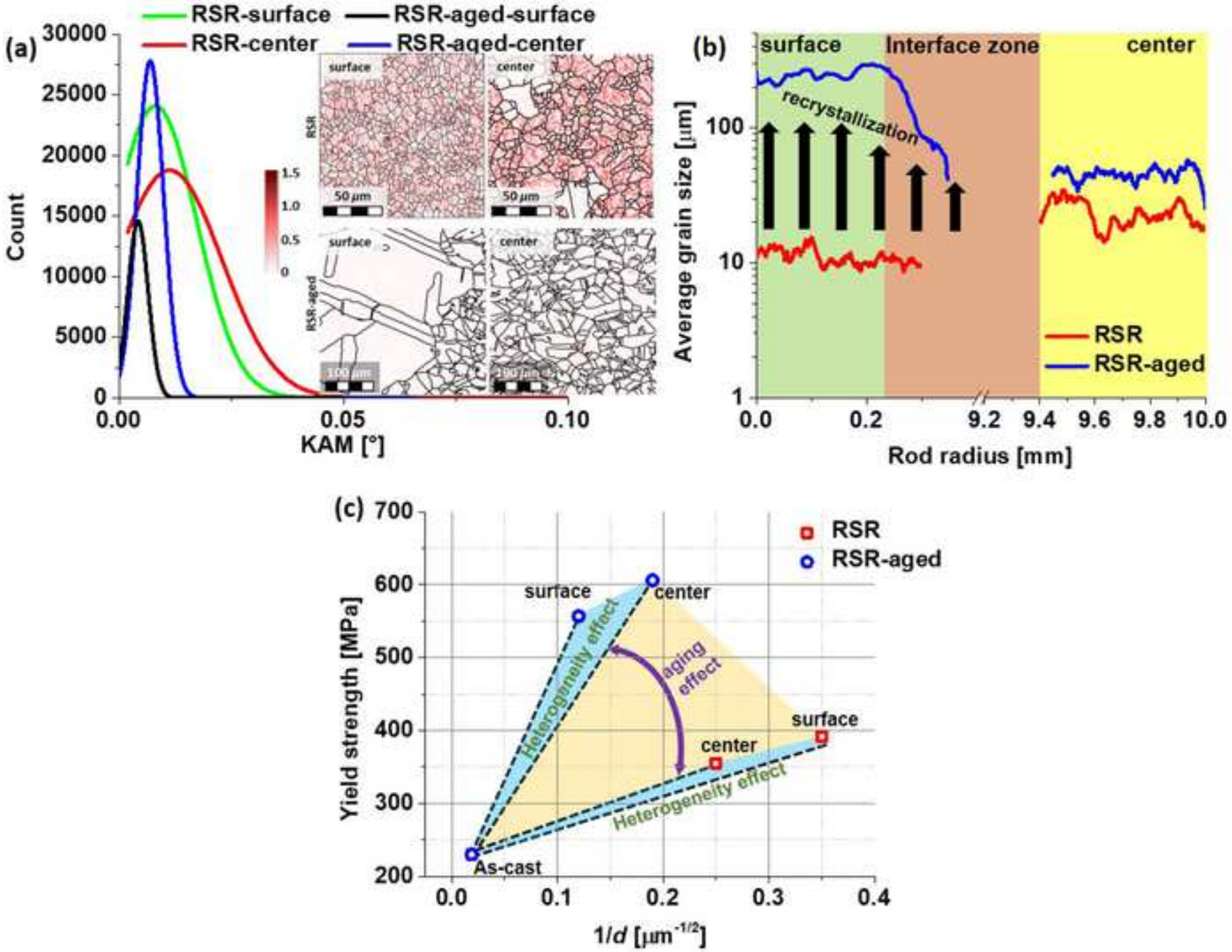

Figure(s)

Click here to access/download;Figure(s);image14.jpg

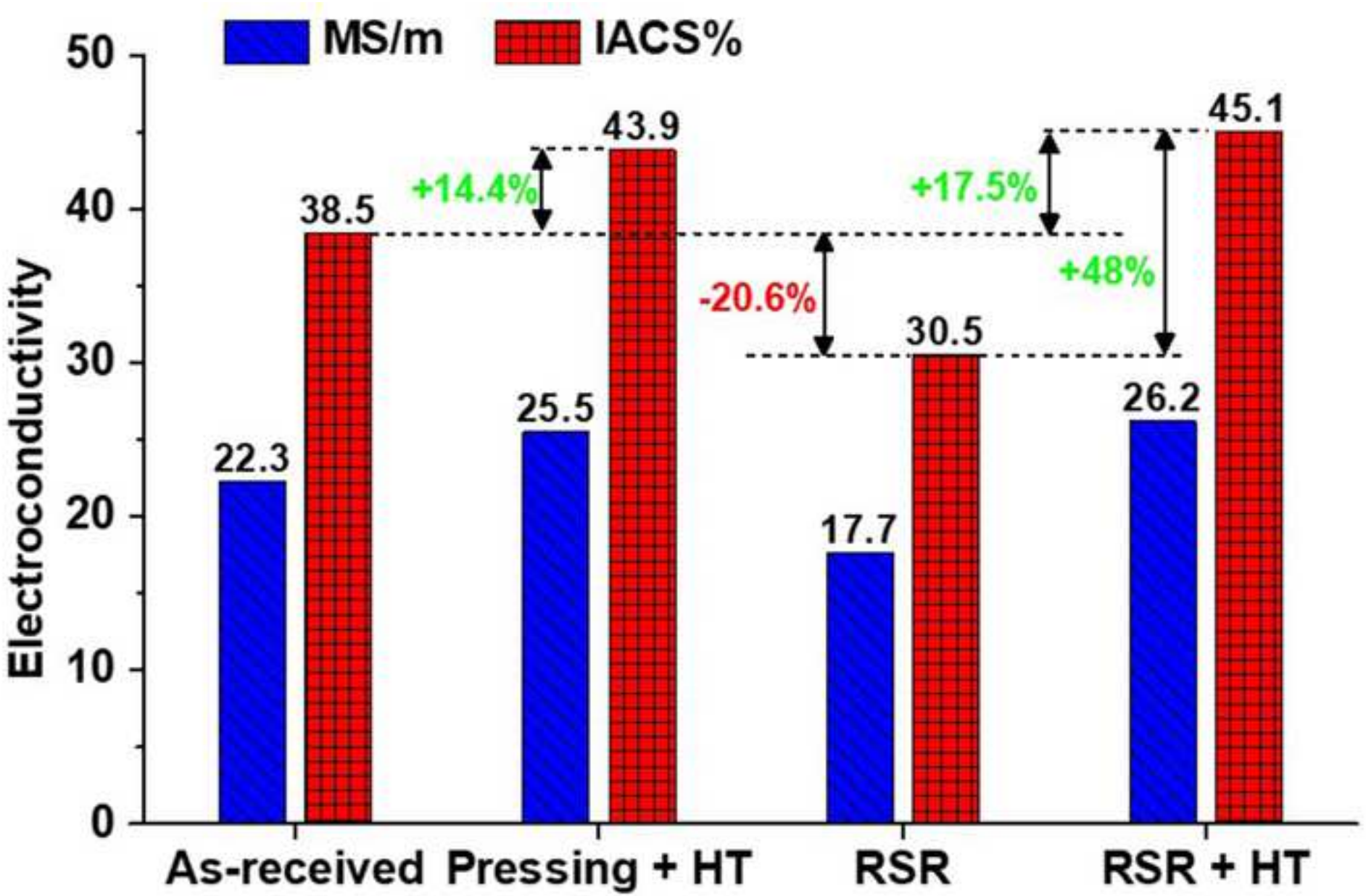

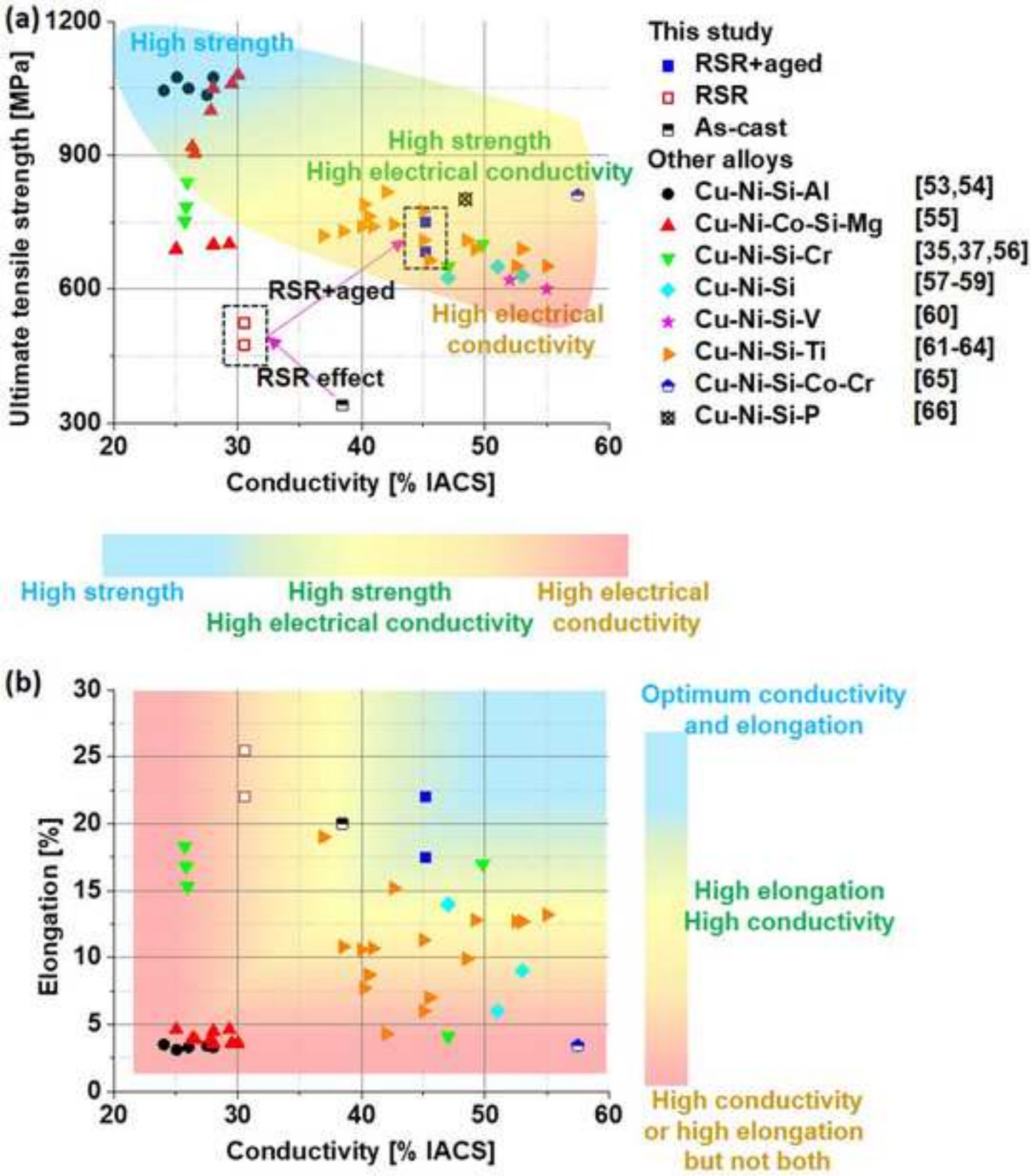

Table 1. Chemical composition of Cu alloy (% wt.)

Alloy	Cu	Ni	Cr	Si	Al	Zn	Fe	Other
Cu-Ni-Cr-Si	95.04	2.89	1.03	0.92	0.03	0.08	0.03	≤ 0.1

Table 1. Experimental properties of Cu-Ni-Cr-Si alloy in the initial state

Parameter name	Value
Hardness (HV)	130-150
Ultimate tensile strength (MPa)	340-380
Yield strength (MPa)	220-240
Elongation (%)	20
Electrical conductivity (MS/m)	22.3

Table 2. Deformation conditions of Rolling.

Pass Number, i	Diameter of workpiece D_{i-1}, mm	Diameter of the resulting rod D_i, mm	Elongation ratio μ_i	$\Sigma\mu_i$
1	60	46	1.70	1.70
2	46	36	1.63	2.78
3	36	28	1.65	4.60
4	28	20	1.96	9.00

Table 3. Microstructural properties

Condition	K_1	K_2	%HAGB	ρ [m^{-2}]	$d_{sub-grain}$ [μm]	$\bar{\gamma}$ [J/m^2]	E_b [J/g]
RSR-surface	1.1×10^{10}	126.8	47.2	8.1×10^{14}	3.20	0.52	0.036
RSR-center	9.8×10^{9}	112.9	40.7	5.7×10^{14}	7.14	0.50	0.016

RSR-aged-surface	3.8×10^{9}	54.8	98.1	1.7×10^{14}	13.05	0.62	0.011
RSR-aged-center	4.6×10^{9}	63.7	97.9	2.1×10^{14}	11.85	0.62	0.012

Table 4. Comparative properties indicators of the rods made of Cu-Ni-Cr-Si alloy

Parameter name	Method of hot deformation	
	Extrusion or drawing [39]	Radial-shear rolling
Hardness (HV)	210	260-280
Ultimate tensile strength (MPa)	750	650-750
Yield strength (MPa)	700	557-606
Elongation (%)	10	12-17
Electrical conductivity (MS/m)	24	26.2

Highlights

- Radial shear rolling can produce copper rods of different diameters at an industrial scale
- The thermomechanical process using radial shear rolling gives rise to a heterogeneous material
- Aging treatment after radial shear rolling produces a remarkable combination of strength, ductility, and electrical conductivity
- Dislocations annihilation and grain boundaries misorientation change help to improve the material electrical conductivity

Declaration of interests

☒ The authors declare that they have no known competing financial interests or personal relationships that could have appeared to influence the work reported in this paper.

☐The authors declare the following financial interests/personal relationships which may be considered as potential competing interests:

Credit authorship contribution statement

Yu.V. Gamin: Investigation, formal analysis, writing original draft, writing review and editing. **Jairo Alberto Muñoz:** Investigation, formal analysis, writing review and editing. **A.S. Aleschenko:** Data curation, formal analysis and investigation. **A.A. Komissarov:** Supervision, funding acquisition, investigation. **N.S. Bunits:** Investigation, writing review and editing. **D.A. Nikolaev:** Investigation. **A.V. Fomin:** Data curation. **V.V. Cheverikin:** Investigation, data curation.